

Data Acquisition of Atmospherically Induced Optical Signal Fluctuations

Master's Thesis of

Jiyun Kim

KIT Department of Electrical Engineering and Information Technology
Institute of Photonics and Quantum Electronics
Institute of Communications and Navigation, DLR

Reviewer: Prof. Dr.-Ing. Sebastian Randel
Second Reviewer: Prof. Dr.-Ing. Christian Koos
Advisors: M. Sc. Jonas Krimmer , IPQ
M. Sc. Carrillo Flores, Andrea Montserrat , DLR

September 18, 2023 - June 9, 2024

DECLARATION I, Jiyun Kim, hereby declare that I wrote my Master's thesis on my own and that I have followed the regulations relating to good scientific practice of the Karlsruhe Institute of Technology (KIT) in their latest form. I did not use any unacknowledged sources or means and I marked all references I used literally or by content.

I declare that I have developed and written the enclosed thesis completely by myself, and have not used sources or means without declaration in the text.

Karlsruhe, June 9, 2024

ACKNOWLEDGMENTS

I would like to express my sincere gratitude to several individuals who have provided invaluable support throughout my thesis journey.

First and foremost, I am deeply grateful to Andrea for granting me the opportunity to conduct research at DLR. Her guidance and support throughout the entire research process, from experiment design and execution to thesis writing, have been incredibly valuable. Her encouragement and motivational spirit were a constant source of strength, and her willingness to offer advice at every step was truly appreciated.

I would also like to extend my thanks to Professor Randel for providing me with the opportunity to pursue external research and for their dedicated supervision throughout this process.

Furthermore, I am truly grateful to Dr.Dirk for his valuable support with the experimental procedures and his insightful advice. His expertise was essential in ensuring the success of my experiments.

My sincere appreciation also goes to Jonas for his consistent weekly support and guidance, even with the challenges of long-distance communication. His willingness to offer guidance and share his knowledge has been greatly appreciated.

Finally, I am eternally grateful to my family for their unwavering emotional support throughout this endeavor. Their encouragement and belief in me have been a constant source of strength. In particular, I would like to express my deepest gratitude to my mother. Thank you, Mom, for your strength and for regaining your health. I eagerly await the opportunity to see you again soon.

ABSTRACT

Free-space optical (FSO) communication offers a cost-effective, high-bandwidth, and high-security [1] solution for diverse communication scenarios, attracting growing interest [2]. However, a significant challenge for FSO links is signal fluctuation, quantified by the power scintillation index (PSI) [3]. This fluctuation manifests as signal fading, which severely degrades link performance[4]. To mitigate this issue, transmitter diversity can be employed in FSO systems [5]. This study investigates the PSI and fading characteristics of FSO links utilizing double transmitters with three different divergence angle application over weak turbulence, log-normal atmospheric fading channels in a ground-to-ground horizontal link of 350 meters. We assume independent channels for our analysis, which leverages an approximation for the sum of uncorrelated log-normal random variables. To verify the lack of correlation between the two beams, additional measurements were conducted prior to the main data collection. The core investigation focuses on the performance improvements offered by the double transmitter configuration for each divergence angle. This evaluation will involve comparing PSI values and fade occurrence with a single transmitter setup. Additionally, the double transmitter performance across the different divergence angles were evaluated. Both numerical simulations and measurement data will be used to support this comprehensive evaluation. Additionally, a lightweight, standalone optical receiver system is also presented for further studies.

CONTENTS

1	INTRODUCTION	1
1.1	Free-Space Optical Communication	2
1.2	Optical Signal Optimization methods	2
1.3	Optical Communication scenarios	3
2	THEORY	7
2.1	Optical Beam	8
2.1.1	Near-infrared light	8
2.1.2	Gaussian Beam	8
2.1.3	Collimated Beam	10
2.2	Geometrical Approach	12
2.2.1	Free-Space Loss	12
2.2.2	Transmitter Gain and Receiver Gain	12
2.3	Atmospheric Turbulence	14
2.3.1	Attenuation	14
2.3.2	Atmospheric Turbulence	14
2.4	Beam Effects	18
2.5	Scintillation and Probability Density Function	23
2.5.1	Power Scintillation Index	23
2.5.2	Modified Rytov Approximation	23
2.5.3	Probability Density Function	25
2.6	Fades	28
2.7	Link Budget	31
2.8	Power Vector Generation Tool for Free-Space Optical Links	34
2.9	Spatial Diversity	37
2.9.1	Sum of Random Variable	39
2.9.2	Mean Power and PSI with N transmitters	40
2.10	Transmitter Diversity	43
2.10.1	Transmitters Separation	43
2.10.2	Double Transmitter	43
2.10.3	Simulations	44
3	HARDWARE	49
3.1	Transmitter	50
3.2	Receiver	52
4	MEASUREMENT	55
4.1	Measurement Data Structure	56
4.2	Transmitter Separation Distance	58

CONTENTS

4.3	Overall Measurement Structure	62
5	ANALYSIS	65
5.1	Probability Density Function	66
5.2	10 cycles overall analysis	69
5.3	Mean Received Power Comparison	77
5.4	Power Scintillation Index Comparison	79
5.5	Fades Comparison	82
6	CONCLUSION	85
	LIST OF ACRONYMS	89
	BIBLIOGRAPHY	91

INTRODUCTION

1 INTRODUCTION

1.1 FREE-SPACE OPTICAL COMMUNICATION

Free space optical communication (FSOC) provides numerous benefits in comparison to Radio Frequency (RF) communications in satellite applications. FSOC overcome bandwidth limitations and channel limitations, which presents in RF spectrum by the International Telecommunications Unit (ITU) [2]. Additionally, it ensures high security by avoiding crosstalk and interference [1]. Furthermore, FSOC terminals and optical ground stations (OGS) require less physical space, offer improved cost-effectiveness, and exhibit greater power efficiency in comparison to RF communication. Consequently, this allows for the use of independent receiver systems on unmanned aerial vehicles (UAVs), which leads to faster implementation times and enhanced network capabilities using high-speed optical data connections [6].

However, the open atmosphere throws a wrench in the works. Variations in air known as atmospheric turbulence result in scintillation – the rapid twinkling of the laser beam and notable signal degradation - signal fading. Moreover, disruptions such as clouds, snow, and rain can further impede signal strength, potentially leading to data errors. Additionally, the extensive capabilities and potential applications of this technology on over long distances are hindered by the demanding need for precise pointing and tracking accuracy due to the small divergences in the optical beam. Overcoming this obstacle is essential to fully harness the benefits of optical connections [7], [8].

1.2 OPTICAL SIGNAL OPTIMIZATION METHODS

To combat atmospheric turbulence that disrupts signals and hinders data transmission, ensuring reliable communication, methods to optimize optical signals were introduced. Promising strategies are multiple beam utilization [9], [10].

By leveraging a multitude of laser beams, each carrying a share of the data, FSO systems can enhance the overall reliability of transmission. In the event of atmospheric turbulence affecting one beam, the remaining beams stand a chance of successfully transmitting, safeguarding the integrity of the data. Spatial diversity techniques entail sending beams at slightly varied angles, establishing diverse paths for the signal to follow. This strategy helps alleviate the impact of localized atmospheric disturbances. Moreover, wavelength division multiplexing (WDM) involves utilizing distinct light wavelengths for each data stream, enabling them to navigate through the atmosphere with differing levels of vulnerability to interference [5].

By employing spatial diversity, the system makes use of multiple laser sources to send out identical data concurrently. This redundancy serves as a protective mechanism; if one transmitter faces power fluctuations or alignment challenges, others can compensate for it. The advantages of transmitter diversity extend beyond mere redundancy. Since each beam experiences scintillation independently, the combined received power from multiple beams tends to average out the fluctuations. This reduces the overall impact of scintillation on the signal strength. Additionally, with multiple beams contributing to the received power, the overall signal becomes

1.3 OPTICAL COMMUNICATION SCENARIOS

stronger, resulting in an enhanced signal-to-noise ratio (SNR) that aids in distinguishing data from background noise more effectively [11].

Mitigating the scintillation effect and increasing the received power play a crucial role in enhancing the reliability of data transmission, particularly in adverse atmospheric environments. Advancements in research are likely to introduce more advanced strategies such as spatial diversity in combination with adaptive optics, aiming to extend the coverage and reliability of FSO communication systems. The utilization of this technology shows great promise in transforming data transfer across a range of applications[12], spanning from high-capacity backhaul networks to safeguarded communication channels for critical infrastructure [13].

This study implemented a transmitter diversity method by employing a 1.6mW 1550nm Gaussian beam for each transmitter, each with varying full width half maximum (FWHM) divergence angles of $330\mu\text{rad}$, $545\mu\text{rad}$, and $924\mu\text{rad}$. The purpose was to explore the benefits of transmitter diversity in various narrow configurations of optical beams.

1.3 OPTICAL COMMUNICATION SCENARIOS

FSO communication systems utilize open space as the medium for transmitting optical signals between line-of-sight apertures. The effectiveness of signal transmission and reception in FSO systems is influenced by the properties of the medium, whether it be the atmosphere, outer space, or a vacuum. FSO technology facilitates data transmission through the propagation of light in atmospheric or space channels, enabling optical connectivity [9].

FSO technology provides significant flexibility in creating high-speed optical network structures, reaching speeds of tens to hundreds of gigabits per second. It supports various communication configurations such as point-to-point, point-to-multipoint, multipoint-to-point, and multipoint-to-multipoint, accommodating different optical link establishment scenarios. Atmospheric effects impact the uplink, downlink and ground-to-ground transmissions in free-space optical laser communications across atmosphere with variations in their effects [2], [9].

Although it is crucial to examine both the uplink and downlink aspects, delving into horizontal FSO connections presents unique benefits when exploring atmospheric influences. Examination of how atmospheric factors influence the propagation of laser beams through horizontal FSO links over shorter distances in controlled settings provides researchers with the opportunity to perform precise experiments within limited spatial confines. This configuration enables the conduct of controlled experiments where atmospheric conditions and environmental parameters can be observed. Moreover, delving into horizontal FSO links assists researchers in enhancing their comprehension of the impact of atmospheric conditions on laser beam transmission. This insight facilitates the enhancement of FSO systems on both the sending and receiving sides by devising strategies to minimize scintillation, address signal deterioration, and ensure consistent high-speed data delivery in turbulent atmospheres[14], [9].

Our configuration involves a short-range optical link established in the vicinity of the Earth's

1 INTRODUCTION

surface, specifically designed to study signal variations and the impact of fades resulting from optical turbulence. This investigation is conducted without involving data transmission or modulations.

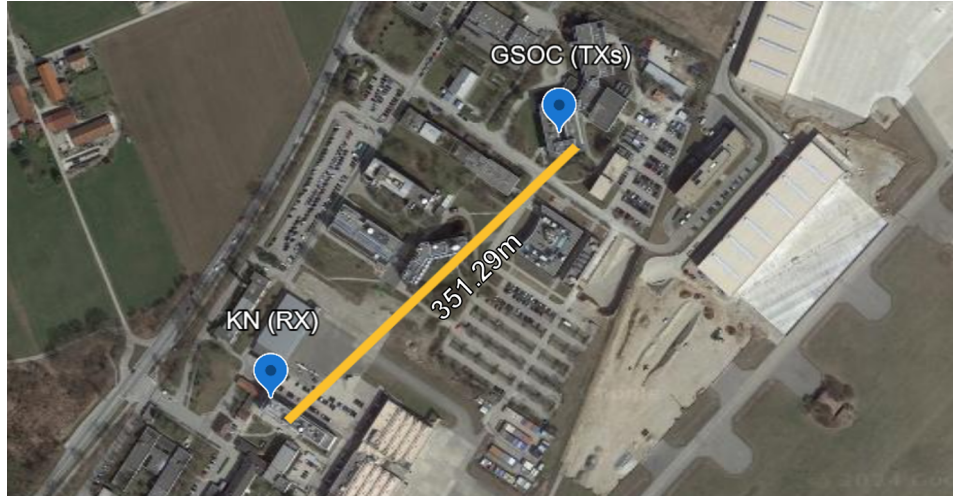


FIGURE 1: Link Configuration in DLR Campus

Our experiments were conducted across an expansive area spanning approximately 350 meters on the DLR campus in Wessling. The configuration is visually illustrated in the provided image1. The transmitters and receiver were strategically positioned at the GSOC(German Space Operations Centre) building and KN(Institute for Communication and Navigation) building respectively, both situated at an elevation of around 580 meters above sea level, indicating a short-range horizontal link. Data collection using these arrangements took place over an extended period, starting from March 14th to April 16th. Each measurement was taken at different time intervals and under various weather conditions. Environmental factors were meticulously recorded alongside the measurement data in Chapter 4 Measurement. The detailed configuration of the optical link is presented in the Table 1 below.

1.3 OPTICAL COMMUNICATION SCENARIOS

Location	Description	Scenario properties
GSOC	Altitude	580m s.l.
	Location	48.09, 11.28
	Number of transmitter	1 or 2
	Theoretical output beam diameter ($1/e^2$)	3.6mm, 2.1mm, 1.21mm
	Wavelength	1550nm
	Divergence angle (FWHM)	330urad, 545urad, 924urad
	Transmitter power	1.6mW
KN	Altitude	580m s.l.
	Location	48.08, 11.28
	Number of receiver	1
	Receiver aperture diameter	25.4mm
	Noise Equivalent Power	0.213nW

TABLE 1: Link Configuration Properties

The rest of the thesis is organized as follows Chapter 2, Theory, introduces the concept of a collimated Gaussian beam and its behavior in log-normal distributed atmospheric turbulence. It then explores spatial diversity and transmitter diversity with mathematical and numerical analysis. Chapter 3, Hardware, details the specifications of the transmitter and receiver assemblies and its properties. Chapter 4, Measurements, outlines the experiment's strategies, measurement data structures, and results obtained using transmitter diversity with varying transmitter separations distances. Chapter 5, Analysis, compares the experimental performance of the double-transmitter configuration with mathematical and numerical simulations, focusing on metrics like mean received power, probability density function, power scintillation index, and fade events. Finally, Chapter 6, Conclusion, presents the key findings and overall conclusions drawn from the research.

2 THEORY

2.1 OPTICAL BEAM

2.1.1 NEAR-INFRARED LIGHT

The invention of the LASER (Light Amplification by Stimulated Emission of Radiation) in 1960 opened a new era of possibilities for communication technologies. Researchers quickly recognized the potential of lasers to extend radio-frequency techniques into the optical-frequency domain, offering significantly higher bandwidth capabilities [15]. In near-earth laser communication systems relying on direct detection, several factors significantly impact system performance. These factors include atmospheric attenuation, eye safety regulations, and readily available laser technology. When considering all these aspects, a wavelength of 1550nm emerges as the optimal choice. This selection prioritizes efficient signal transmission by minimizing atmospheric signal loss [16], [17]. Additionally, it adheres to eye safety regulations due to the reduced hazard at this wavelength compared to other wavelength with same power. Finally, 1550nm benefits from the widespread availability of suitable laser sources. Due to these combined advantages, we opted for a 1550nm near-infrared laser as the transmitter source in our system [14].

2.1.2 GAUSSIAN BEAM

Laser communication systems predominantly utilize the Gaussian (TEM_{00}) mode due to its synergistic advantages. The symmetrical Gaussian profile aligns perfectly with typical laser cavity geometries, maximizing light amplification and minimizing unwanted reflections. Additionally, its inherent stability ensures minimal distortion during propagation, even in scenarios with imperfect components or atmospheric turbulence. Finally, the well-understood mathematical nature of the Gaussian distribution facilitates accurate theoretical modeling of beam interactions with optical elements, simplifying system design and analysis. These combined benefits solidify the Gaussian mode as the optimal choice for robust and efficient laser communication [18],[19]. Our experimental setup utilizes a Gaussian source beam. The far-field intensity distribution, $I(L, \theta)$, of such a beam is characterized by the following equation:

$$I(L, \theta) = I_0(L) e^{-2(\frac{\theta}{\omega_0})^2} \quad [W/m^2] \quad (1)$$

where,

L is a link distance

$I_0(L)$ is the intensity at the center of the beam

ω_0 is an angular distance from the center where the intensity is $1/e^2$

θ is the angular deviation from the center of the beam

Figure 2 (referenced by [20]) depicts the normalized intensity distribution of Gaussian beams with varying divergence angles, which aligns with the configurations employed in our measurements. The divergence angles were controlled by incorporating different collimators with varying divergence specifications into the transmitter assembly. Details regarding these transmitter assembly will be explained in Chapter 3.

2.1 OPTICAL BEAM

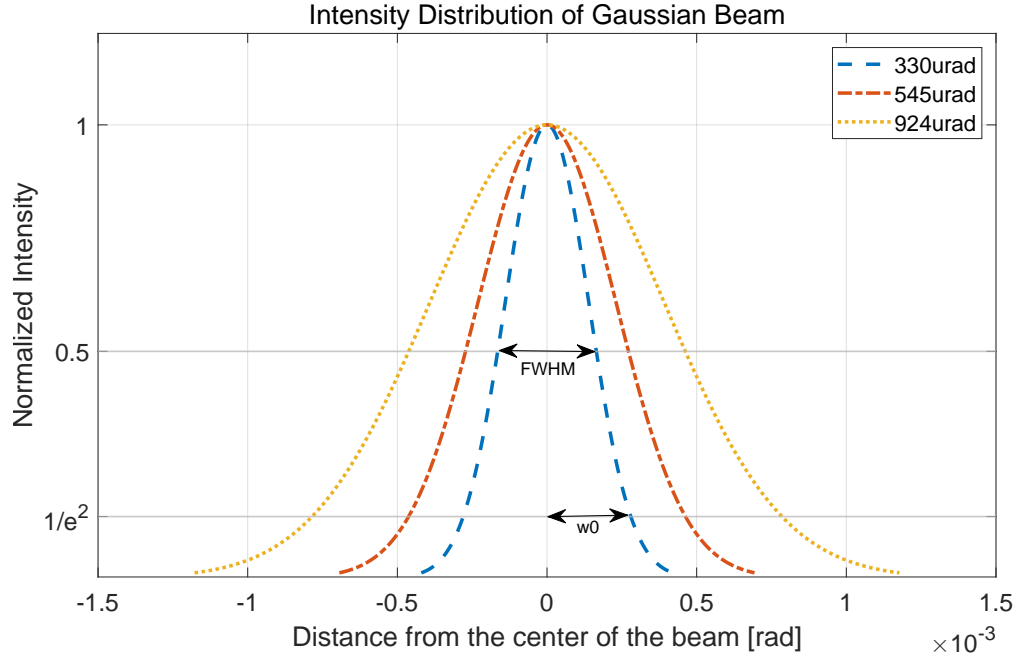


FIGURE 2: Intensity Distribution of Gaussian Beam [20]

The beam waist radius, denoted as ω_0 , represents the point along the propagation axis where the intensity has dropped to $1/e^2$ of its on-axis value. A smaller ω_0 signifies a narrower initial beam, enabling tighter focusing with lenses. Conversely, beams with a larger ω_0 exhibit slower divergence compared to their narrower counterparts [21].

The Full Width at Half Maximum (FWHM), denoted by θ_{FWHM} , is a prevalent metric used across various disciplines to quantify the width of a distribution. In the context of Gaussian beams, the FWHM value (θ_{FWHM}) represents twice the angular distance from the beam's center to the point where the intensity falls to half its peak value (I_0). A smaller FWHM indicates a more concentrated beam with a higher central power density. The divergence angle of the transmitted Gaussian beam is frequently expressed using the FWHM value. This approach is also adopted divergence angle as FWHM value. The relationship between θ_{FWHM} and ω_0 for Gaussian beams is given by [20]:

$$\omega_0 = \frac{\theta_{FWHM}}{\sqrt{2\ln 2}} \quad [\text{rad}] \quad (2)$$

Table 2 summarizes the characteristics of the beams employed in our measurements. The Full Width at Half Maximum (FWHM) divergence angle of these collimators was determined using the Equation 2.

2 THEORY

Full range angle ω_0	$559\mu\text{rad}$	$925\mu\text{rad}$	$1570\mu\text{rad}$
FWHM divergence angle θ_{FWHM}	$330\mu\text{rad}$	$545\mu\text{rad}$	$924\mu\text{rad}$

TABLE 2: Beam Characteristics

2.1.3 COLLIMATED BEAM

Let us consider a gaussian beam with initial amplitude A_0 propagating through free space. The transmitter is located at a reference plane denoted by $z = 0$. At this plane, the beam's amplitude distribution exhibits a Gaussian profile characterized by initial beam radius, W_0 [m]. This parameter defines the radius at which the beam intensity weakens to $1/e^2$ of its peak value on the beam axis. The Gaussian beam at $z = 0$ is given by [13]:

$$U_0(r, 0) = A_0 \exp\left(-\frac{r^2}{W_0^2} - i\frac{kr^2}{2F_0}\right) \quad (3)$$

Within this equation, r represents the distance measured from the center of the beam in a perpendicular direction (transverse direction). $k (= 2\pi/\lambda)$ [1/m] is the optical wave number. Finally, F_0 signifies the radius of curvature of the beam's wavefront, which specifies the beam forming. Figure 3 illustrated positive values of F_0 ($F_0 > 0$) correspond to converging beams, $F_0 = 1$ represents a collimated beam, and negative values ($F_0 < 0$) indicate diverging beams [13].

Collimated beams hold significant advantages in optical applications due to their characteristic property of minimal divergence, resulting in near-parallel propagation of light rays. However, they are not the only viable option. Diverging beams, in contrast, exhibit spreading light rays with increasing divergence angles. This characteristic allows them to illuminate large areas, albeit at the expense of lower power density and potential mode coupling issues within waveguides. Converging beams, on the other hand, concentrate light rays towards a focal point upon exiting the source, leading to high power density but requiring precise alignment [22]. In our pursuit of developing a simple, stand-alone receiver system with manual alignment between the transmitter and receiver, collimated beams were the most suitable choice for our measurements.

Within the context of free-space propagation, a Gaussian beam wave traveling along the positive z -axis over a path of length L can be mathematically described as :

$$U_0(r, L) = \frac{A_0}{\Theta_0 + iA_0} \exp\left(ikL - \frac{r^2}{W^2} - i\frac{kr^2}{2F'}\right) \quad (4)$$

The parameters denoted by Θ_0 and A_0 are identified as transmitter beam parameters. This designation arises from their definition based on the beam's characteristics at the transmitter location. These parameters are expressed mathematically as :

$$\Theta_0 = 1 - \frac{L}{F_0}, \quad A_0 = \frac{2L}{kW_0^2} \quad (5)$$

2.1 OPTICAL BEAM

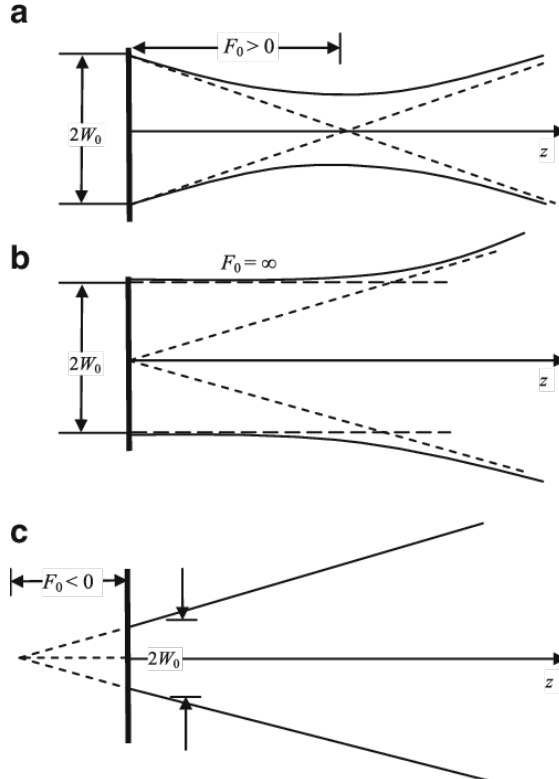


FIGURE 3: (a) convergent beam, (b) collimated beam, and (c) divergent beam [13]

The parameter Θ_0 characterizes the amplitude change within the wave caused by focusing or refraction at the transmitter. Conversely, Λ_0 represents the amplitude change due to diffraction occurring at the transmitter plane. Θ_0 is also referred to as the curvature parameter, while Λ_0 is known as the Fresnel ratio at the transmitter.

Equation (5) represent the effective beam radius and the phase front radius of curvature of the beam, respectively, both evaluated at the receiver plane. Given the defined transmitter beam parameters, the expressions for the receiver beam parameters (Θ and Λ) are provided as :

$$\Theta = 1 + \frac{L}{F'} = \frac{\Theta_0}{\Theta_0^2 + \Lambda_0^2} \quad (6)$$

$$\Lambda = \frac{2L}{kW^2} = \frac{\Lambda_0}{\Theta_0^2 + \Lambda_0^2} \quad (7)$$

2 THEORY

2.2 GEOMETRICAL APPROACH

2.2.1 FREE-SPACE LOSS

Free-space path loss (FSPL) is a dominant factor limiting the range and performance of FSO communication systems. It represents the attenuation experienced by the signal as it propagates through free space. The FSPL is quantified by the equation [23]:

$$L_{fsl} = 10 \log_{10} L_s = 10 \log_{10} \left(\frac{\lambda}{4\pi L} \right)^2 [dB] \quad (8)$$

where L_s represents the free-space loss factor, L is the link range (distance between transmitter and receiver) in meters, and λ denotes the wavelength of the optical source in meters. Due to the shorter wavelengths of light compared to radio frequencies, FSO systems experience significantly higher free-space loss compared to their RF counterparts.

To illustrate the impact of FSPL, consider a scenario with a 350m link and an optical source wavelength of a typical value (e.g., 1550 nm). Applying the equation, we obtain free-space loss factor, L_s value as 1.24×10^{-13} and L_{fsl} as -189dB. These values highlight the significant attenuation incurred by the signal even over relatively short distances in FSO systems.

2.2.2 TRANSMITTER GAIN AND RECEIVER GAIN

A geometrical representation of beam propagation is depicted in Figure 4 (referenced [13]). In our FSO system, Gaussian beams with varying FWHM divergence angles were employed. The specific divergence angles used were 330 μ rad, 545 μ rad, and 924 μ rad. The transmitter antenna diameter (D_T), detailed in Table 3, was calculated by [23] :

$$D_T = \sqrt{2} D_{e^{-2}} \approx 2.40 \times D_{FWHM} [cm] \quad (9)$$

These divergence angles served as the basis for estimating the received beam diameters at the receiver using purely geometric calculations, neglecting atmospheric effects. Following propagation over a distance of 350 meters, the diameters of the transmitted beams were determined geometrically (see Figure 4) using Equation 10. (See D_B Table 3)

$$D_B = L \times \theta_{FWHM} [cm] \quad (10)$$

By applying relationship between θ_{FWHM} and ω_0 for Gaussian beams, provided in Equation (2), the maximum possible axial gain can be expressed as in dB [23] :

$$g_{TX} = 10 \log_{10} \left(\frac{4\pi A_{TX}}{\lambda^2} \right) = 10 \log_{10} \left(\frac{4\sqrt{2}}{\theta_{e^2}} \right)^2 = 10 \log_{10} \left(\frac{4\sqrt{\ln 2}}{\theta_{FWHM}} \right)^2 [dB] \quad (11)$$

2.2 GEOMETRICAL APPROACH

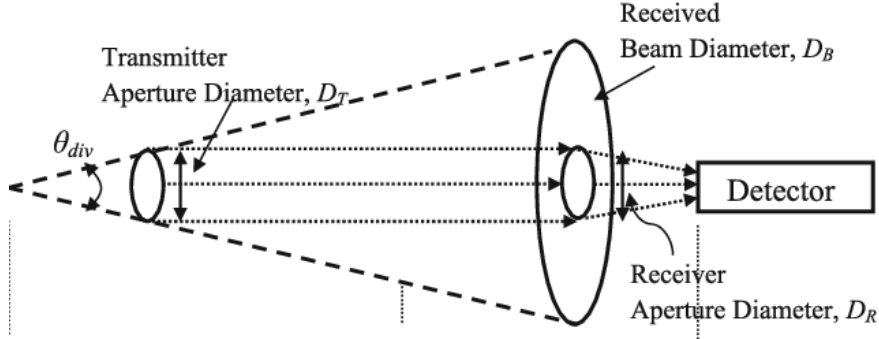


FIGURE 4: Beam Propagation geometrical representation [13]

FWHM divergence angle	D_T	D_B at 350m	D_R
$330\mu\text{rad}$	0.51cm	11.55 cm	2.54cm
$545\mu\text{rad}$	0.30cm	19.08 cm	2.54cm
$924\mu\text{rad}$	0.17cm	32.34 cm	2.54cm

TABLE 3: Beam Diameter with Distance

Where A_{TX} is the transmitter aperture area. For direct-detection receivers, assuming the receiver aperture area A_{RX} is smaller than the signal spot size (See Table 3), its gain can be directly calculated from this area [23].

$$g_{RX} = 10 \log_{10} \left(\frac{4\pi A_{RX}}{\lambda^2} \right) [dB] \quad (12)$$

Combining free-space loss from Equation(8), transmitter gain from Equation(11), and receiver gain from Equation(12), a geometric model expresses received optical power mathematically as in dB [23] :

$$P_{A_{RX}} = P_{TX} + G_{TX} + G_{RX} + L_{fsl} = P_{TX} + 10 \log_{10} \left(\frac{4 \cdot \ln 2}{\pi} \cdot \frac{A_{RX}}{(L \cdot \theta_{FWHM})^2} \right) [dB] \quad (13)$$

This section explored the geometric approach to Gaussian beam propagation in free-space, excluding atmospheric effects. Three distinct divergence angles ($330\mu\text{rad}$, $545\mu\text{rad}$, and $924\mu\text{rad}$) was considered. For each divergence angle, the free-space loss, transmitter antenna gain, and receiver antenna gain were calculated and presented in Section 2.7. A more comprehensive discussion of Gaussian beam propagation in free-space, incorporating atmospheric effects, will be provided in the next chapter.

2 THEORY

2.3 ATMOSPHERIC TURBULENCE

Atmospheric conditions can significantly impact the optical signals employed in free-space optical communication. These factors include sunlight, wind, cloud, humidity, precipitation (rain, snow, sleet), atmospheric obscurants (fog, haze), and particulate matter (pollution). Various elements can interfere with the transmission of laser beams through the atmosphere. Laser beams, propagating through Earth's atmosphere, encounter disruptions in received signals [7], [15].

2.3.1 ATTENUATION

Atmospheric attenuation significantly impacts the performance and availability of FSO links. This attenuation arises from the absorption and scattering of light by atmospheric constituents, excluding specific effects caused by environmental factors like fog, snow, and rain. These effects degrade the intensity of the transmitted beam as it propagates through the atmosphere. For a collimated beam with an initial intensity of $I(0)$, Beer's Law offers a quantitative means to describe the atmospheric transmittance (T_{atm}). This parameter relates to the overall attenuation experienced by the beam after traversing a path length L [14], [24]:

$$T_{atm} = I(L)/I(0) = \exp(-\tau) = \exp(-\alpha L) \quad (14)$$

where α represents the atmospheric attenuation coefficient, a constant value for scenarios with a horizontally propagating beam through the atmosphere. The optical depth τ is another way to express atmospheric loss (L_{atm}) in decibels (dB) [14]:

$$L_{atm} = 10 \log(T_{atm}) = 4.343\alpha L \quad [dB] \quad (15)$$

Background radiation, including direct sunlight and sky radiance, significantly impacts the SNR of the received optical signal. Additionally, cloud cover can severely attenuate the signal, hindering its detection. To mitigate the detrimental effects of background radiation, optical bandpass filters are commonly employed in front of photodiodes [14]. In our system, we implemented an optical narrow bandpass filter with a 12 nm bandwidth for this purpose. While the bandpass filter provides initial mitigation, our measurement approach addresses background sunlight meticulously with additional methods. These methods will be elaborated upon in Chapter 4.

2.3.2 ATMOSPHERIC TURBULENCE

Atmospheric turbulence is a dominant factor causing distortion in optical wave propagation. Random fluctuations in air temperature and pressure result in inhomogeneities of the refractive index. These inhomogeneities affect the amplitude and phase of the optical beam, perturbing its wavefront (as illustrated in Figure 5). These refractive index variations arise from turbulent eddies, which are localized regions of air with distinct sizes, temperatures, densities, and consequently, refractive indices. These eddies, generated by a combination of wind shear, convection currents,

2.3 ATMOSPHERIC TURBULENCE

and temperature variations, are transient phenomena. l_0 denotes inner scale of turbulence and L_0 denotes outer scale of turbulence. Their random nature disrupts the laser beam's phase front, leading to phase-shifted arrivals at the receiver plane [7], [15] , [25].

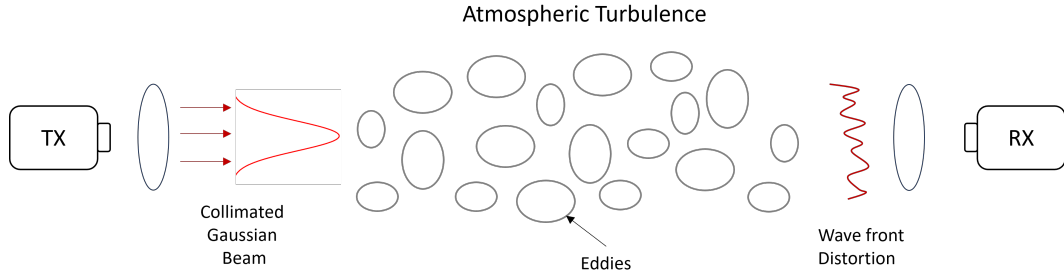


FIGURE 5: Atmospheric Turbulence

Atmospheric turbulence cells characterized by eddy sizes (l_0 , L_0) can induce various detrimental effects on the propagating beam. These effects encompass beam spreading, beam wander, and beam scintillation. Collectively, these phenomena contribute to variations in the gaussian beam, consequently impacting the received signal power and quality [15], [26], [13].

- Beam Wander: Large eddies (L_0), exceeding the beam diameter (W), can cause deflection of the entire beam, potentially leading to misalignment with the receiver aperture.
- Beam Scintillation: Eddies with dimensions comparable to the beam diameter act as dynamic lenses, inducing random fluctuations in the beam's irradiance at the receiver.
- Beam Spreading: Smaller eddies (l_0), with sizes smaller than the beam diameter (W), cause a minor portion of the beam to undergo independent diffraction and scattering, resulting in a reduction of the received power density and a distortion of the wavefront.

The propagation of an optical beam through the atmosphere can be modeled using the wave equation :

$$\nabla^2 U + k^2 n^2(r)U = 0 \quad (16)$$

Where $\nabla^2 U$ represents the Laplacian operator acting on the electric field U , $k (=2\pi/\lambda)$ is wave number and $n(r)$ signifies the refractive index of the medium, which is typically a random function of space due to atmospheric turbulence. The refractive index of the atmospheric medium, $n(r)$, exhibits a random variation across space due to the prevailing temperature and pressure conditions. This dependence can be expressed mathematically through the following equation

$$n(r) = 1 + 7.66 \times 10^{-6} (1 + 7.52 \times 10^{-3} \lambda^{-2}) \frac{P'(r)}{T'(r)} \quad (17)$$

2 THEORY

The refractive index (n) of the atmosphere depends on the prevailing wavelength (λ) in meters, atmospheric pressure (P') in millibars (mbar), and temperature (T') in Kelvin. The structure function ($D_n(r)$) for the refractive index fluctuations is expressed as:

$$D_n(r_n) = C_n^2 r^{2/3} \quad (18)$$

where C_n^2 , referred to as the refractive index structure constant, quantifies the intensity of these fluctuations.

The Kolmogorov power spectrum ($\Phi_n(\kappa)$) for the refractive index fluctuations, as a physical description of the wavefront perturbations induced by the atmosphere, characterized by outer scale (L_0) and inner scale (l_0) of eddies, defined by the equation:

$$\Phi_n(\kappa) = 0.033C_n^2\kappa^{-11/3} \left(\frac{1}{L_0} \ll \kappa \ll \frac{1}{l_0} \right) \quad (19)$$

κ is the scalar spatial frequency (in rad/m) and the refractive index structure constant, denoted by C_n^2 , serves as a quantitative measure for the intensity of refractive index fluctuations within the atmosphere. The Hufnagel-Valley 5/7 (HV5/7) model, a widely recognized model based on empirical atmospheric scintillation data, is presented below to describe this parameter [15], [27].

$$C_n^2(h) = 0.00594 \left(\frac{v}{27} \right)^2 (10^{-5}h)^{10} \exp\left(\frac{-h}{1000}\right) + 2.7 \times 10^{-16} \exp\left(\frac{-h}{1500}\right) + A \exp\left(\frac{-h}{100}\right) \quad (20)$$

h : height [km]

v : wind speed [m/s]

A : nominal value of $C_n^2(0)$ at the ground [$m^{-2/3}$]

$A = 1.7 \times 10^{-14} m^{-2/3}$, when $v = 21$ m/s

Several existing models describe the refractive index structure, including the Fried model, Hufnagel-Stanley model, Hufnagel Valley model, Hufnagel-Andrews-Phillips model, Submarine Laser Communication (SLC) model, PAMELA model, and Clear 1 according to its applications and its improved models [28], [29], [30], [31]. However, for the purposes of this work, we will solely employ the Hufnagel-Valley 5/7 (HV5/7) model.

C_n^2 holds a constant value for horizontal paths over short distances, typically ranging from $10^{-17} m^{-2/3}$ (weak turbulence) to $10^{-13} m^{-2/3}$ (strong turbulence). However, various environmental factors such as, temperature, pressure, humidity, location, time of day, wind speed, and solar heating, influence C_n^2 value [15]. In prior research [32], seasonal variations exhibit a weaker effect on scintillation compared to diurnal and short-term meteorological influences. Winter experiences less intense and variable turbulence. Diurnally, summer turbulence demonstrates a strong correlation with sunshine and boundary-layer warming. The path-averaged C_n^2 in

2.3 ATMOSPHERIC TURBULENCE

this context ranges from $5 \times 10^{-15} m^{-2/3}$ to $10^{-12} m^{-2/3}$, peaking in the late afternoon. As atmospheric conditions stabilize towards evening, scintillation intensity follows a daily cycle, rising with morning warming, reaching a peak around 11 AM, and then subsiding. More detailed measurement data for C_n^2 , specific to the DLR-OGS site location, can be found in [33].

A visual representation of the various atmospheric effects impacting a free-space propagating optical beam is provided in Figure 6. These effects can be broadly classified into two categories: attenuation and distortion, both caused by atmospheric turbulence. Attenuation mechanisms, such as absorption and scattering, lead to a reduction in the average power of the received signal. In contrast, distortion effects introduce fluctuations in the received signal around its mean value. These fluctuations can arise from phenomena like beam spreading, beam wander and scintillation, which will be explored in detail in subsequent sections.

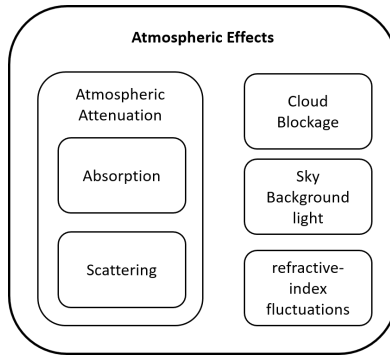


FIGURE 6: Atmospheric Effects

2 THEORY

2.4 BEAM EFFECTS

This section delves deeper into the effects of atmospheric turbulence on optical fields. Understanding the statistical properties of the optical field in turbulent environments is essential. By analyzing these properties, we can derive important statistical quantities that characterize the behavior of the beam under turbulent conditions. To illustrate the relationships between these statistical quantities and the resulting effects of turbulence, Figure 7, adapted from Andrews [7], serves as a valuable guide. This flowchart visually depicts the influence of turbulence on various aspects of the optical field and the resulting consequences.

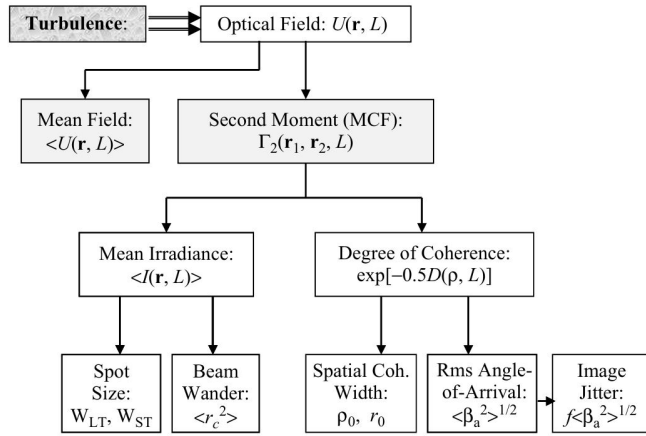


FIGURE 7: Flowchart of Optical Turbulence Effects on the Optical Field [7]

The received field, denoted by $U(r, L)$, as defined in Equation (4), is characterized by two parameters. The first parameter, L , represents the propagation distance along the positive z -axis. This distance extends from the transmitter's emitting aperture to the receiver. The second parameter, r , is a vector in the receiver plane, perpendicular to the propagation axis. Under the conventional Rytov approximation [34], the received optical field at a specific link range, L , from the transmitter can be described as [13], [15], [7] :

$$\begin{aligned} U(r, L) &= U_0(r, L) \exp[\Psi(r, L)] \\ &= U_0(r, L) \exp[\Psi_1(r, L) + \Psi_2(r, L) + \dots] \end{aligned} \quad (21)$$

We consider the free-space diffraction-limited Gaussian beam wave at the receiver, denoted by $U_0(r, L)$. Due to random variations in the refractive index along the propagation path L , the actual received field experiences complex phase fluctuations, which we represent by $\Psi(r, L)$. To analyze these fluctuations, we decompose them into two perturbation terms: $\Psi_1(r, L)$ and $\Psi_2(r, L)$. The first term, $\Psi_1(r, L)$, represents the first-order perturbation, while the second term, $\Psi_2(r, L)$, captures the second-order perturbation. The expression for the first-order moment is subsequently provided [13], [15] :

$$\langle U(r, L) \rangle = U_0(r, L) \langle \exp[\Psi(r, L)] \rangle \quad (22)$$

Where the first moment of the field, denoted by $\langle U(r, L) \rangle$, represents the ensemble average of the wave field, indicated by the angled brackets $\langle \rangle$. This ensemble average signifies the coherent portion of the wave, also known as the mean field of the optical wave. The coherent portion carries the essential information of the signal and plays a critical role in determining the performance of the communication system.

MUTUAL COHERENCE FUNCTION

The second moment, Mutual Coherence Function (MCF), $I_2(r_1, r_2, L)$, is defined as [13], [15]:

$$\begin{aligned} I_2(r_1, r_2, L) &= \langle U(r_1, L) \langle U^*(r_2, L) \rangle \rangle \\ &= U_0(r_1, L) U_0^*(r_2, L) \langle \exp[\Psi(r_1, L) + \Psi^*(r_2, L)] \rangle \end{aligned} \quad (23)$$

Within the receiver plane, we consider two observation points denoted by r_1 and r_2 . The asterisk (*) denotes the complex conjugate, while the angled brackets ($\langle \rangle$) represent the ensemble average. This ensemble average can be calculated using the following equation [13]:

$$\langle \exp(\Psi) \rangle = \exp[\langle \Psi \rangle + \frac{1}{2} (\langle \Psi^2 \rangle - \langle \Psi \rangle^2)] \quad (24)$$

the MCF for a Gaussian beam wave propagating through turbulence exhibits statistical inhomogeneity. This signifies that the MCF depends not only on the scalar separation distance between two observation points, r_1 and r_2 , within the receiver plane, but also on their specific positions relative to the beam profile. In the special case where these points are symmetrical ($r_1 = r_2 = r$), a direct relationship can be established between the MCF and the mean irradiance ($\langle I(r, L) \rangle$) defined in Equation (25), where the mean irradiance ($\langle I(r, L) \rangle$) influenced by turbulence is entirely determined by the beam spot size. This relationship allows us to quantify the extent of beam spreading induced by turbulence, where the beam widens beyond its inherent diffraction limit [15], [14].

$$\begin{aligned} \langle I(r, L) \rangle &= I_2(r, r, L) \\ &\approx \frac{W_0^2}{W_e^2} \exp\left[-\frac{2r^2}{W_e^2}\right] \end{aligned} \quad (25)$$

The diameter of the beam at the receiver plane is denoted by W and the effective beam spot size, denoted as W_e in meters (m), characterizes the area over which the optical field is concentrated. The specific expression for W_e is given by [7], [14]:

2 THEORY

$$W_e^2 = W^2(1 + T) \quad (26)$$

The parameter T captures the additional spreading of the beam due to turbulence. This parameter is influenced by both the strength of the turbulence and the specific beam path (horizontal, uplink, downlink). For the specific case of a horizontal path with constant C_n^2 (refractive index structure constant, defined in Equation (20), the expression for T can be derived using the Kolmogorov spectrum model, introduced in Equation(19) [14], [7] :

$$T = 5.32 \sigma_\chi^2 \Lambda^{5/6} \quad (27)$$

The variance of the log-normal amplitude, denoted by σ_χ^2 , will be introduced in Equation (40) and characterizes the path-dependent intensity fluctuations. The parameter Λ , previously defined in Equation (7), represents a beam-related quantity.

The effective waist, denoted by W_e (also referred to as the long-term spot size, W_{LT}), represents the combined effect of all instantaneous beam profiles reaching the receiver over a long period. This encompasses both the natural diffraction in free space and the additional spreading caused by turbulent eddies smaller than the beam itself. Beyond this combined spreading, a phenomenon known as beam wandering comes into play. This effect, caused by large-scale turbulent eddies, results in the beam center deviating from its original path and undergoing a wandering motion around an average position. The root-mean-square (rms) distance of this wandering motion, denoted by $\langle r_c^2 \rangle$, characterizes the influence of beam wander. By incorporating this effect, the effective mean waist can be expressed using the beam wander displacement variance, $\langle r_c^2 \rangle$, as [35], [14], [7]:

$$W_e^2 (= W_{LT}^2) = W_{ST}^2 + \langle r_c^2 \rangle \quad (28)$$

For a horizontal link, where $W_{ST} > W_0$, the rms centroid displacement of the beam, $\langle r_c^2 \rangle$, can be expressed as [14], [7] :

$$\langle r_c^2 \rangle = 2.87 C_n^2 L^3 W_0^{-3} \quad (29)$$

The intensity of the beam can be modeled using a beta distribution, as described in previous works [36], [37].

$$f_I = \beta \cdot I^{\beta-1}, (0 \leq I \leq 1, \beta > 0) \quad (30)$$

The quantity $\langle I \rangle$ is not normalized by its mean value. The expression for this mean value is subsequently provided as [36], [37]:

$$\langle I \rangle = \frac{\beta}{\beta + 1} \quad (31)$$

Under the assumption of weak turbulence, the shape parameter, denoted by β , of the beta distribution employed to model pointing errors arising from beam wander can be expressed as [36], [37]:

$$\beta = \frac{\theta_{1/e^2}^2 / 2}{2\theta_{BW}^2} \quad (32)$$

Where θ_{1/e^2} , defined in Section 2.1 as ω_0 , represents the full-angle beam divergence at which the beam intensity drops to $1/e^2$ of its peak value for a well-collimated laser beam. θ_{BW}^2 is the angular beam wander for an uplink propagation, given as Equation(33) [36]. While our analysis focuses on a horizontal link, for simplicity, we adopt the same equation used for uplink propagation to model the angular beam wander.

$$\theta_{BW} = \frac{\sqrt{\langle r_c^2 \rangle}}{L} \quad (33)$$

The beam suffers an additional loss due to beam wandering. This excess loss can be expressed in decibel as [36]. [23] :

$$L_{bw} = 10 \log_{10} \left(\frac{\beta}{\beta + 1} \right) [dB] \quad (34)$$

SPATIAL COHERENCE

The MCF offers more than just predicting beam spreading due to turbulence, as reflected in the mean irradiance. It also provides valuable insights into the spatial coherence properties of the received wave. The MCF is closely linked to the wave structure function (WSF), which is primarily influenced by the phase structure function. For observation points located symmetrically within the beam spot size ($r_2 = -r_1$), the WSF for a Gaussian-beam wave on either an uplink or downlink path can be defined as, $D(\rho, L)$. where ρ represents the separation distance between the observation points. To illustrate this concept, the MCF for two observation points, r_1 and r_2 with a separation distance of ρ can be expressed as [35] [38]:

$$\Gamma_2(\rho, L) = \exp \left[-\frac{1}{2} D(\rho, L) \right] \quad (35)$$

Here, L represents the propagation distance and $D(\rho, L)$ is the WSF, represents the real part of a complex quantity $\mathcal{D}(\rho, L)$, expressed mathematically as [7]:

$$D(\rho, L) = \text{Re}[\mathcal{D}(\rho, L)] \quad (36)$$

The spatial coherence radius, denoted by ρ_0 , is defined as the specific separation distance, ρ , at which the WSF equals 2. This relationship is expressed as $D(\rho_0, L) = 2$. In practice, the atmospheric coherence width, $r_0[m]$, is commonly defined as 2.1 times the spatial coherence

2 THEORY

radius, resulting in $r_0 = 2.1\rho_0$ [7], [35]. This atmospheric coherence width provides a measure of the typical separation distance over which different parts of the wavefront remain significantly correlated. Building on this concept, expressions for the atmospheric coherence width, r_0 , for both plane waves and spherical waves with horizontal link were derived as [35], [7], [39], [40], [41]:

$$r_0 = (0.423k^2C_n^2L)^{-3/5} \text{ [m]} \quad (\text{Plane wave}) \quad (37)$$

$$r_0 = (0.158k^2C_n^2L)^{-3/5} \text{ [m]} \quad (\text{Spherical wave}) \quad (38)$$

The atmospheric coherence width, r_0 , depends on several factors. One key parameter is the refractive index structure constant C_n^2 , introduced in Equation(20), which characterizes turbulence strength. For a horizontal link, the refractive index structure constant, C_n^2 , remains constant throughout the propagation path. Another factor is the wave number, denoted by $k = 2\pi/\lambda$, where λ is the wavelength of the beam. Due to this dependence, the r_0 exhibits a proportionality to the wavelength raised to the power of $6/5$ (i.e, $r_0 \propto \lambda^{6/5}$). The wavefront properties themselves also play a role [14], [7].

To simplify the analysis and focus on the core principles, we employed the equations for spherical and plane waves instead of the more complex equation for a Gaussian wave. The atmospheric coherence width, r_0 , for a horizontal link of 350 m and a wavelength of 1550 nm was calculated with several different C_n^2 constant values. These results are presented in Table 4. Subsequently, these r_0 values will be employed to determine the optimal separation distance between the two transmitters. A comparison between the calculated values and the actual measurement data will be presented in Section 4.2.

C_n^2	r_0 (Plane wave)	r_0 (Spherical wave)
$1.7 \cdot 10^{-14}$	0.107 [m]	0.194 [m]
$3.4 \cdot 10^{-14}$	0.07 [m]	0.127 [m]
$6.8 \cdot 10^{-14}$	0.046 [m]	0.084 [m]
10^{-13}	0.037 [m]	0.067 [m]

TABLE 4: atmospheric coherence width (r_0) with $L=350\text{m}$, $\lambda = 1550\text{nm}$

2.5 SCINTILLATION AND PROBABILITY DENSITY FUNCTION

2.5.1 POWER SCINTILLATION INDEX

Scintillation refers to the irradiance fluctuations within the received beam's cross-section after propagating through atmospheric turbulence. It is measured by the power scintillation index (or normalized variance of irradiance), denoted by σ_p^2 . This parameter significantly impacts system performance by causing deep fades and reducing the signal-to-noise ratio, as defined by the equation [15] , [8]:

$$\sigma_p^2 = \frac{\langle P^2 \rangle - \langle P \rangle^2}{\langle P \rangle^2} = \frac{\langle P^2 \rangle}{\langle P \rangle^2} - 1 \quad [\text{unitless}] \quad (39)$$

P is optical power and $\langle \cdot \rangle$ denotes average

The relationship between the power scintillation index (σ_p^2) and the log-amplitude variance (σ_χ^2) can be expressed mathematically as :

$$\sigma_p^2 \approx 4\sigma_\chi^2, \text{ for } \sigma_\chi^2 \ll 1 \quad (40)$$

2.5.2 MODIFIED RYTOV APPROXIMATION

The modified Rytov Approximation is applicable to weak to strong atmospheric fluctuations. For this, the following assumptions are necessary [13], [42] :

- The small-scale (diffracting) and large-scale (refracting) fluctuations (The received irradiance fluctuations can be modulated)
- The small- and large-scale processes are independent (no coherence)
- The Rytov method for optical scintillation is valid even in the saturation regime by using spatial frequency filters to account for the loss of spatial coherence of the optical wave in strong fluctuation conditions.

the normalized power can be expressed as $P = XY$, where X and Y are independent random variables. These variables arise from the influence of large-scale and small-scale turbulent eddies, respectively. It is further assumed that both X and Y have a unit mean ($\langle X \rangle = \langle Y \rangle = 1$). Consequently, the normalized power itself has a mean value of 1 ($\langle P \rangle = 1$), The second moment of the received power ($\langle P^2 \rangle$) is given by ($\because \langle X \rangle^2 = \langle Y \rangle^2 = 1$):

$$\langle P^2 \rangle = \langle X^2 \rangle \langle Y^2 \rangle = (1 + \sigma_x^2)(1 + \sigma_y^2) \quad (41)$$

By applying the Equation41 to 39, the power scintillation index can be expressed as with $\langle P \rangle^2 = 1 (\because \langle P \rangle = 1)$:

2 THEORY

$$\begin{aligned}\sigma_p^2 &\approx (1 + \sigma_x^2)(1 + \sigma_y^2) - 1 \\ &= \sigma_x^2 + \sigma_y^2 + \sigma_x^2\sigma_y^2\end{aligned}\quad (42)$$

Due to X and Y are independent $\sigma_x^2\sigma_y^2 = 0$, and the equation can be simplified as :

$$\sigma_p^2 = \sigma_x^2 + \sigma_y^2 \quad (43)$$

Because $\langle P \rangle^2 = \langle X \rangle^2 = \langle Y \rangle^2 = 1$, the scintillation index $\sigma_p^2, \sigma_x^2, \sigma_y^2$ can be written in terms of log variance :

$$\begin{aligned}\sigma_p^2 &= \exp(\sigma_{lnp}^2) - 1 \\ \sigma_x^2 &= \exp(\sigma_{lnx}^2) - 1 \\ \sigma_y^2 &= \exp(\sigma_{lny}^2) - 1\end{aligned}\quad (44)$$

Therefore, the power scintillation index (σ_p^2) became :

$$\sigma_p^2 = \exp(\sigma_{lnx}^2 + \sigma_{lny}^2) - 1 \quad (45)$$

In weak fluctuation ($\sigma_p^2 < 1$), the power scintillation index reduces to the limiting form :

$$\sigma_p^2 \approx \sigma_{lnp}^2 \approx \sigma_{lnx}^2 + \sigma_{lny}^2 \quad (46)$$

Building on the relationship between scintillation index and log-amplitude variance, the variance of log-irradiance (also known as Rytov variance), denoted by σ_R^2 , can be further connected to the scintillation index σ_p^2 through the following equation :

$$\sigma_p^2 = \exp(\sigma_R^2) - 1 \approx \sigma_R^2, \text{ for } \sigma_R^2 \ll 1 \quad (47)$$

While a comprehensive, rigorous theory for optical wave propagation through turbulent media remains elusive, a good understanding exists within specific asymptotic regimes. For models employing infinite plane waves or spherical waves (point sources), the weak turbulence regime in the atmosphere can be characterized by the Rytov variance, defined as :

$$\sigma_R^2 = 1.23 C_n^2 k^{7/6} L^{11/6} \text{ [unitless]} \quad (48)$$

The relationship between scintillation index (σ_p^2) and Rytov variance (σ_R^2) depends on the type of wave employed in the model. For plane waves, σ_p^2 directly corresponds to σ_R^2 ($\sigma_p^2 = \sigma_R^2$). However, for spherical waves, the scintillation index is related to the Rytov variance by a factor of 0.4 ($\sigma_p^2 = 0.4\sigma_R^2$). [15], [8]

2.5 SCINTILLATION AND PROBABILITY DENSITY FUNCTION

2.5.3 PROBABILITY DENSITY FUNCTION

Under weak turbulence conditions, where the scintillation index (σ_p^2) is less than 1, the lognormal model is widely employed due to its relative simplicity in mathematical calculations. This model characterizes the PDF of the received power (P) as :

$$f(P) = \frac{1}{\sqrt{2\pi\sigma_p^2 P}} \exp \left[-\frac{(\ln(P) - \mu)^2}{2\sigma_p^2} \right] \quad (49)$$

where μ represents the mean of the natural logarithm of the power $\langle \ln(P) \rangle$. Based on Equation 40, $\sigma_p^2 = 4\sigma_\chi^2$, revised expression can be written as :

$$f(P) = \frac{1}{2\sqrt{2\pi\sigma_\chi^2 P}} \exp \left[-\frac{(\ln(P) - \mu)^2}{8\sigma_\chi^2} \right] \quad (50)$$

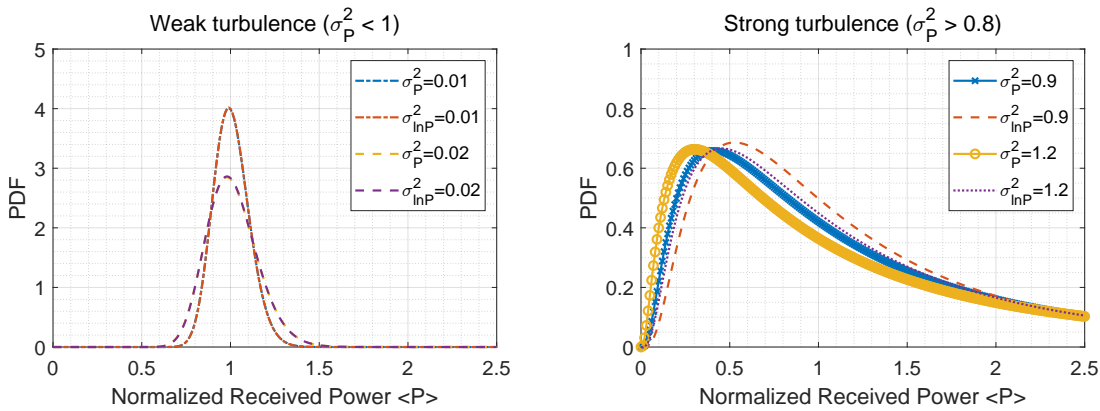


FIGURE 8: Rytov Approximation Log-normal Distributions with weak and strong turbulence

Figure 9 illustrates the log-normal distribution for power scintillation index (σ_p^2) and log-amplitude variance (σ_R^2) in both weak turbulence ($\sigma^2 < 1$) and strong turbulence ($\sigma^2 > 1$) regimes. The figure presents these quantities independently. The graph reveals that the distributions for (σ_p^2) and log-amplitude variance (σ_R^2) are nearly identical in the weak turbulence scenario for σ^2 values of 0.01 and 0.02. However, in the strong turbulence regime, even a value of $\sigma^2 = 0.9$ (which remains less than 1) exhibits slight discrepancies between the distributions of these two quantities. This observation suggests that the Rytov approximation is only valid under weak turbulence conditions. Given that our scenario falls within the weak turbulence regime with an expected scintillation index of 0.01-0.03, the Rytov approximation and its associated log-normal distributions hold true for our analysis.

2 THEORY

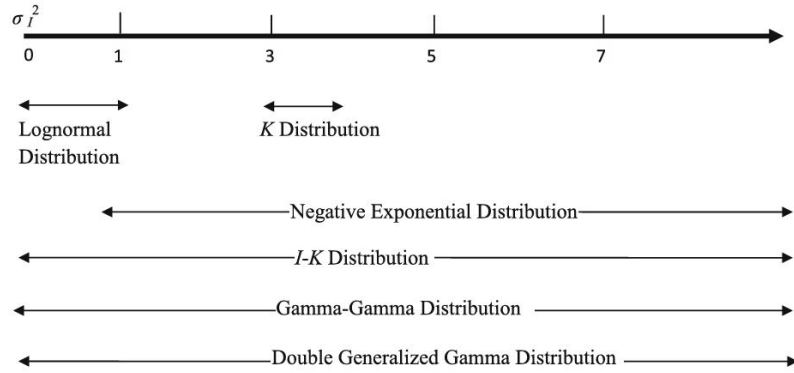


FIGURE 9: Various distributions for scintillation index [13]

Figure 9 [13] depicts the behavior of various probability distributions as they relate to the scintillation index. The figure illustrates that the Log-normal distribution remains applicable only within the weak turbulence regime, characterized by $(\sigma^2 < 1)$. For scenarios with higher scintillation indices ($\sigma^2 > 1$), the Log-normal distribution loses its validity. In such cases, alternative distributions like the I-K [43] and Gamma-Gamma distributions [44] become more suitable for modeling the phenomenon. Additional details regarding these distributions can be found in a dedicated reference source [45].

Previous research has established a method for deriving scintillation loss within a log-normal fading channel.[46] This method incorporates two key parameters: the average power (P_{mean}) and a loss threshold value (p_{thr}). Figure 10 visually represents the relationship between the mean power(P_{mean}), the loss fraction (p_{thr}) (obtained by integrating the tail of the probability distribution function - PDF), and the corresponding scintillation loss ($Loss_{sci}$).

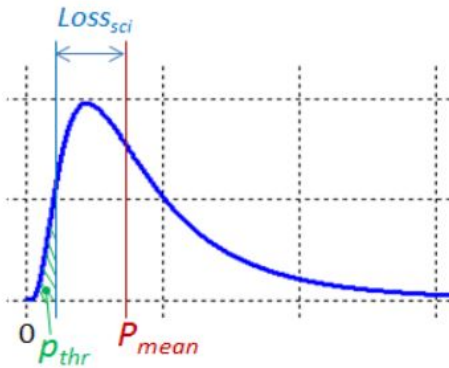


FIGURE 10: Scintillation loss [46]

The corresponding expression for scintillation loss (denoted as L_{sci} in dB) is derived considering

2.5 SCINTILLATION AND PROBABILITY DENSITY FUNCTION

a log-normal probability density function (PDF) for the power vector, as expressed in [46] , [47]:

$$L_{sci} = -4.343 \left[erfinv(2P_{thr} - 1) \sqrt{2\ln(\sigma_P^2 + 1)} - 0.5 \ln(\sigma_P^2 + 1) \right] [dB] \quad (51)$$

Across a horizontal link distance ranging from 340 meters to 360 meters, scintillation loss (L_{sci}) values were calculated within a range of -0.268 dB to -0.283 dB. This calculation employed Equation (48) and utilized the Rytov variance (σ_R^2) obtained using Equation (20). The refractive index structure constant (C_n^2) value, was $1.72 \times 10^{-14} m^{-2/3}$ as determined by the H-V 5/7 model (detailed in Section 2.3).

2 THEORY

2.6 FADES

Building upon the discussion of atmospheric turbulence and its effects on optical signal presented in Section 2.3, this section focuses on the phenomenon of scintillation. Scintillation, as previously introduced in Section 2.5, arises during beam propagation and manifests as power fluctuations at the receiver. These fluctuations can lead to signal fading events, where the received power falls below a predetermined threshold.

Within this section, we designate P_{th} , as the threshold level for the received power (P). Furthermore, we introduce the concept of the fade threshold parameter, denoted by f_{th} in Equation(52). This parameter signifies the decibel (dB) level below the average received power ($\langle P \rangle$) [4], [48].

$$f_{th} = 10 \log_{10} \left(\frac{\langle P \rangle}{P_{th}} \right) [\text{dB}] \quad (52)$$

Our analysis assumes that the PDF of the received power fluctuations mirrors that of the irradiance fluctuations. While various models exist to describe irradiance fluctuations. We focus on the log-normal model applicable to scenarios with weak scintillation. The log-normal model generally predicts lower fade probabilities [15]. The fade probability, also known as probability of miss, quantifies the probability of the received power falling below the predetermined threshold level. This can be expressed as cumulative distribution of the received power [49]:

$$F(P) = \frac{1}{2} \left\{ 1 + \operatorname{erf} \left[\frac{\ln P - \mu}{\sqrt{2}\sigma_P} \right] \right\} \quad (53)$$

where $\operatorname{erf}(x)$ represents the error function defined as [50] :

$$\operatorname{erf}(x) = \frac{2}{\sqrt{\pi}} \int_0^x \exp(-t^2) dt \quad (54)$$

Additionally, the symbol μ signifies the average of the natural logarithm of the received power, denoted by $\langle \ln P \rangle$, which was previously introduced in Equation (49). Leveraging Equation (52), we can rewrite Equation (53) as:

$$F(P) = \frac{1}{2} \left\{ 1 + \operatorname{erf} \left[\frac{\ln \left(\frac{P}{P_{th}} \right) - 0.23 f_{th}}{\sqrt{2}\sigma_P} \right] \right\} \quad (55)$$

The probability of the fading allows for the derivation of the expected number of fades per unit time and their corresponding mean duration, providing valuable metrics for evaluating system performance. Previous research in [4] explored the estimation of fractional fade time, expected

2.6 FADES

number of fades, and mean fade duration for uplink, downlink, and horizontal link with various models. our analysis specifically addresses signal fades encountered in line-of-sight terrestrial links with weak turbulence regime.

The expected number of fades per unit time, denoted by $\langle n(P_{th}) \rangle$, is defined in Equation(56). This metric represents the frequency of negative crossings, where the received power falls below a predetermined threshold level, P_{th} . Here, v_0 represents a quasi-frequency parameter that relates to the width of the normalized log-intensity power spectrum. While a comprehensive discussion of v_0 falls outside the scope of this study as it does not directly influence the probability of fades, the concept is explored in detail within the references [4] and [48].

$$\langle n(P_{th}) \rangle = v_0 \exp \left[-\frac{\left\{ \ln \left(\frac{P}{P_{th}} \right) - 0.23 f_{th} \right\}^2}{2\sigma_P^2} \right] \quad (56)$$

Furthermore, the mean duration of a fade event, denoted by $\langle t(P_{th}) \rangle$, is defined as the average time the received beam intensity remains below the threshold f_{th} . This duration can be determined using the expression:

$$\langle t(P_{th}) \rangle = \frac{f(P \leq P_{th})}{\langle n(P_{th}) \rangle} \quad (57)$$

Where $f(P)$ is the PDF of the received power, introduced in Equation(49).

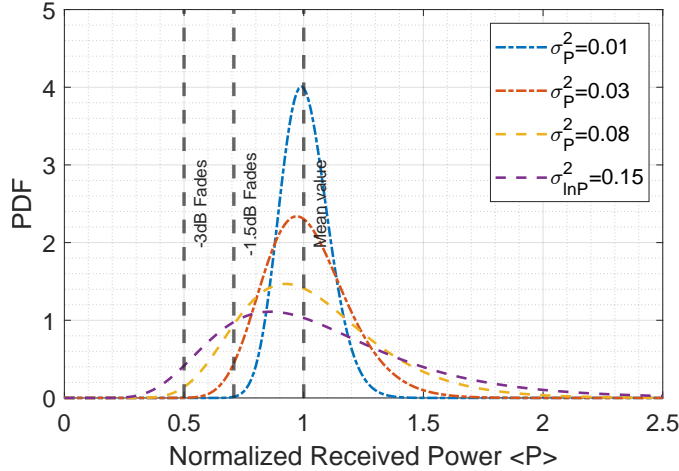


FIGURE 11: Fades threshold

Figure 11 depicts the PDF of the normalized received power, defined in Equation(49) with various PSI values. Two specific fade thresholds are provided: -3 dB and -1.5 dB. As evident from the

2 THEORY

graph, increasing PSI values lead to a larger area falling below both thresholds, indicating a higher probability of fade events. Based on the refractive index parameter discussed in Section 2.3, we anticipate PSI values around 0.01 to 0.08. The PDF with PSI value of 0.01 in the figure exhibits minimal fades with the -3 dB threshold. This minimal fade scenario makes it challenging to investigate fade events effectively. In previous research [51] with 61 km horizontal link scenarios suggests a fade threshold (f_{th}) of -3 dB. However, in our scenarios, we employed a lower threshold of -1.5 dB due to low PSI values with the short link distance of 350 meters, which is expected to result in a lower frequency of fade events.

2.7 LINK BUDGET

The total received power incorporates several factors, including transmitter and receiver gains, as well as losses due to beam wander, free-space loss, atmospheric attenuation effects, and atmospheric scintillation. Determining the cumulative impact involves summing all link budget components expressed in decibels (dB) as Equation(58). This calculation stems from a comprehensive link budget analysis conducted earlier [23]. The link budget assessment thoroughly considers all elements influencing signal transmission over the optical link.

$$P_{Rx} = P_{Tx} + G_{Rx} + G_{Tx} + L_G + L_{bw} + L_{fsl} + L_{atm} + L_{sci} \quad [dBm] \quad (58)$$

P_{Rx} received optical power [dBm]	L_{bw} beam wander loss [dB] eq
P_{Tx} transmit optical power [dBm]	L_{fsl} free-space loss [dB] eq
G_{Rx} receiver antenna gain [dB]	L_{atm} atmospheric attenuation loss [dB]
G_{Tx} transmitter antenna gain [dB]	L_{sci} scintillation loss [dB]
L_G optical geometric loss [dB]	

The individual terms contributing to the overall link loss were calculated using the corresponding equations referenced in previous sections. The transmit power (P_{Tx}) was set to 1.6 mW, which translates to 2 dBm using the conversion formula (Equation 59). Specific equations were employed for each term: Equation (11), (12), (8), (34), (15), and (51) for G_{Tx} , G_{Rx} , L_{fsl} , L_{BW} , L_{atm} , and L_{sci} , respectively. Notably, that a specific value of $\beta = 2.89$ was utilized for the beam wander loss calculation L_{BW} due to the observation that different divergence angles resulted in approximately the same β value within this context. Additionally, L_{atm} with a value of -1 dB chosen based on statistics from a reference source [23].

$$dBm = 10\log_{10} [mW] \quad (59)$$

The results of the link budget calculations for the optical link operating over a range of 100 meters to 400 meters are presented in Figure 13. For improved visualization of the data across a wide range of values, the y-axis is plotted on a logarithmic scale. The specific values corresponding to our target link distance of 350 meters are detailed in Table 5.

2 THEORY

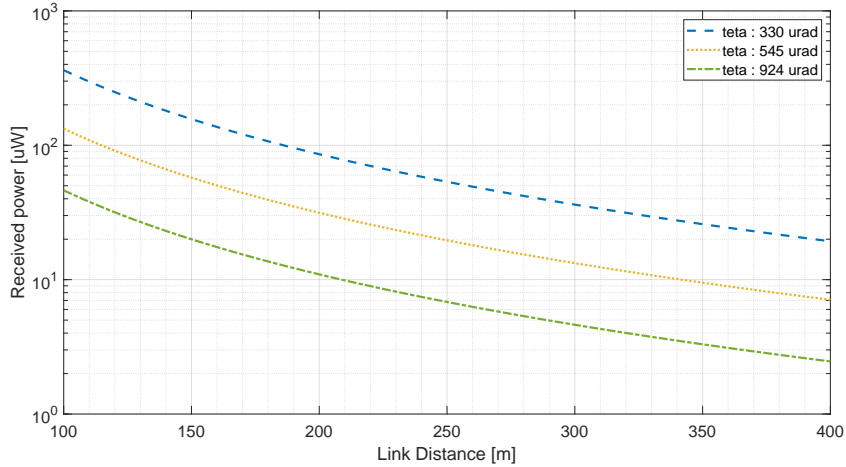


FIGURE 12: Link Budget log scaled

θ_{FWHM}	P_{Rx}	P_{Tx}	G_{TX}	G_{RX}	L_{BW}	L_{FSL}	L_{atm}	L_{sci}
330μrad	-15.87dBm	2dBm	80.08dB	94.23dB	-1.29dB	-189dB	-1dB	-0.83dB
545μrad	-20.23dBm	2dBm	75.72dB	94.23dB	-1.29dB	-189dB	-1dB	-0.83dB
924μrad	-24.81dBm	2dBm	71.14dB	94.23dB	-1.29dB	-189dB	-1dB	-0.83dB

TABLE 5: Estimated optical output power with horizontal link 350m

The estimated optical output power can be obtained through two primary methods. The first approach involves converting the value from dBm to mW using the provided equation, resulting in 25.73μW 9.43μW, and 3.28μW for 330μrad, 545μrad and 924μrad, respectively:

$$mW = 10^{\frac{dBm}{10}} \quad (60)$$

Alternatively, the optical output power can be determined directly by calculating each individual term contributing to the overall power using its corresponding original equation. This approach can be mathematically represented by a comprehensive equation that incorporates all the contributing terms [23]:

$$P_{Rx} = P_{Tx} \cdot \frac{4 \cdot \ln 2}{\pi} \cdot \frac{A_{Rx}}{(L \cdot \theta_{FWHM})^2} \cdot \frac{\beta}{\beta + 1} \quad [W] \quad (61)$$

P_{Tx} transmit optical power [W]

θ_{FWHM} Full-Width-Half-Maximum divergence angle [rad]

A_{Rx} Aperture area of photo detector

Figure 13 presents the estimated received optical power as a function of the optical link distance. The y-axis is labeled in units of microwatts (μW). For clarity, detailed values corresponding to specific link distances of 340 meters, 350 meters, and 360 meters are provided in a separate Table 6.

2.7 LINK BUDGET

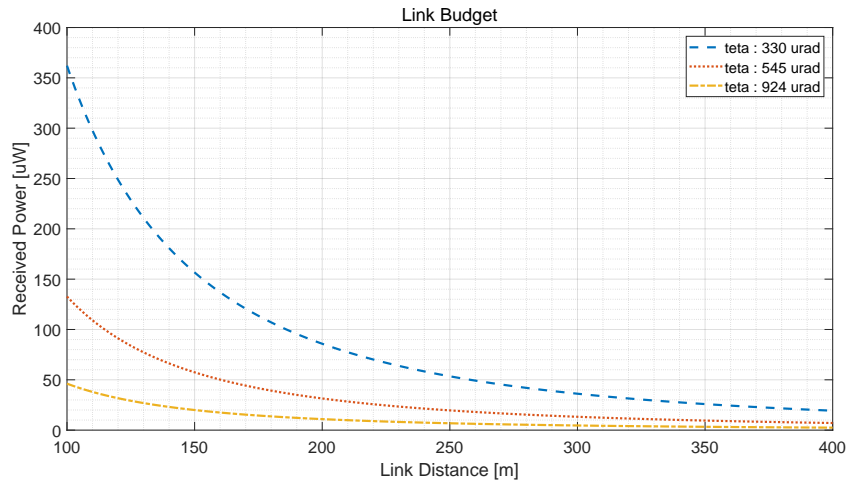


FIGURE 13: Link Budget

Link Distance (L) [m]	340	350	360
$P_{Rx}330\mu \text{ [μW]}$	27.58	25.73	24.35
$P_{Rx}545\mu \text{ [μW]}$	10.11	9.43	8.9
$P_{Rx}924\mu \text{ [μW]}$	3.51	3.28	3.10

TABLE 6: Link Budget

2 THEORY

2.8 POWER VECTOR GENERATION TOOL FOR FREE-SPACE OPTICAL LINKS

This work leverages a MATLAB simulation tool named PVGeT (Power Vector Generation Tool), previously introduced in [52], to model the influence of atmospheric turbulence and pointing jitter on the received optical power. PVGeT offers the capability to generate three distinct categories of received power:

- Power impacted by log-normally distributed atmospheric turbulence effects.
- Power affected by beta-distributed pointing jitter effects.
- A combined scenario encompassing both effects presented as a series of received power values over time.

The tool utilizes parameters such as PSI, signal bandwidth, and mean received power as inputs. These parameters can be determined analytically or obtained from prior experimental measurements. A detailed description of PVGeT's generation and verification process can be found in the aforementioned reference [52].

As illustrated in the PVGeT block diagram (Figure 14) referenced from [52], the simulation generates two independent random variables: one representing log-normal distributed atmospheric scintillation and another representing beta-distributed pointing error. These variables are then multiplied to account for the combined effect of both phenomena. Reference [52] delves into the generation of vectors for these distributions and presents a comparison between the artificially generated data and actual measurement results.

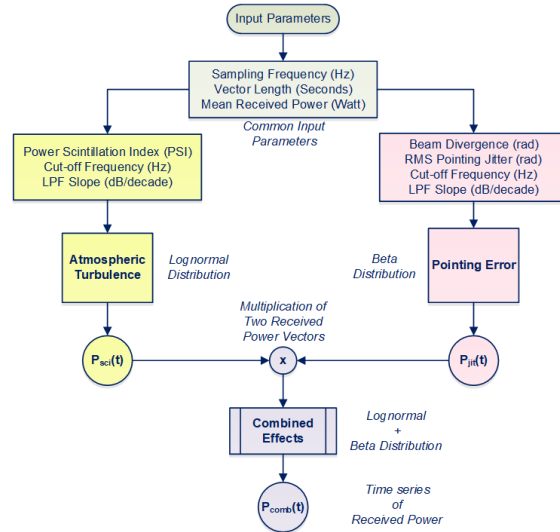


FIGURE 14: PVGeT block diagram [52]

2.8 POWER VECTOR GENERATION TOOL FOR FREE-SPACE OPTICAL LINKS

Previous research has primarily utilized PVGeT vectors for simulating LEO (Low-Earth Orbit) satellite downlink and uplink scenarios [53], [52], [54]. However, PVGeT can also be employed for horizontal link simulations by adjusting the input parameters. Reference datasets of power vectors, generated by DLR [53], can be used to verify different systems across various uplink elevation angles [54]. This work focuses on determining the input parameters necessary to utilize PVGeT for generating power vectors representing a horizontal link with a double-transmitter setup. The objective is to simulate and evaluate the advantages of transmitter diversity in mitigating scintillation effects.

Our approach involves generating normalized mean power log-normal distribution vectors using PVGeT, with a length of 10 seconds for each transmitter. The generated vectors are then summed to obtain the combined received power vector for the double-transmitter setup. Table 7 details the specific input variables used in this process.

Parameters	Values
Sampling Frequency	10kHz
Vector Length	10s
Scintillation Index	0.02
Cut-Off Frequency	120 dB/decade
LPF slope	20Hz
Mean Power	1W

TABLE 7: PVGeT tool input parameters and assigned values

Figure 15 (a) exemplifies a power vector generated with PVGeT, while Figure 15 (b) depicts its corresponding probability density function (PDF). The normalized power vector has a mean power of 1, and its PDF exhibits a log-normal distribution, which aligns with the theoretical log-normal distribution also shown in the graph.

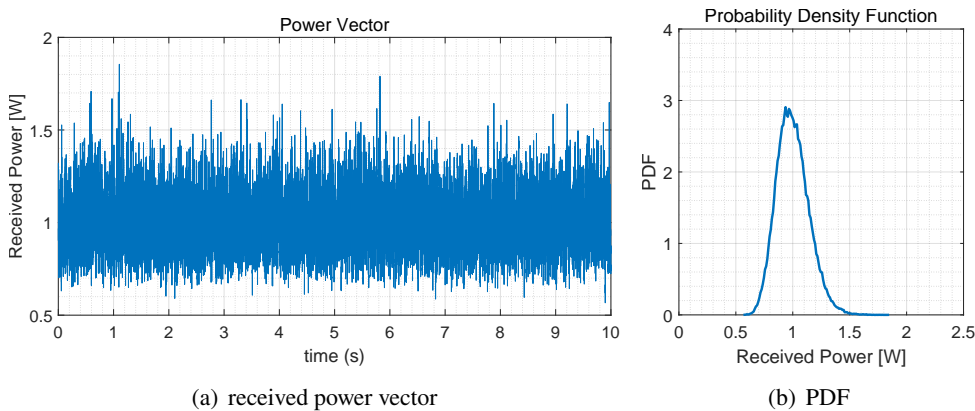


FIGURE 15: Example Power Vector generated by PVGeT tool and PDF of the power vector

2 THEORY

In this study, we employed the PVGeT tool to generate two unique power vectors. To explore scenarios involving double transmitters, the sum of these two vectors was then computed. These combined power vectors served as the foundation for simulating transmitter diversity in next section.

2.9 SPATIAL DIVERSITY

In FSO communication, researchers have explored various techniques to combat the detrimental effects of atmospheric turbulence on optical signals. One promising technique is spatial diversity, employing multiple beams. The concept of spatial diversity, initially introduced for wireless communication systems, this technique utilizes various configurations, including SIMO (single input multiple output), which has single transmit antenna and multiple receive antennas, MISO (multiple input single output), which has multiple transmit antennas and single receive antenna, and MIMO (multiple input multiple output), which has multiple transmit antennas and multiple receive antennas [5].

This technique has been adapted for FSO applications [55] in various scenarios by utilizing multiple transmit apertures (transmit diversity) or the receive apertures (receiver diversity) or at both sides (multiple input multiple output– MIMO) [13]. These configurations are illustrated in Figure 16, Figure 17, and Figure 18, respectively.

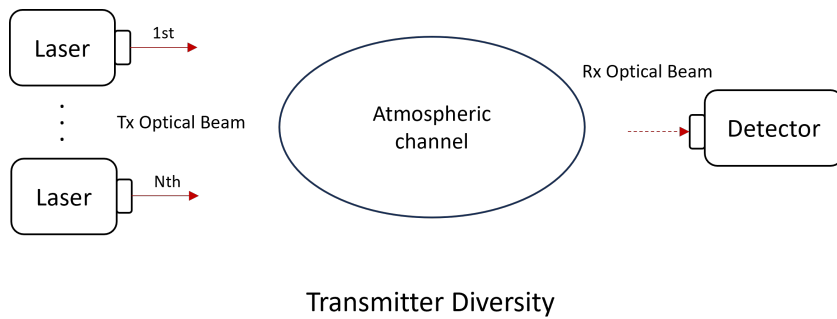


FIGURE 16: Transmitter diversity (MISO)

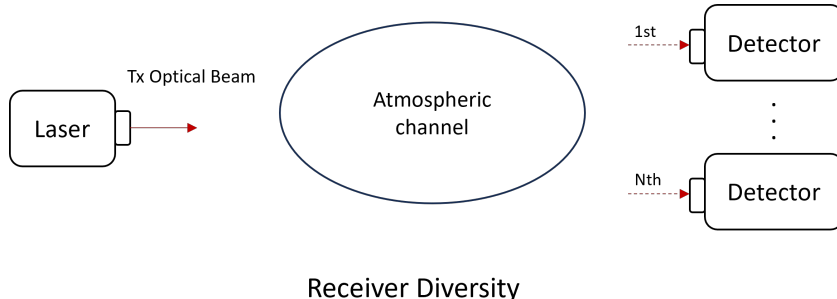


FIGURE 17: Receiver diversity (SIMO)

2 THEORY

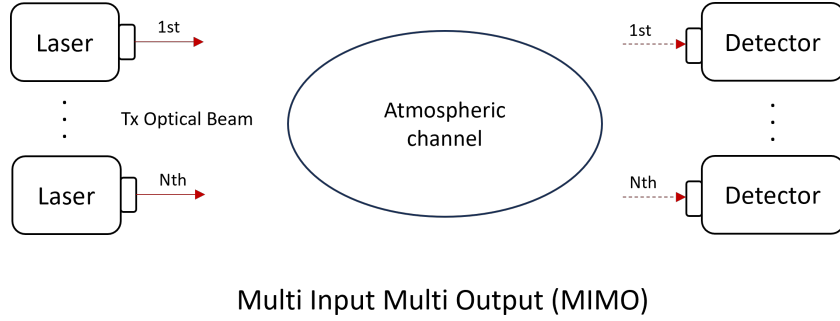


FIGURE 18: Transmitter and receiver diversity (MIMO)

Building upon prior research [56] demonstrating the advantages of spatial diversity for FSO communication, this study investigates its impact on signal strength and system performance. Spatial diversity, by employing multiple beams, offers several benefits in mitigating atmospheric turbulence. It allows for enhanced signal strength. This translates to increased transmission distances, higher achievable data rates, and robust operation even under heavy attenuation conditions. The inherent redundancy provided by spatial diversity reduces the probability of experiencing both deep fades (significant signal weakening) and surges (sudden intensity increases). Consequently, lower transmitter power levels can be employed while maintaining safe laser operation within wavelength-dependent thresholds.

Prior research [11] investigated the Bit Error Rate (BER) performance of FSO links utilizing spatial diversity over log-normal atmospheric turbulence channels. Their study demonstrated, through numerical results, the effectiveness of spatial diversity in reducing channel variance. However, the observed performance degradation due to spatial correlation highlights the criticality of maintaining efficient separation between apertures and strict co-alignment to achieve the full potential diversity gain offered by employing multiple transmitters and receivers.

Furthermore, the effectiveness of spatial diversity in Multiple-Input Multiple-Output (MIMO) FSO systems has been extensively validated across various regimes, distributions, and applications. Research employing diverse modulation formats provides strong evidence for its advantages. Studies utilizing both multi-pulse Pulse-Position Modulation (PPM) [57] and Q-ary PPM [58] have demonstrated its efficacy in mitigating fading effects under different channel conditions, including both log-normal and Rayleigh fading regimes. Additionally, research has explored the benefits of spatial diversity in Intensity Modulation/Direct Detection (IM/DD) systems with On-Off Keying (OOK) modulation through K turbulence channels [59]. This comprehensive body of research underscores the versatility and robustness of spatial diversity in enhancing the performance of FSO links.

2.9.1 SUM OF RANDOM VARIABLE

In free-space optical communication systems that employ multiple beams transmitted from separate sources, we often analyze the combined effect of atmospheric effects on the signal. This combined effect can be represented mathematically as the sum of several random variables, denoted as :

$$Y = X_1 + X_2 + X_3 + \dots + X_n \quad (62)$$

where each X_i represents the random influence of atmospheric conditions on an individual beam.

There's a property called the linearity of expectation [60], which states that the expected value (our case, average received optical power) of a sum equals the sum of the expected values of each individual variable. This means the total mean received power value from multiple beams is simply the sum of the individual mean received power value of each beam.

$$E(Y) = E(X_1) + E(X_2) + E(X_3) + \dots + E(X_n) \quad (63)$$

The general formula for the variance of the sum of variables [60] in free-space optical communication with multi-beam sources :

$$\text{Var}\left(\sum_{i=1}^n X_i\right) = \sum_{i=1}^n \text{Var}(X_i) + 2 \sum_{i < j} \text{Cov}(X_i, X_j) \quad (64)$$

The variance of the sum of two random variables can be expressed as :

$$\text{Var}(X_1 + X_2) = \text{Var}(X_1) + \text{Var}(X_2) + 2\text{Cov}(X_1, X_2) \quad (65)$$

Covariance, denoted as $\text{Cov}(X_1, X_2)$, measures the tendency of the influence on two beams (X_1 and X_2) to vary together. A positive covariance suggests they're affected by similar atmospheric conditions, while negative covariance indicates they might experience opposite effects.

$$\text{Cov}(X_1 + X_2) = E(X_1 X_2) - E(X_1)E(X_2) \quad (66)$$

Many of these properties and relationships can be directly proven using this definition. For instance, if the atmospheric effects on different beams are independent, then $E(X_1 X_2) = E(X_1)E(X_2)$, and therefore $\text{Cov}(X_1, X_2) = 0$. If the atmospheric effects on $X_1, X_2, X_3, \dots, X_n$ are all independent, the formula simplifies to

2 THEORY

$$Var\left(\sum_{i=1}^n X_i\right) = \sum_{i=1}^n Var(X_i) \quad (67)$$

This means the variance of the received signal is simply the sum of the individual variances of the atmospheric effects on each beam, because the covariances between independent effects are zero.

2.9.2 MEAN POWER AND PSI WITH N TRANSMITTERS

Leveraging the previously established concept of sums of random variables, this work aims to derive general expressions for both the average received power and the power scintillation index (PSI) within free-space optical communication systems, utilizing multiple beams [61].

Assuming a scenario with N independent optical beams, the separation between the transmitter or receiver apertures exceeds the atmospheric coherence width (r_0), introduced in Section 2.4. This ensures that the N beams are statistically independent and uncorrelated. In this case, the combined received signal can be expressed as :

$$P_N = \sum_{j=1}^N P_j \quad (68)$$

To simplify the analysis, we make an assumption that the means and variances of all the beams are identical. Under this assumption, the total mean received power, $\langle P_r \rangle$, can be derived using Equation (63) [10]:

$$\langle P_N \rangle = N \times \langle P_j \rangle \quad (69)$$

The introduction of multiple, uncorrelated signal paths through spatial diversity modifies the received power. This modification can be expressed as the summation of individual powers from each path, as shown in Equation (69). This equation demonstrates a proportional relationship between the mean received power and the number of identical beams (N). The inherent summation characteristic of spatial diversity leads to an increase in the average received power.

The variance of the received power in multi-beam systems were further investigated. We begin by expressing the variance of N beams, denoted by $Var(X_N)$ and the variance of a single beam as $Var(X_j)$. Employing Equation (39), the variance of N beams $Var(X_N)$ can be expressed as :

$$Var(X_N) = \langle P_N \rangle^2 \times \sigma_N^2 \quad (70)$$

Also, the variance of single beam $Var(X_j)$ can be expressed as :

$$Var(X_j) = \langle P_j \rangle^2 \times \sigma_j^2 \quad (71)$$

By leveraging the relationship between multi-beam average power and single-beam power established in Equation (69), we can simplify Equation (70) to Equation (72).

$$\text{Var}(X_N) = N^2 \times \langle P_j \rangle^2 \times \sigma_N^2 \quad (72)$$

Furthermore, the fundamental property of variances for independent beams, Equation (67), allows us to express the variance of N beams $\text{Var}(X_N)$ as the sum of the variances of individual beams $\text{Var}(X_j)$.

$$\text{Var}(X_N) = N \times \text{Var}(X_j) \quad (73)$$

Combining Equations (71), (72), and (73), we arrive at a key result: Equation (74). This equation relates the PSI of N beams, σ_N^2 , to the PSI of a single beam, σ_j^2

$$N^2 \times \langle P_j \rangle^2 \times \sigma_N^2 = N \times \langle P_j \rangle^2 \times \sigma_j^2 \quad (74)$$

Finally, by simplifying Equation (74), we obtain an Equation (75), which reveals that the PSI of N beams is inversely proportional to the number of beams (N). In other words, as the number of beams in a system increases, the overall scintillation strength, represented by PSI, for the combined power decreases.

$$\sigma_N^2 = \frac{1}{N} \times \sigma_j^2 \quad (75)$$

Conversely, when the N received signals exhibit correlation, the resulting correlated power scintillation index, denoted by σ_N^2 is influenced by the degree of correlation, as described in Equation (76) [62]. This equation introduces the concept of the spatial correlation coefficient (r_p), where P represents the set of all possible beam pairs and p refers to an individual pair. In the absence of any correlation between beams ($r_p = 0$), Equation(76) simplifies to the previously derived Equation(75).

$$\sigma_N^2 = \frac{1}{N} \left(1 + \frac{2}{N} \sum_{p \in P} r_p \right) \sigma_j^2 \quad (76)$$

The fluctuation of the received power, quantified by Equation (75) , exhibits an inverse relationship with the number of identical beams (N). This translates to a reduction in the overall power scintillation index (PSI). As the number of incorporated optical beams increases, the overall signal becomes less susceptible to variations induced by atmospheric effects on individual beams. However, according to Equation(76), this effect is only possible when there is no correlation in any beam pairs. Normally this conditions can be satisfied when the beams separation distances are larger than the atmospheric coherence width (r_0). Numerical researches have been done in [63] and [62] and detailed in section 2.10

2 THEORY

The key takeaway from Equation (75) is the inverse relationship between the fluctuation of received power, quantified by the PSI and the number of identical beams (N). This translates to a reduction in the overall power scintillation index. As the number of incorporated optical beams increases, the combined signal becomes less susceptible to power variations caused by atmospheric effects on individual beams. However, as highlighted by Equation (76), this beneficial effect is only achievable when there is no correlation between any beam pairs. Typically, this condition can be met when the separation distances between beams are larger than the atmospheric coherence width, denoted by r_0 . For a more detailed discussion on achieving decorrelation through beam separation, refer to Section 2.10. Existing research on this topic can be found in [63] and [62].

This section has established the efficacy of spatial diversity as a method to improve the performance of FSO links. The discussion encompassed both previous research findings and the underlying mathematical theory. Building upon this foundation, the subsequent section will delve deeper into the specific advantages offered by transmitter diversity, particularly focusing on configurations employing two transmitters ($N=2$). This analysis will leverage a combined approach, utilizing both mathematical derivations and numerical simulations to comprehensively evaluate the impact of two-transmitter diversity on FSO links.

2.10 TRANSMITTER DIVERSITY

2.10.1 TRANSMITTERS SEPARATION

Building upon the established benefits of spatial diversity, as discussed in Section 2.9, this section delves deeper into the performance of transmitter diversity specifically. In previous research [63], the optimal number and spacing of transmitters required for effective mitigation of atmospheric scintillation-induced received power fluctuations were investigated. This study explored transmitter diversity configurations with varying numbers of transmitters ($N = 1$ to 16) in both weak and strong fluctuation regimes, utilizing link distances of 1.2 km and 10.4 km.

The research observed a proportional reduction in signal fluctuations as the number of laser transmitters (N) increased. Interestingly, as the number of lasers increased and fluctuations decreased, the log-normal model provided a better fit with slight shift in the distribution. Notably, when the separation distance between transmitters (d) exceeded the atmospheric coherence width (r_0), there was no significant difference in performance between various separation configurations. This effect was particularly pronounced for shorter optical links compared to longer ones. These findings suggest that the condition, separation distances greater than the atmospheric coherence length ($d > r_0$), should be satisfied for reducing received power fluctuations to acceptable levels.

Building upon the concept of transmitter diversity, additional research [62] explored the channel correlation characteristics in a terrestrial free-space optical communication link employing multiple laser transmitters ($N=1,4$). This study utilized numerical simulations to demonstrate that the channel correlation increases with both the receiver aperture size and the propagation distance. A simple scaling rule for the spatial correlation coefficient(r_p) and scintillation index (σ_N^2) in a system with N spatially correlated received signals were introduced in Equation(76).

2.10.2 DOUBLE TRANSMITTER

This section delves specifically into the performance of a double transmitter configuration ($N=2$). This configuration presents potential advantages, including doubling of signal strength and half reduced susceptibility to atmospheric turbulence. Previous research [51] demonstrated the performance improvements with a double transmitter configuration in ground-to-ground direct-detection transmission over 61 km optical link under strong atmospheric turbulence. This study employed two identical transmitters operating at 1 W and 980 nm, separated by approximately 4 meters, exhibited correlation with the high optical attenuation caused by near-ground fog and mist in front of the receiver. The doubling of the mean received power with double transmitter was observed, led to a significant reduction in signal fading, with the probability of a 3 dB fade from the mean power. A range of 15 to 33 percents fades probability was observed with double transmitter compared to 26 to 46 percents for single transmitter.

In our experiment, we implemented a double-transmitter setup utilizing identical 1.6 mW continuous wave gaussian beams with a wavelength of 1550 nm at each transmitter. Importantly, our experiments employed three different full width half maximum (FWHM) divergence angle

2 THEORY

guassian beams: $330 \mu\text{rad}$, $545 \mu\text{rad}$, and $924 \mu\text{rad}$. Based on the principles of transmitter diversity, we anticipated achieving double the average received optical power and a reduction in PSI values by half compared to a single-transmitter setup. To minimize the impact of signal correlation between the two transmitters, Chapter 4 explores the separation distance. Building upon these findings, Chapter 5 will delve into the performance of the double transmitter configuration under various beam divergence angles.

To illustrate the theoretical predictions derived in Equations (69),(75), a specific scenario involving a double transmitter configuration ($N=2$) was investigated. In this scenario, both transmitters were assumed to possess similar mean received power and comparable PSI values. The previously derived equations for average received power and PSI were then particularized to this specific double transmitter case.

$$P_s = 2 \times P_1 \quad [\text{W}] \quad , \quad \sigma_s^2 = \frac{\sigma_1^2}{2} \quad (77)$$

Where P_s is total received power and σ_s^2 is total PSI value with two transmitters

Where P_1 is received power and σ_1^2 is PSI value with one transmitter

2.10.3 SIMULATIONS

To validate these theoretical summaries, the PVGeT tool introduced earlier was employed (See section 2.8). Two independent optical power vectors were generated using the same input parameters (Table 7), representing the received power vectors for TX1 and TX2. The sum of these vectors was considered to represent the double transmitter setup (TXs). Figure 19 visually depicts the power vectors for TX1, TX2, and the combined TXs.

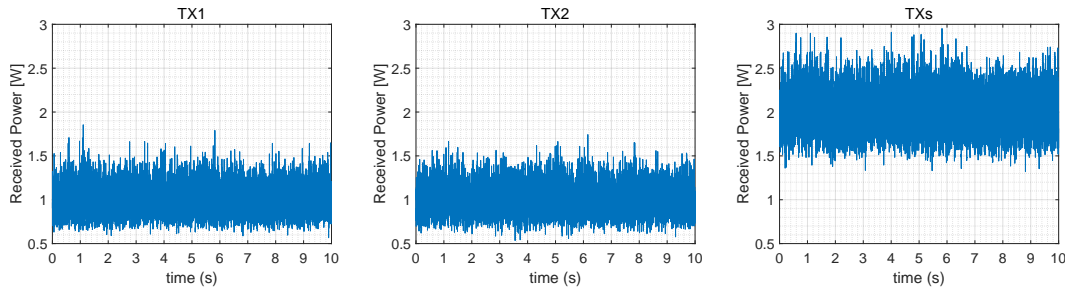


FIGURE 19: Power vectors generated with PVGeT for TX1, TX2 and TXs

Furthermore, Figure 20 presents the probability density functions (PDFs) for each power vector, plotted on a single graph for comparison. Additionally, the theoretical log-normal distribution for the random variable power vectors was investigated. Equation (49) was employed to derive the log-normal distribution for TX1: $\ln(X) \sim \mathcal{N}(\mu, \sigma^2)$, where X represents the power vector and $\mathcal{N}(\mu, \sigma^2)$ denotes a normal distribution with mean power μ and power scintillation index

(PSI) σ_p^2 . It is important to note that the input mean power was set to 1 (normalized mean power), and we consider the variance σ^2 to be equivalent to the PSI (σ_p^2). Similarly, the log-normal distribution for the double-transmitter setup (TXs) was derived as $\ln(2X) \sim \mathcal{N}(2\mu, \sigma^2/2)$ with double mean power and half PSI value by utilizing the Equation (77). These distributions are also plotted in Figure 20 for visual comparison.

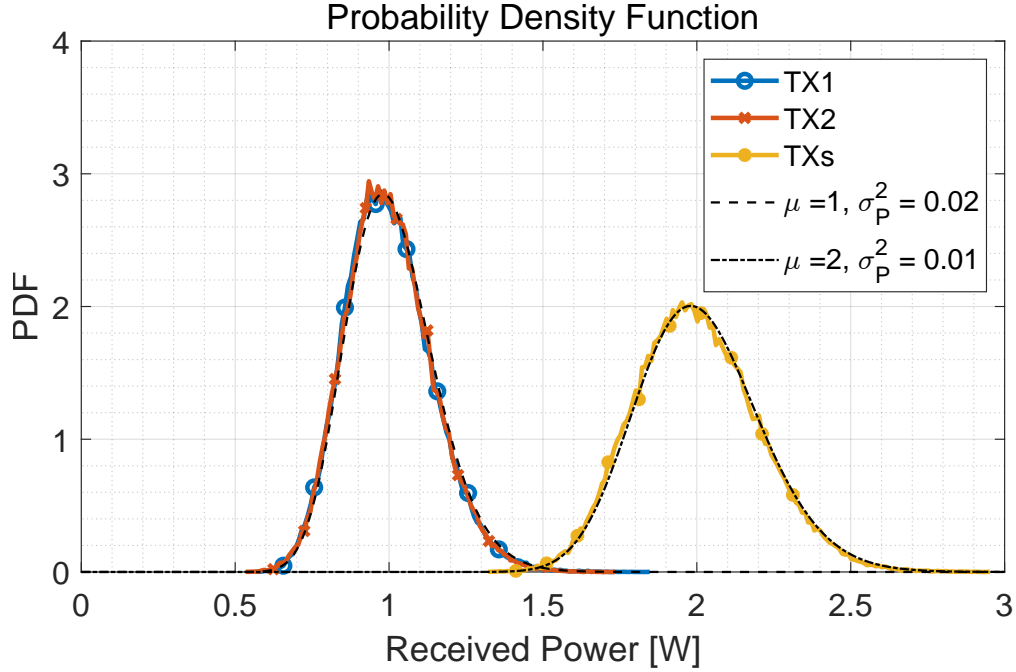


FIGURE 20: Probability Density Function for TX1, TX2 and TXs

An examination of the probability density functions (PDFs) for the received power vectors of TX1 and TX2 revealed a high degree of similarity. Both PDFs exhibited a log-normal distribution, a characteristic distribution for received power in free-space optical communication systems. Notably, both PDFs shared an identical mean value of 1 Watt, indicating a consistent average received power for both individual transmitters. However, a closer look revealed subtle differences in the spread of the distributions. The power scintillation index (PSI) values for TX1 and TX2 were found to be 0.02 and 0.0198, respectively. While this difference is minimal, it suggests a slightly higher variability in the received power for TX1 compared to TX2. The PDF of the combined TXs vector, representing the double transmitter configuration, also displayed a log-normal distribution as expected. The mean value of this combined PDF doubled to 2 Watts, confirming the theoretical prediction that the average received power effectively doubles with the double transmitter setup. The analysis of the standard deviation for the TXs vector yielded an interesting observation. As anticipated, the PSI decreased to 0.01 compared to the individual transmitters, representing roughly a half reduction effect. This finding aligns well with the established theory, suggesting that while the average power is amplified, the overall distribution of the received power exhibits a lower degree of deviation in the double transmitter setup compared to the single transmitters.

2 THEORY

Figure 21 shows the power density function (PDF) of the power vectors generated by PVGeT tool. The figure (a) describes one transmitter with its fade threshold -1.5dB from its mean power and figure (b) describes two transmitters with its fade threshold. As we predicted in the theory part 2.5, one-transmitter configuration, which has double power scintillation index (PSI), shows more probability of fades events compared to two-transmitter configuration. For the two-transmitter, which has half PSI value, at the figure (b), shows almost zero fades. It confirms the theory section 2.5 that higher PSI values cause more fades events and lower PSI values causes less fades. Additionally, in weak turbulence regime ($\sigma_p^2 < 1$), there is potential possibility to achieve zero fades event by utilizing transmitter diversity.

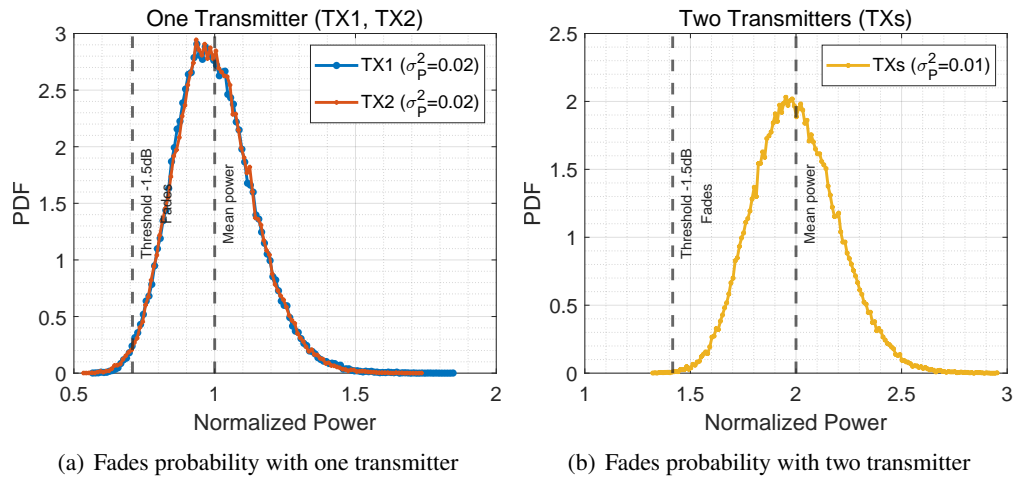


FIGURE 21: Fades probability with -1.5dB threshold

The observations presented in Figure 21 highlight the potential of transmitter diversity to achieve near-zero fade events, especially within a weak turbulence regime characterized by a low scintillation index ($\sigma_p^2 < 1$). This finding suggests that employing a double-transmitter configuration can significantly mitigate scintillation effects and potentially lead to highly reliable signal transmission under specific atmospheric conditions.

While the current analysis provides valuable insights, further investigation is warranted to fully explore the relationship between PSI values, fade events, and different atmospheric conditions. By incorporating the measurement data in section 2.5, a more comprehensive understanding of how transmitter diversity influences fade events under diverse atmospheric scenarios could be achieved.

Figure 22 presents the PSI values for each vector. PSI was evaluated for every second (Table 8), and the overall PSI value for the entire 10-second duration is displayed in the top right corner of the graph. The 10-second PSI values for TX1, TX2, and TXs were found to be 0.02, 0.0198, and 0.01, respectively. This demonstrates that the PSI value for TXs was approximately halved compared to the single transmitter setups.

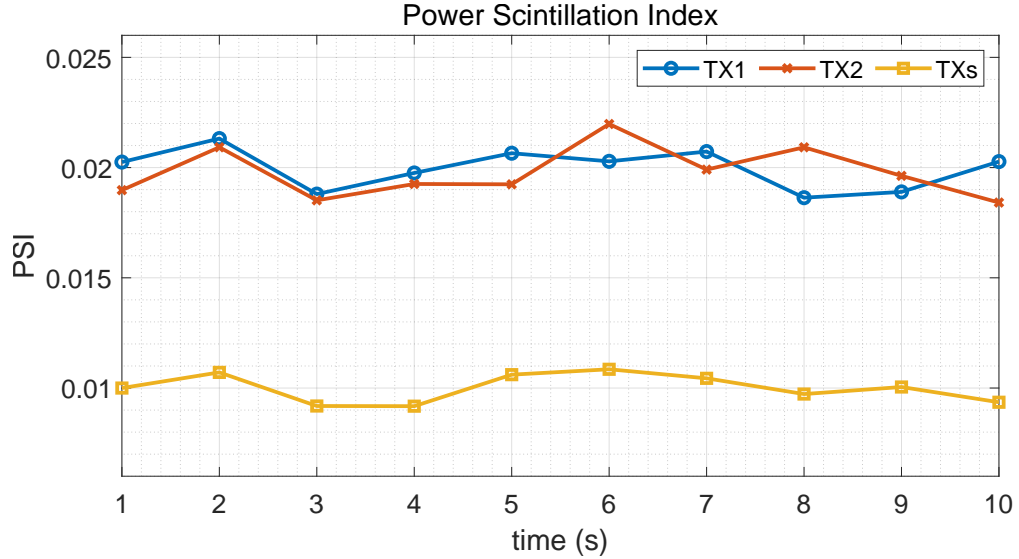


FIGURE 22: Power Scintillation Index for TX1, TX2 and TXs

second	1	2	3	4	5	6	7	8	9	10
TX1	20.3	21.3	18.8	19.8	20.7	20.3	20.7	18.6	18.9	20.3
TX2	19.0	20.9	18.5	19.3	19.2	22.0	19.9	20.9	19.6	18.4
TXs	10.0	10.7	9.2	9.2	10.6	10.9	10.4	9.7	10.0	9.4

TABLE 8: PSI values for each second $\times 10^{-3}$

Figure 23 presents the analysis of signal fades experienced in the simulation. The threshold for identifying a fade event was established at -1.5 dB relative to the mean received power value. This threshold translates to approximately $0.708 \times$ the mean power. The results of the fade analysis exhibited a strong correlation with the trends observed in the PSI graph (Figure 22). As evident from the graph, employing a double transmitter configuration with a low PSI value of 0.02 for each individual transmitter significantly reduced the occurrence of fades. In fact, the fade analysis suggests that near-zero fades were experienced in this scenario.

2 THEORY

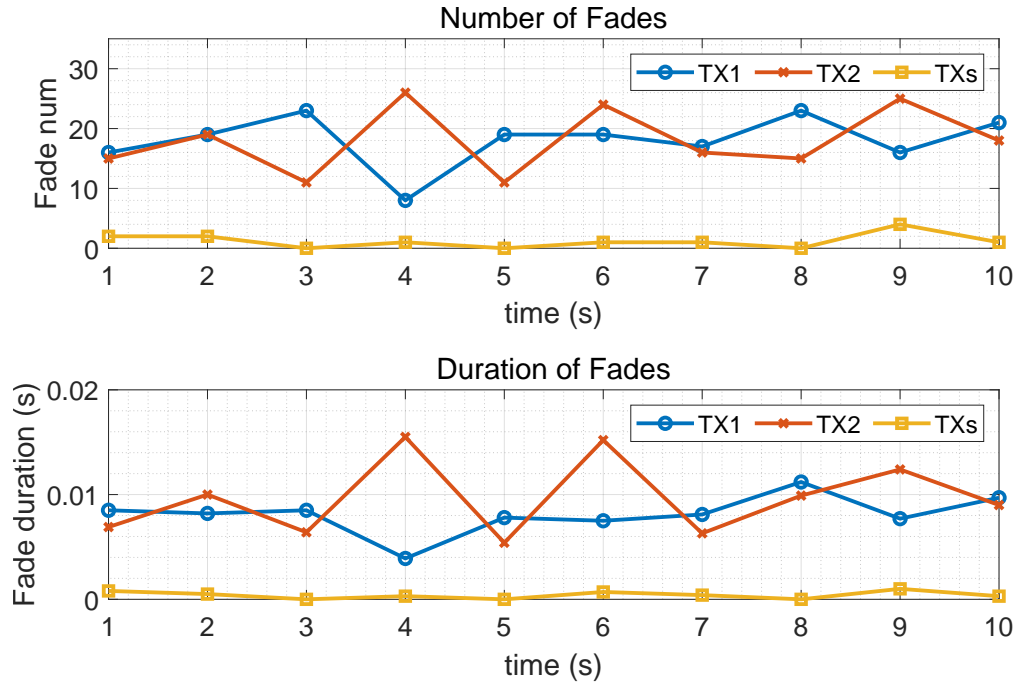


FIGURE 23: Fades Analysis for TX1, TX2 and TXs

These numerical and analytical findings provide valuable insights into the advantages of employing a double transmitter configuration. These results will be further compared with the experimental measurements presented in the Analysis chapter 5.

HARDWARE

3 HARDWARE

3.1 TRANSMITTER

This section details the configuration and positioning of the two identical transmitters employed in the measurements. Information of the overall link configuration were provided in Figure 1 and Table 1. The transmitters were positioned on the fourth floor of the German Space Operations Centre (GSOC) building, located within the German Aerospace Center (DLR) campus in Oberpfaffenhofen, Munich. The GSOC building itself has an approximate altitude of 580 meters above sea level.

As illustrated in Figure 24, these transmitters were positioned with a separation distance exceeding 2.7 meters. This separation distance was chosen to be larger than the atmospheric coherence length, also known as the Fried parameter, which was discussed in Section 2.4. This strategic placement ensures the independence of the beams emitted by each transmitter, maximizing the potential benefits of the double-transmitter configuration.

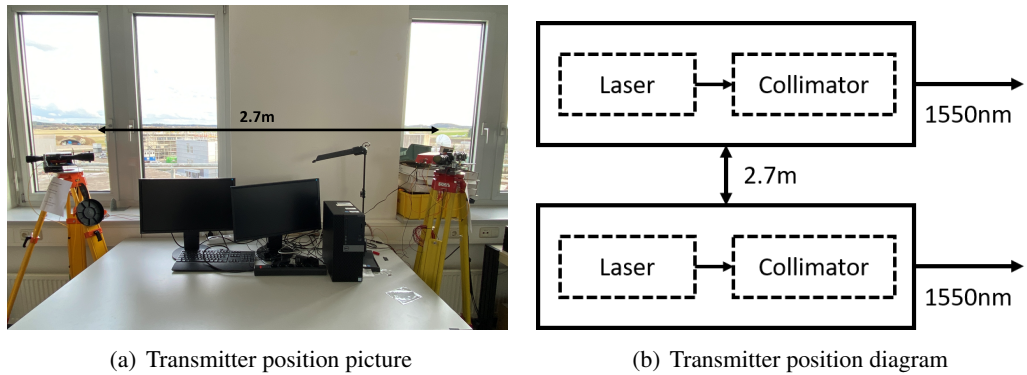


FIGURE 24: Transmitters set-up

The employed transmitters were meticulously assembled on lightweight aluminum plates. Each transmitter consisted of a continuous-wave (CW) 1550 nm single-mode InGaAsP laser source, emitting approximately 1.6 mW of power. To collimate the laser beam, a collimator with an anti-reflective coated aspheric lens optimized for the 1050-1620 nm wavelength range was incorporated. A single-mode fiber optic cable connected the laser source to the collimator. Additionally, a scope was integrated to precisely guide and direct the beam towards the receiver, facilitating optimal alignment between the transmitter and receiver terminals. A key feature of the transmitter design was the inclusion of a motorized laser shutter positioned in front of the collimator. This shutter operated cyclically, enabling signal transmission for 10 seconds out of every 11-second interval. During the remaining 1 second, the shutter blocked the signal to allow for background light measurement. An Arduino Uno board working in conjunction with motors and cardboard components controlled this cyclical operation. A visual representation of the complete transmitter assembly is provided in Figure 25.

Table 9 provides a detailed breakdown of the characteristics associated with the collimators (A, B, and C) utilized in the measurements. This table includes the parameter values of Gaussian

3.1 TRANSMITTER

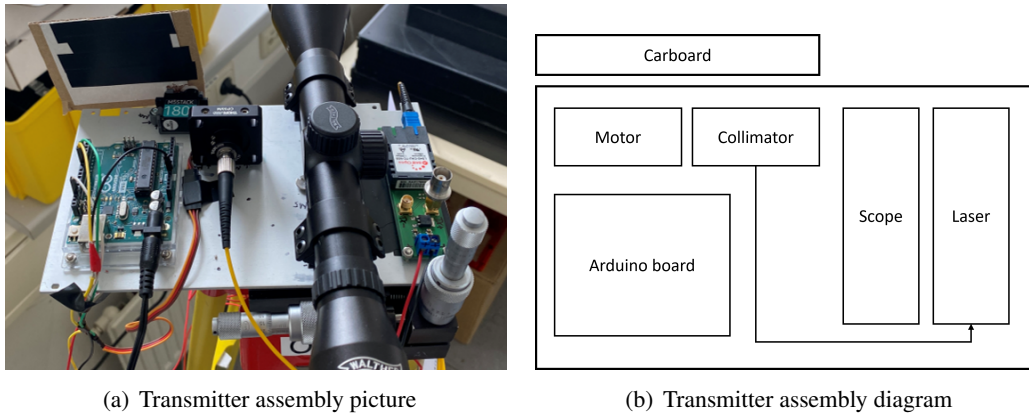


FIGURE 25: Transmitters set-up

Collimator	Collimator A	Collimator B	Collimator C
Full range angle $2\omega_0$	$559\mu\text{rad}$	$925\mu\text{rad}$	$1570\mu\text{rad}$
FWHM divergence angle θ_{FWHM}	$330\mu\text{rad}$	$545\mu\text{rad}$	$924\mu\text{rad}$
Beam diameter at $\frac{1}{e^2}$	3.6mm	2.1mm	1.21mm

TABLE 9: Collimator Characteristics

beam properties (waist radius, ω_0 , and divergence angle, θ_{FWHM}) introduced in Section 2.1. The following section will delve into the specifics of the receiver employed in the experiment.

3 HARDWARE

3.2 RECEIVER

This section focuses on the specifics of the optical receiver employed in the experiment. The receiver was strategically positioned on the third floor of the Institute for Communication and Navigation (KN) building, located within the DLR campus. During the design process, meticulous attention was placed on minimizing weight and dimensions, while also considering the availability of an external power source. This emphasis on portability and power autonomy ensured the receiver's independent functionality and its adaptability across diverse environments.

As illustrated in Figures 26, the optical receiver was designed structure comprised of three distinct levels of acrylic plates. The first level housed critical optical components, including a photodetector, a focal lens, an optical band-pass filter, and a lens tube. The second level accommodated the data-logger responsible for recording measurements, while the third level housed the power supply consisting of batteries. This modular design with separate levels for components facilitated easier maintenance and provided a clear overview of the internal structure. The Figure 27 depicts the detail of the receiver with pictures of front and side of the receiver.

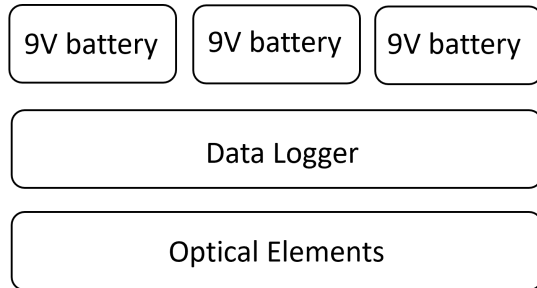
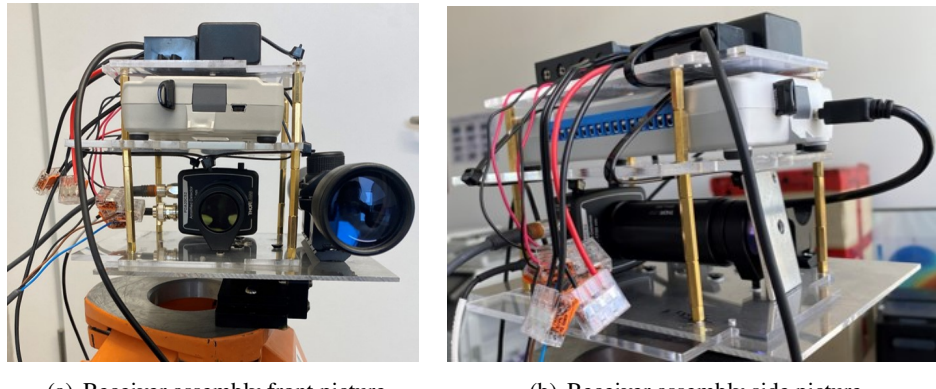


FIGURE 26: Receiver assembly diagram



(a) Receiver assembly front picture

(b) Receiver assembly side picture

FIGURE 27: Receiver assembly picture

The optical components housed in the first level included a gain-adjustable InGaAsP photodetector

with peak responsivity at 1550 nm, a 1550 nm optical band-pass filter ensured only light within the designated wavelength range reached the detector, and a 30 mm lens tube housed a spherical lens (25.4 mm diameter and 40 mm focal length) that focused the received signal onto the photodetector, as illustrated in the Figure 28. The BPF and PD denote band-pass filter and photodetector, respectively. Specific gain settings for the photodetector are detailed in Table 10. Equation(78) allows to calculate the received optical power (P_{out}) based on the measured electrical signal strength from the photodetector. This equation expresses the relationship between the output optical power, the converted output voltage (V_{out}), and the responsivity (R) of the photodetector at the specific wavelength of 1550 nm. The responsivity value employed in this calculation is $R = 1.04[A/W]$.

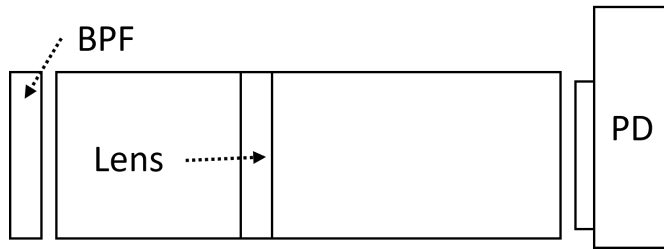


FIGURE 28: Receiver optical components assembly diagram

Gain	0dB	10dB	20dB	30dB
value [V/A]	$1.51 \cdot 10^3$	$4.75 \cdot 10^3$	$1.5 \cdot 10^4$	$4.75 \cdot 10^4$
Gain	40dB	50dB	60dB	70dB
value [V/A]	$1.51 \cdot 10^5$	$4.75 \cdot 10^5$	$1.5 \cdot 10^6$	$4.75 \cdot 10^6$

TABLE 10: Photodetector gain property

$$P_{out} = V_{out} \times \frac{1}{R \times gain} [W] \quad (78)$$

The best form spherical lens is designed with two different radii of curvature for each side to achieve optimal performance (diffraction-limited performance) for small input beam diameters. The optical band-pass filter, centered at 1550nm with a bandwidth of 12nm, were placed in front of the lens tube. The received light was subsequently focused by the spherical lens onto a photo-detector with a 2mm diameter active region, granting the receiver a field of view of 0.05 rad.

Positioned on the second level, a low-weight data logger integrated with the system. The power supplies, placed on the third level, harnessed the energy of 9V alkaline batteries, enabling stand-alone operation. Prior to deployment, a assessment was conducted in an indoor environment,

3 HARDWARE

utilizing a voltage source to validate the proper operation of both the photo-detector and the data logger.

The performance of the photo-detector was evaluated while connected to the data logger. Three different configurations were tested:

- a voltage input of $\pm 6V$ with a current range of 15-24mA
- a voltage input of $\pm 9V$ with a current range of 15-30mA
- a voltage input of $\pm 12V$ with a current range of 20-34mA.

The output voltages of the photodetector increased in accordance with these settings. Using the maximum gain setting of 70dB, the outputs were measured as 5V, 8V, and 10V respectively. Based on these results, it was determined that a differential power supply consisting of two alkaline 9V batteries with a capacity of 475mAh would be suitable. This power supply can sustain a current of approximately 20mA for a duration of 20 hours.

The performance of the data logger was assessed same approach while being connected to the photodetector. To prevent over loaded voltage, 5V DC/DC converter was added in between the power supplier and the data logger. The instrument displayed a red LED indicator, indicating an error status, when a voltage input of 4.5V were used. However, when the voltage input was increased to 5V, the instrument was able to operate in stand-alone recording mode, albeit occasionally indicating an error. Subsequently, a decision was made to supply an input voltage of 9V, which allowed for error-free operation of the data logger.

The final receiver design prioritizes achieving a low weight and portable size. Targeting a compact form factor, the dimensions were established as 160mm x 100mm x 100mm, with a targeted weight of 750g. This includes all major functional components as well as ancillary elements like fasteners. A comprehensive hardware configuration diagram is provided in Figure 29 to serve as a visual summary of the discussed design.

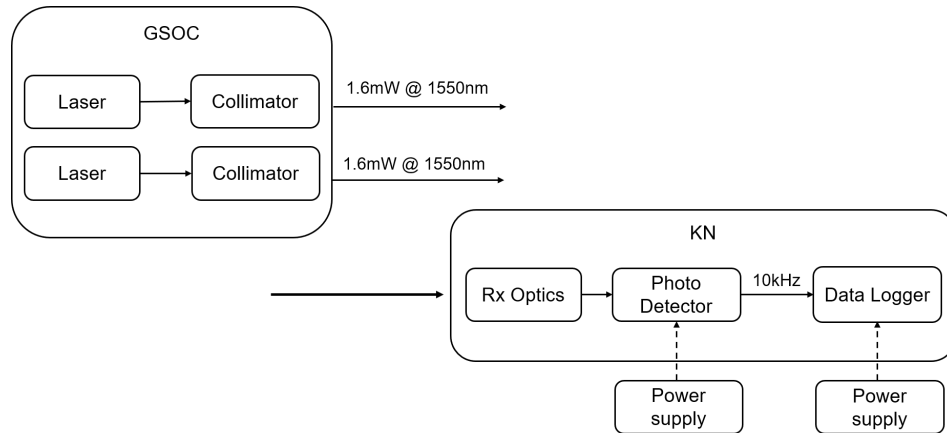


FIGURE 29: Hardware set-up

MEASUREMENT

4 MEASUREMENT

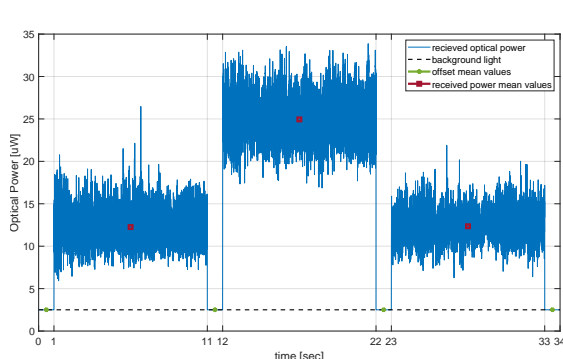
The experiments were conducted across an expansive area spanning approximately 350 meters on the DLR campus in Wessling, as visually illustrated in the provided image1. The transmitters and receiver were strategically positioned at the GSOC building and KN building respectively, both situated at an elevation of around 580 meters above sea level. The path's altitude above sea level was utilized to determine the refractive index structure parameter (C_n^2) profiles, employing the Hufnagel-Valley model as a reference [15], introduced in Section 2.3. The comprehensive data acquisition campaigns were undertaken during an extensive period, commencing from the 14th of March and spanning until the 16th of April. Each individual measurement was conducted at various time frames and subjected to diverse weather conditions. The date, time and weather parameters were documented alongside the measurement data in a tabular format.

In the previous chapter, the hardware setup for the experiment was discussed. To reiterate, two identical transmitters were positioned approximately 2.7 meters apart, each equipped with identical collimators. A single receiver was employed alongside these transmitters. Three distinct FWHM divergence angles were utilized: $330\mu\text{rad}$, $545\mu\text{rad}$, and $924\mu\text{rad}$. The properties of these divergence angles are outlined in the Table 9. The alignment between the transmitters and receiver was manually set with the aid of the scopes, installed in each transmitter assembly, depicted in Figure 24.

This section delves into the intricate process of data acquisition, detailing the approach and framework employed, followed by a comprehensive introduction to the organized measurement sets, classified according to weather data pertaining to each distinct divergence.

4.1 MEASUREMENT DATA STRUCTURE

For each angle, a single representative cycle was selected, ensuring optimal alignment between the transmitters and receiver, depicted in Figure 30,31,32, serves to elucidate the measurement cycle and data acquisition process in detail.



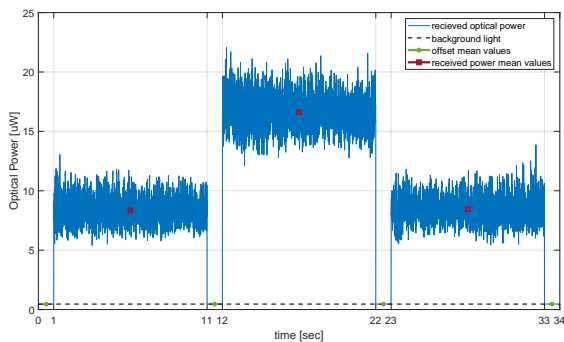
(a) $330\mu\text{rad}$

segment	name	mean value (uW)
0-1s	offset1	2.541
1-11s	TX2	12.255
11-12s	offset2	2.539
12-22s	TXs	24.945
22-23s	offset3	2.459
23-33s	TX1	12.348
33-34s	offset4	2.484

TABLE 11: $330\mu\text{rad}$ segment details

FIGURE 30: $330\mu\text{rad}$ selected measurement data with sample rate 10kHz

4.1 MEASUREMENT DATA STRUCTURE

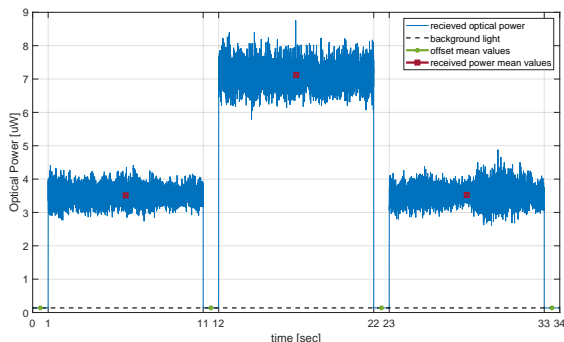


(a) 545urad

FIGURE 31: 545urad selected measurement data with sample rate 10kHz

segment	name	mean value (uW)
0-1s	offset1	0.521
1-11s	TX2	8.356
11-12s	offset2	0.493
12-22s	TXs	16.599
22-23s	offset3	0.418
23-33s	TX1	8.488
33-34s	offset4	0.426

TABLE 12: 545urad segment details



(a) 924urad

FIGURE 32: 924urad selected measurement data with sample rate 10kHz

In the measurement process, each set of data comprises multiple components: the TX2 output power, the combined output power of TX1 and TX2, and the TX1 output power. This data is collected over a duration of 34 seconds as a cycle. Additionally, prior to and following the acquisition of the received optical signal, there is a separate 1-second interval dedicated to capturing background light value. The details of each segment are provided in Table 11, 12, 13.

To obtain precise readings, the mean value of offset periods preceding and succeeding the targeted power vector is calculated and subtracted from each 10-second segment of the optical power data. For instance, the average of the offset values from 0 to 1 second period (offset1) and the subsequent 11 to 12 second period (offset2) is deducted from the TX2 power vector. The same methodology is applied to the TX1 power vector and the combined TX1 and TX2 power vector.

The background light was excluded from consideration as it was subtracted from the data prior to analysis. This methodical approach ensured that the data chosen for analysis was representative

segment	name	mean value (uW)
0-1s	offset1	0.135
1-11s	TX2	3.512
11-12s	offset2	0.137
12-22s	TXs	7.119
22-23s	offset3	0.139
23-33s	TX1	3.525
33-34s	offset4	0.140

TABLE 13: 924urad segment details

4 MEASUREMENT

and conducive to drawing accurate conclusions regarding the behavior and performance of the divergence angles under study.

4.2 TRANSMITTER SEPARATION DISTANCE

This section investigates the impact of transmitter separation distance on transmitter diversity techniques. While previous Section 2.10 has assumed independence between beams transmitted from different transmitters, real-world scenarios may introduce correlations between beams when the separation distance is insufficient. This section aims to experimentally validate the influence of transmitter spacing on the achieved diversity gain.

We hypothesize that while the total mean received power will be the sum of the individual mean powers from each transmitter, the reduction in power scintillation index(PSI) will not be proportional to the number of transmitting antennas if the separation distance is inadequate. This implies that achieving the full benefit of transmit diversity, in terms of improved signal reliability, requires careful consideration of transmitter placement.

Our experiment will explore the relationship between transmitter separation distance and existence of correlation between transmitted beams by measuring the reduction in PSI. The findings will be presented and compared to existing theoretical models of transmit diversity, highlighting the importance of real-world considerations in practical system design.

Figure 33 shows the probability density function (PDF) of the received optical power in a system employing a $330 \mu\text{rad}$ collimator. The corresponding numerical data for each separation distance is provided in Table14.

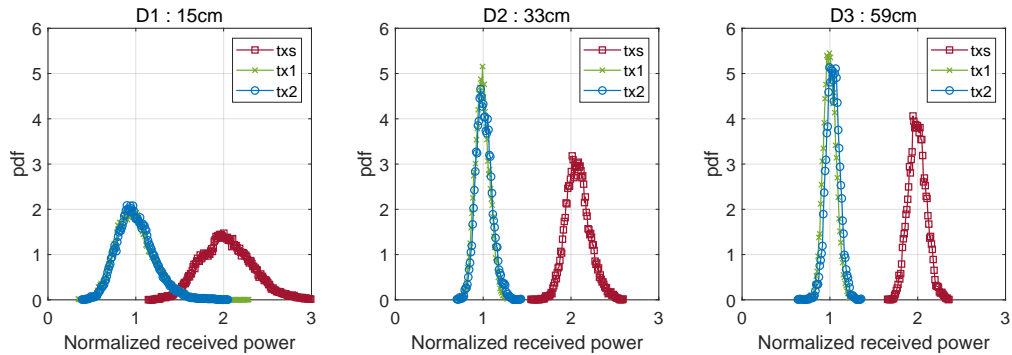


FIGURE 33: 330μ PDF for D1(15cm), D2(33cm), D3(59cm)

4.2 TRANSMITTER SEPARATION DISTANCE

Separation	D1(15cm)	D2(33cm)	D3(59cm)
TX1	8.96	10.29	10.72
TX2	9.02	10.48	10.73
TXs	18.31	21.58	21.41

TABLE 14: 330μ mean output power values in μW with different transmitter separation distances

Here, we focus on the analysis of PDFs from two transmitters (TX1 and TX2) denoted as a "double transmitter set-up." The power vectors received over a 10-second duration for each transmitter and double transmitter set-up were normalized using the average value of the combined mean power from TX1 and TX2.

The key observation from this analysis is that irrespective of the separation distance between the transmitters, the mean received power for the double transmitter configuration is approximately twice the mean received power obtained with a single transmitter setup. This finding aligns with the fundamental principle of transmit diversity, where the addition of independent transmit channels statistically increases the average received power, as estimated in Section 2.10.

Figure 34 depicts the measured PSI the received optical power within a system employing a $330\mu\text{rad}$ collimator. The corresponding numerical data for each separation distance is conveniently presented in Table 15 for ease of reference. The left side of the figure shows the raw PSI values, and the right side shows the PSI values normalized by the PSI values with a double transmitter setup. It is crucial to acknowledge that weather conditions can significantly impact the measurement results. Therefore, the relevant weather data is provided Figure 35.

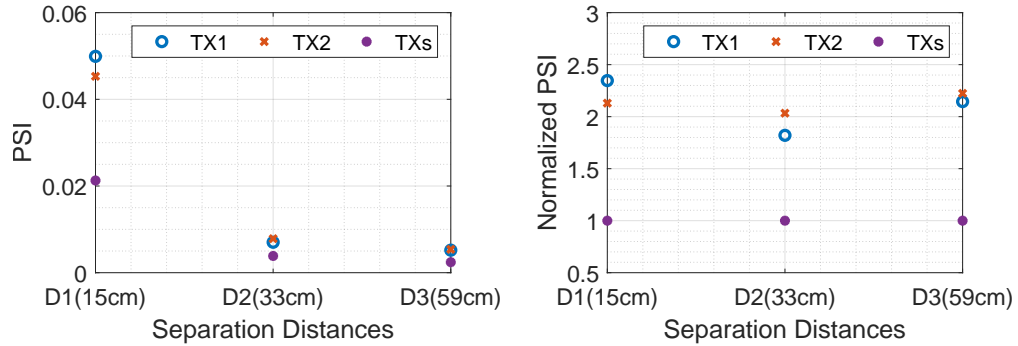


FIGURE 34: 330μ PSI for D1(15cm), D2(33cm), D3(59cm)

4 MEASUREMENT

Separation	D1(15cm)	D2(33cm)	D3(59cm)
TX1	0.05	0.07	0.0052
TX2	0.045	0.08	0.0054
TXs	0.021	0.04	0.0024

TABLE 15: 330μ PSI values for 10s with different transmitter separation distances

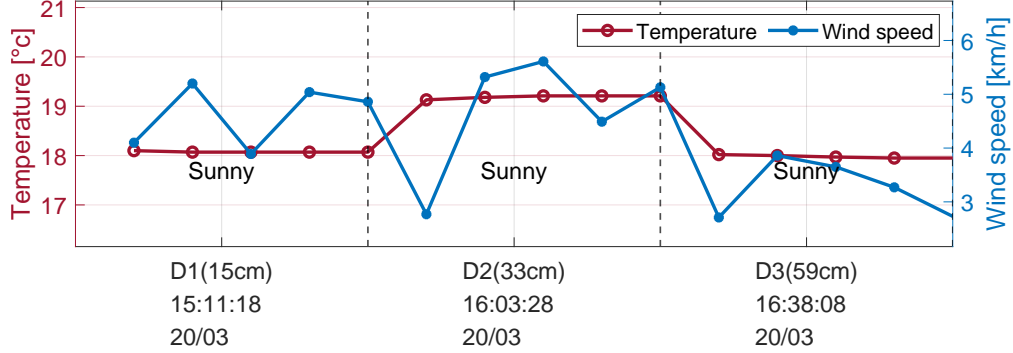


FIGURE 35: weather data for measurement D1(15cm), D2(33cm), D3(59cm)

Our experiment observed a significant scintillation effect, particularly at transmitter separation distances of 15 cm, 33 cm, and 59 cm. Notably, employing a double-transmitter setup reduced the PSI values by a factor of approximately 2-2.5 compared to the single-transmitter case with all separation distances (as shown in Figure 34 and Table 15). These findings suggest a possible relationship between transmitter separation distance and the severity of power scintillation in the received signal. While further research is necessary to fully understand the underlying mechanisms, the results provide initial evidence that the advantages of transmitter diversity in reducing scintillation effects might be achievable even with minimal transmitter separations (15 cm in this case). This observation justifies further investigation with larger transmitter separations beyond 15 cm.

To further explore the interplay between transmitter separation distance and scintillation effects, we repeated the experiment using a 550μ rad collimator with a minimum achievable separation distance of 11 cm. This limitation arose due to physical constraints, as each transmitter assembly component measured 10 cm. The data for this additional configuration can be instrumental in providing a more comprehensive understanding of the relationship between these parameters.

Figure 36 presents the normalized PDF of the received optical power for two transmitter separation distances: 11 cm and 270 cm. As anticipated, the total mean power with the double-transmitter setup is roughly double the value measured with the single-transmitter configuration (detailed values are provided in Table 16). This observation aligns with the expected behavior of increased power due to the additional transmitter.

4.2 TRANSMITTER SEPARATION DISTANCE

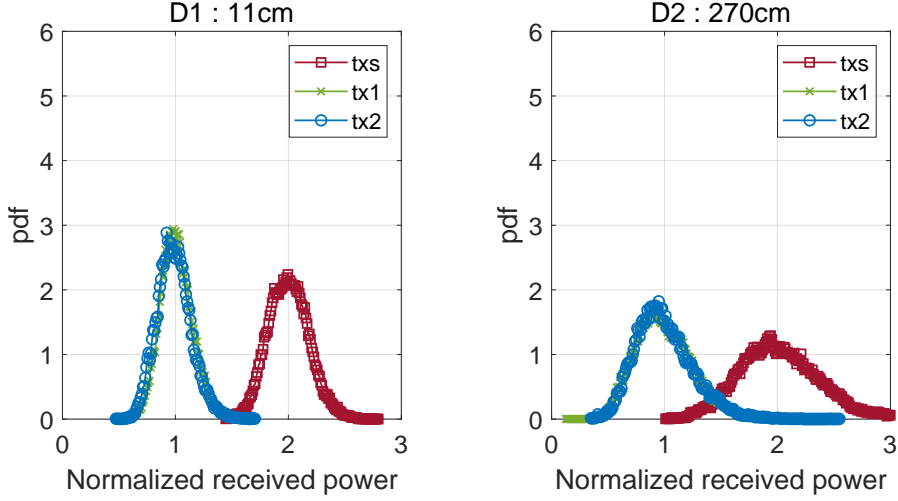


FIGURE 36: 545μ PDF for D1(11cm), D2(270cm)

Separation	D1(11cm)	D2(270cm)
TX1	6.68	8.14
TX2	6.56	8.12
TXs	13.24	16.48

TABLE 16: 545μ mean output power values in μ W with different transmitter separation distances

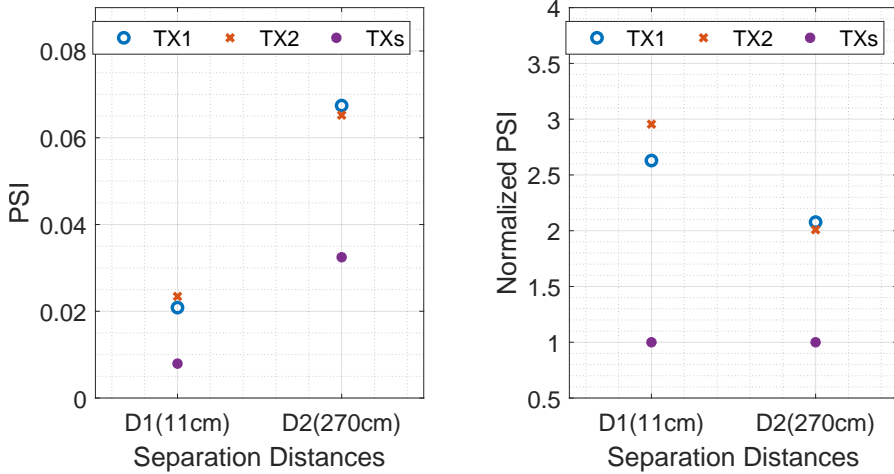


FIGURE 37: 545μ PSI for D1(11cm), D2(270cm)

Interestingly, even at the minimum achievable separation distance of 11 cm, the experiment revealed a clear benefit of transmitter diversity in reducing PSI. Figure 37 illustrates this effect, where the left side shows raw PSI values and the right side shows normalized values relative to

4 MEASUREMENT

Separation	D1(11cm)	D2(270cm)
TX1	0.021	0.067
TX2	0.023	0.065
TXs	0.008	0.033

TABLE 17: 545μ PSI values for 10s with different transmitter separation distances

the double-transmitter setup (refer to Table 17 for specific values). Notably, with a separation of 11 cm, the single-transmitter configuration exhibited PSI values of 0.05 and 0.045, while the double-transmitter setup achieved a significantly lower value of 0.021, representing a reduction of approximately 2.5-3 times. While a reduction of around 2 times was observed for the 270 cm separation distance compared to the single-transmitter case, further experiments employed this larger separation due to the promising results. This decision to utilize the 270 cm separation for subsequent measurements was based on the observations regarding the impact of transmitter separation distance on scintillation effects.

4.3 OVERALL MEASUREMENT STRUCTURE

Ten cycles were selected for each of three radiation angles ($330 \mu\text{rad}$, $545 \mu\text{rad}$, and $924 \mu\text{rad}$) based on optimal transmitter-receiver alignment and having the same mean received power. These cycles were chosen from measurements conducted between March 14th and April 16th. Figure 38 depicts the structure of the selected cycle plots. Each cycle is presented as a separate plot due to being obtained at different times, with the x-axis indicating the date and time for each cycle. The y-axis represents the received power value after background light subtraction (as detailed in the previous Section 4.1). Corresponding weather data for each set of 10 cycles ($330 \mu\text{rad}$, $545 \mu\text{rad}$, and $924 \mu\text{rad}$) will be presented in Chapter 5. The weather data will be structured similarly to the measurement data (Figure 39), with each cycle separated by dotted lines to signify distinct time periods. The time and date information on the weather data plots will correspond to the x-axis of the measurement data plots (Figure 38). The right y-axis will display temperature, while the secondary right y-axis will show wind speed, both being considered critical weather variables for free-space optical communication. General weather conditions (sunny, rainy, cloudy) will be indicated within the graphs using floating text. Any other relevant weather information deemed crucial for analysis will be provided additionally in text format.

4.3 OVERALL MEASUREMENT STRUCTURE

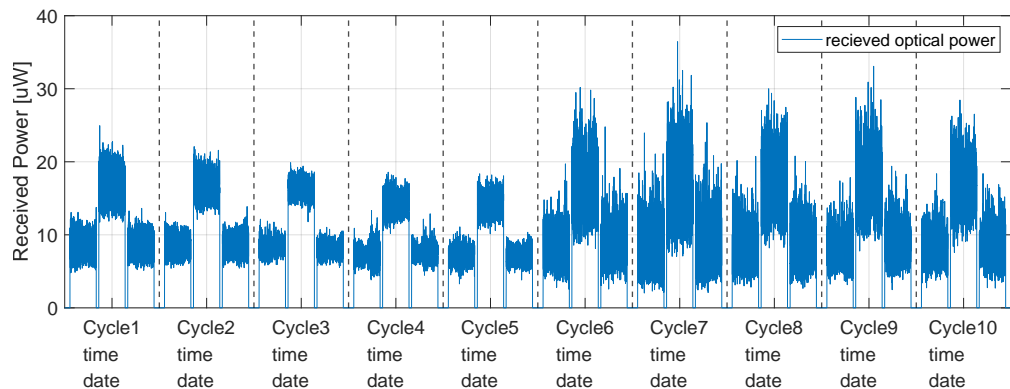


FIGURE 38: 10cycles measurement structure

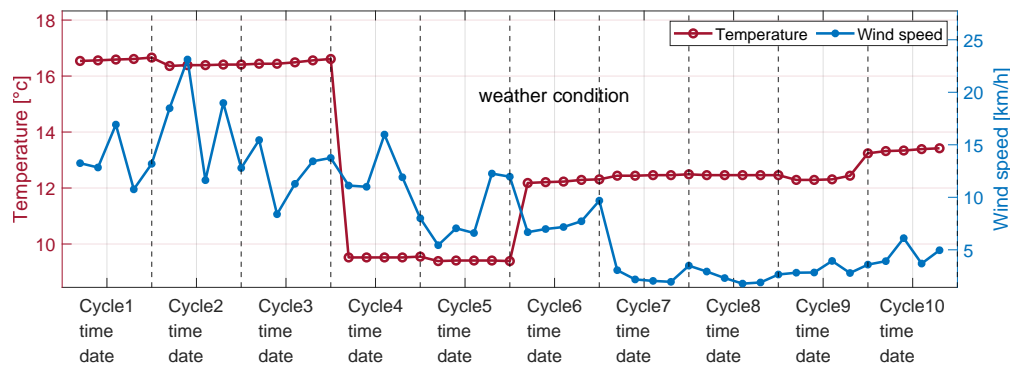


FIGURE 39: 10cycles weather data structure

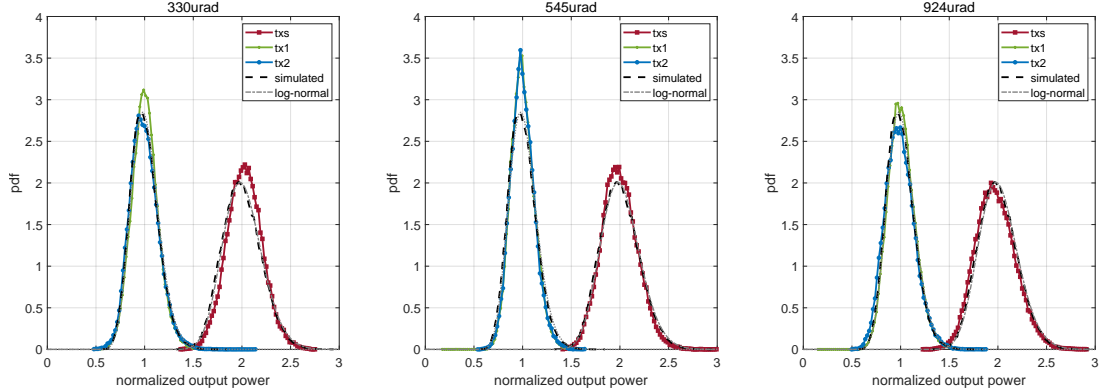
ANALYSIS

5 ANALYSIS

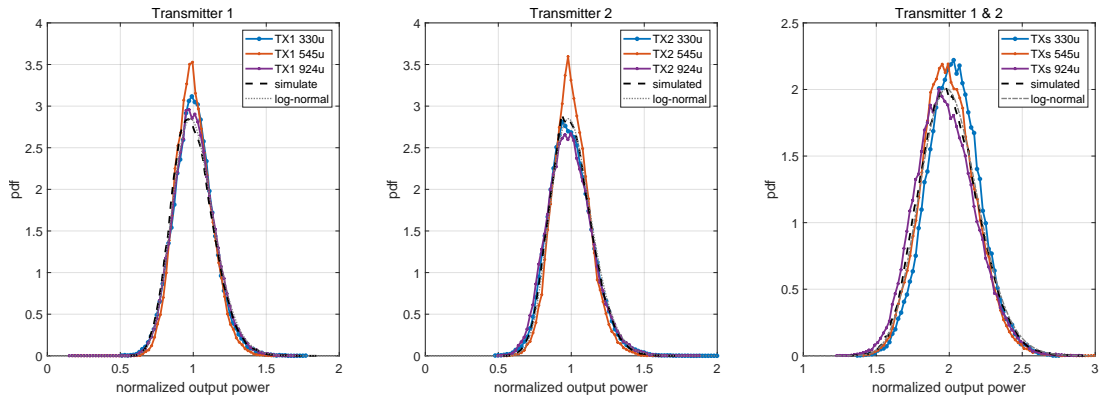
5.1 PROBABILITY DENSITY FUNCTION

To facilitate a comparative analysis of the probability density functions (PDFs) for the received optical power under varying divergence angles, the simulated power vectors generated by the PVGeT tool (described in Section 2.8) were employed. Divergence angles of $330 \mu\text{rad}$, $545 \mu\text{rad}$, and $924 \mu\text{rad}$ were investigated. One cycle of data was selected from each scenario ensuring similar power scintillation index (PSI) values. The specific values for each case are detailed in Table 18.

Figure 40 (a) presents the normalized PDFs for each divergence angle ($330 \mu\text{rad}$, $545 \mu\text{rad}$, and $924 \mu\text{rad}$) across TX1, TX2, and TXs. The normalization process involved dividing the 10-second received optical power data for each case by the average value obtained from the mean values of TX1 and TX2. This normalization aligns with the theoretical expectation that the mean received power for the combined TXs configuration is approximately double that of a single transmitter setup.



(a) PDF for $330\mu\text{rad} / 545\mu\text{rad} / 924\mu\text{rad}$



(b) PDF for TX1 / TX2 / TXs

FIGURE 40: Probability Density Function (PDF)

5.1 PROBABILITY DENSITY FUNCTION

	330 μ rad	545 μ rad	924 μ rad	PVGeT
TX1	0.0181	0.0147	0.0192	0.02
TX2	0.0217	0.0154	0.0231	0.0198
TXs	0.008	0.0085	0.0098	0.01
factor	0.56-0.63	0.42-0.45	0.49-0.58	0.49-0.5

TABLE 18: power scintillation index values from measurement and simulated data

Figure 40 (b) delves deeper into a comparison of the PDFs for TX1, TX2, and TXs. Here, the PDFs are compared against the PDF of a power vector generated by the PVGeT tool, along with theoretical log-normal distributions. The log-normal distributions are represented as $\ln(X) \sim \mathcal{N}(1, 0.02)$ for a single transmitter and $\ln(X) \sim \mathcal{N}(2, 0.01)$ for the double-transmitter configuration (detailed explanations for these distributions can be found in Sections 2.5 and 2.10).

As evident from the graph, all investigated cases exhibited a doubling of the mean power compared to the single-transmitter setup. Notably, the PDFs for single-transmitter cases (TX1 and TX2) with similar PSI values demonstrated good agreement with both the simulated power vector and the theoretical log-normal distribution. Interestingly, for the combined TXs scenario, the variation of the PDF exhibited a slight deviation from both the PVGeT PDF and the log-normal distribution.

The observed reduction in PSI varied depending on the divergence angle. At 330 μ rad, the PSI reduction ranged from 0.56 to 0.63. A slightly less pronounced reduction was observed at 545 μ rad, with a range of 0.42 to 0.45. The divergence angle of 924 μ rad resulted in an intermediate behavior, with PSI values between 0.49 and 0.58. In contrast, the simulated power vector consistently exhibited a precise 0.5 reduction in PSI value (from 0.49 to 0.5).

Figure 41 presents the probability of fade events for each divergence angle (330 μ rad, 545 μ rad, and 924 μ rad) under both single-transmitter (TX1) and double-transmitter (TXs) configurations. Each row in the figure corresponds to a specific divergence angle.

The figure clearly demonstrates a significant reduction in fade probability when employing the double-transmitter configuration compared to the single-transmitter setup for all three divergence angles. The first row depicts the fade probability for the 330 μ rad case, with a noticeable decrease observed when transitioning from TX1 to TXs. Similar trends are evident for the 545 μ rad (second row) and 924 μ rad (third row) configurations. This observed reduction in fade probability aligns with the previously established relationship between PSI values and prevalence of fade events. However, there is no relationship between fades and different divergence angle application.

However, the analysis revealed no significant relationship between the employed divergence angle (330 μ rad, 545 μ rad, and 924 μ rad) and the occurrence of fade events, when they have similar PSI values. This suggests that within the range of divergence angles investigated in this study, the impact of beam collimation on fade probability is negligible compared to other factors, such as the mean received power as will be discussed in next section 5.3.

5 ANALYSIS

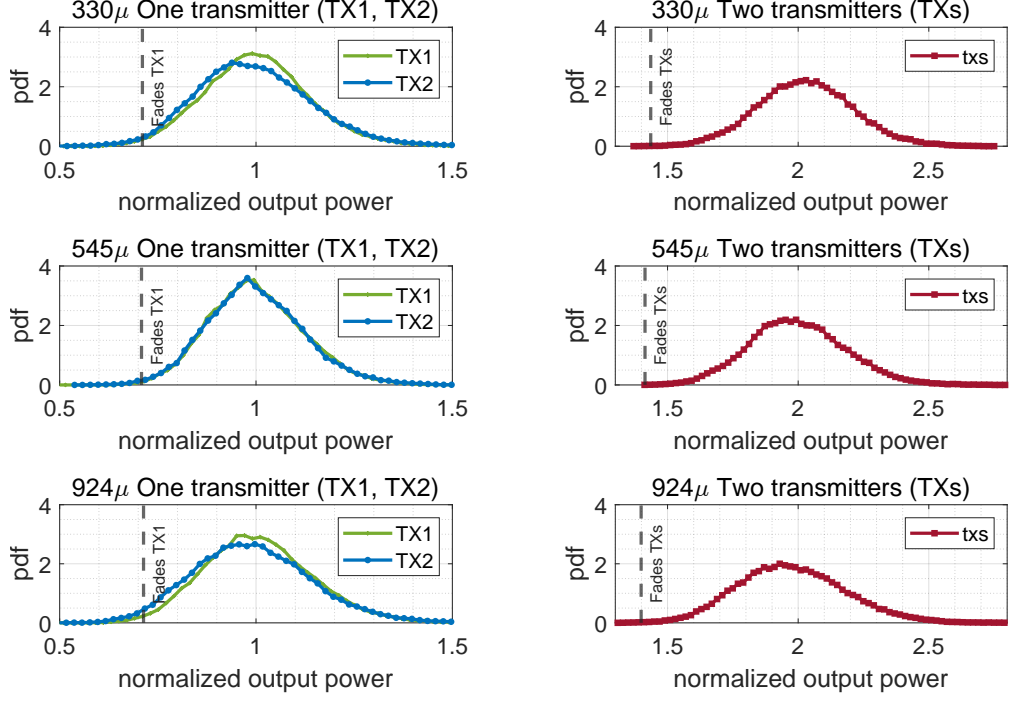


FIGURE 41: Fades probability for 330μ , 545μ and 924μ

Furthermore, the figure suggests the potential for achieving near-zero fade events, especially in scenarios with low PSI values. The text mentions a hypothetical case where the single-transmitter PSI value σ_P^2 is approximately 0.02, while the double-transmitter configuration reduces the PSI to 0.01. This significant decrease in PSI due to transmitter diversity translates to a considerably lower probability of fade events, potentially approaching zero within weak turbulence regimes.

The text highlights a general trend where the overall measured fade events appear to follow the trend of PSI values. A more detailed discussion of this observed correlation and its underlying mechanisms is likely presented in the next section 5.5.

5.2 10 CYCLES OVERALL ANALYSIS

5.2 10 CYCLES OVERALL ANALYSIS

To conduct a thorough examination, ten cycles were chosen for each divergence angle. Optimal positioning between the transmitters and receiver was prioritized to ensure equivalent signal strength and quality from the two transmitters. The cycles were selected across various weather conditions to analyze transmitter diversity in different environmental factors, with the specific conditions listed alongside each graph. To obtain accurate power vector values, a precise approach was followed. The corresponding background light values were subtracted from each power vector, adhering to the detailed method outlined in the previous section 4.1.

Ten measurement cycles were obtained from a Free-Space Optical (FSO) system with a Full Width Half Maximum (FWHM) of $330 \mu\text{rad}$ gaussian beam. Each cycle represents a distinct measurement session at a different date and time. Figure 42 summarizes the mean received power obtained during these cycles. The x-axis denotes the date and time of each measurement, while the markers (various colors and shapes) represent the average power value calculated every 10 seconds within a cycle. The corresponding numerical values are provided in Table 19. Consistent with theoretical expectations, all cycles exhibited a doubling of received power with the double transmitter setup, which agrees well with the theory. (see Section 2.10) However, variations in the absolute mean power values were observed across cycles. Notably, cycles conducted on the same day (e.g., cycles 3-7 and 8-10 on April 15th and 16th, respectively) demonstrated greater similarity in their mean power compared to cycles from different days. This suggests a stronger influence of the date of measurement on the received power compared to the specific time of day.

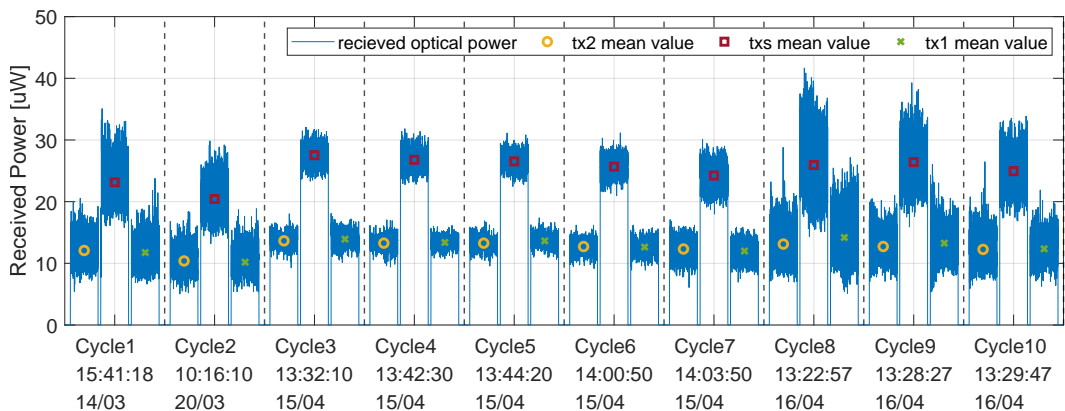


FIGURE 42: $330\mu\text{rad}$ 10cycles measurement

Cycle	1	2	3	4	5	6	7	8	9	10
TX1	11.75	10.19	13.93	13.39	13.64	12.64	12.00	14.19	13.27	12.35
TX2	12.08	10.39	13.65	13.27	13.27	12.72	12.33	13.12	12.73	12.26
TXs	23.14	20.43	27.53	26.79	26.54	25.68	24.23	25.94	26.42	24.95

TABLE 19: $330\mu\text{rad}$ 10cycles mean output power values in μW

5 ANALYSIS

Corresponding weather data for each cycle is presented in Figure 43. Analysis of the general weather conditions revealed that sunny days (e.g., March 20th) exhibited lower mean power compared to days with fair (not strictly sunny or cloudy) conditions (e.g., April 15th). Interestingly, the cloudy and windy day of April 16th displayed higher power variations across cycles 8-10. While these observations suggest a potential link between weather conditions and mean received power value, no direct correlation with temperature or wind speed was identified.

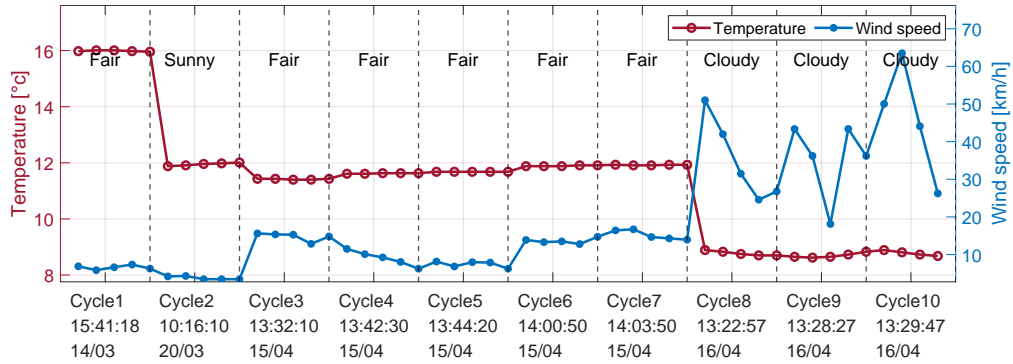


FIGURE 43: 330urad 10cycles weather

The Power Scintillation Index (PSI) was calculated every 10 seconds for each transmitter configuration (single and double) within each measurement cycle. These PSI values were aligned along a common x-axis in Figure 44 (a) to facilitate direct comparison. Figure 44 (b) presents the PSI values normalized by the double-transmitter PSI values, emphasizing the reduction achieved. As observed in Figure 44 (b), the PSI exhibited a reduction factor between 1.5 and 2.7 due to the double-transmitter setup. The specific PSI values are tabulated in Table 20.

While cycle 1-2 displayed relatively high PSI values despite low wind speeds (around 8 km/h), cycle 8-10 (conducted on April 16th) exhibited significantly higher PSI values coinciding with wind speeds ranging from 20 to 65 km/h. These cycles with high wind speeds also demonstrated greater deviations in PSI between the TX1 and TX2 single transmitter configurations, resulting in a decrease factor less or more pronounced than a factor of 2. Conversely, cycle 3-7 (collected on April 15th) showed lower and more stable PSI values, leading to smaller deviations between the transmitter configurations and a decrease factor closer to 2 with the double-transmitter setup.

5.2 10 CYCLES OVERALL ANALYSIS

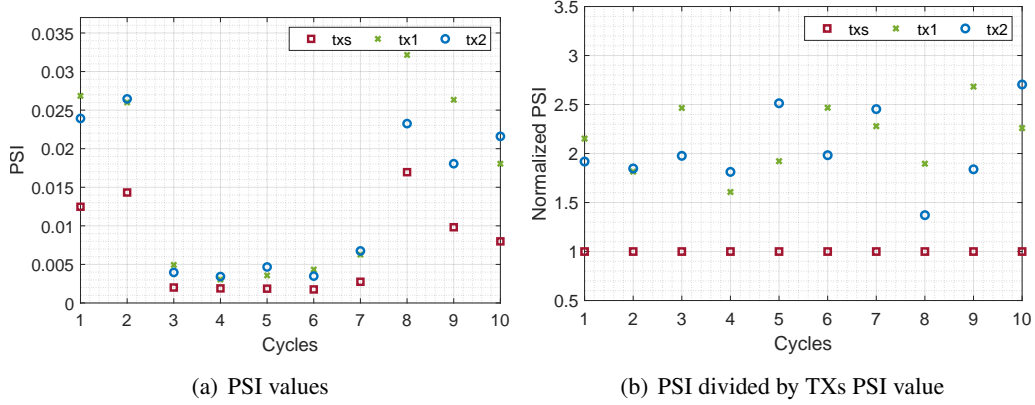


FIGURE 44: $330\mu\text{rad}$ 10cycles PSI

Cycle	1	2	3	4	5	6	7	8	9	10
TX1	26.8	26.0	4.9	3.0	3.6	4.3	6.3	32.2	26.3	18
TX2	23.9	26.5	4.0	3.4	4.7	3.5	6.7	23.3	18.1	21.6
TXs	15.5	14.3	2.0	1.9	1.9	1.8	1.8	17	9.8	8

TABLE 20: $330\mu\text{rad}$ 10cycles PSI values ($\times 10^{-3}$)

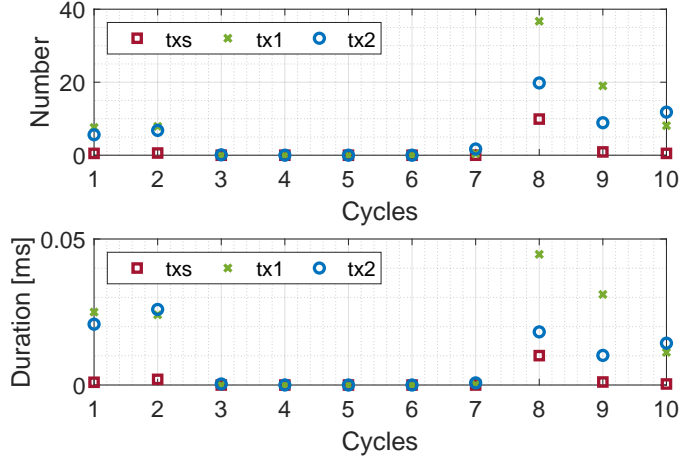


FIGURE 45: $330\mu\text{rad}$ 10cycles fades analysis

Ten measurement cycles were conducted for a Free-Space Optical (FSO) system with a Full Width Half Maximum (FWHM) of $545\mu\text{rad}$. The mean received power values exhibited greater consistency across all cycles compared to the $330\mu\text{rad}$ case, as shown in Figure 46. This figure adopts the established presentation style, with each cycle's mean power directly plotted for visual representation. Corresponding numerical values are provided in Table 21. Figure 47 presents the associated weather data, while Figure 48 incorporates plots of both PSI (Power Scintillation

5 ANALYSIS

Index) values and normalized PSI values for straightforward comparison between single and double transmitter configurations.

Consistent with observations from the $330\mu\text{rad}$ case, cycles conducted on the same day exhibited even more consistent mean power values compared to those from different days. As anticipated with the double transmitter setup, a doubling of the received power was observed. However, no statistically significant correlations were identified between the mean power value and specific weather variables.

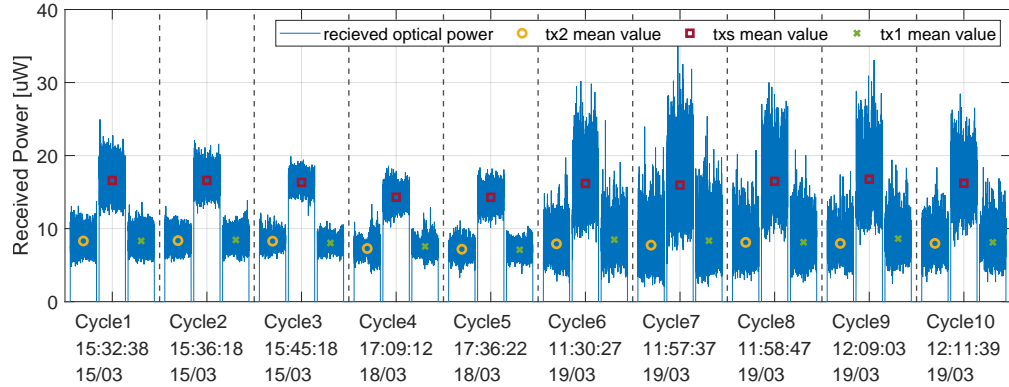


FIGURE 46: $545\mu\text{rad}$ 10cycles measurement

Cycle	1	2	3	4	5	6	7	8	9	10
TX1	8.32	8.45	8.04	7.57	7.10	8.49	8.36	8.14	8.63	8.12
TX2	8.31	8.36	8.28	7.27	7.18	7.92	7.73	8.12	7.97	7.98
TXs	16.59	16.60	16.34	14.30	14.29	16.19	15.95	16.48	16.77	16.21

TABLE 21: 545μ 10cycles mean output power values in μW

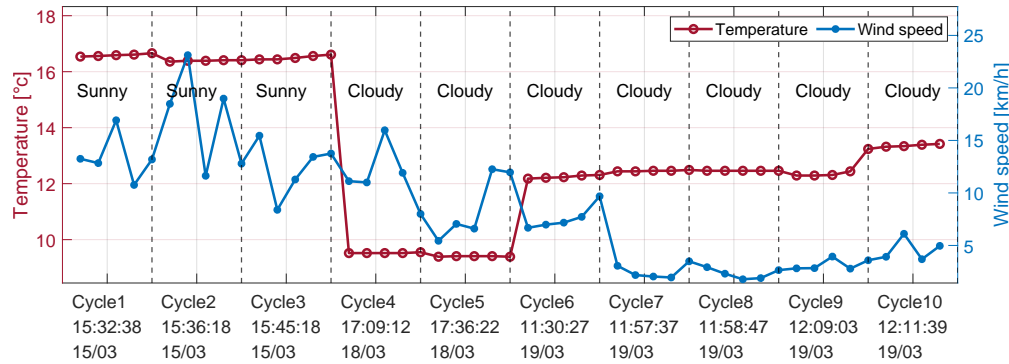


FIGURE 47: $545\mu\text{rad}$ 10cycles weather

Intriguing results were observed for the PSI values presented in Table 22. Cycles 1-3, conducted

5.2 10 CYCLES OVERALL ANALYSIS

on March 15th, a sunny day with relatively high temperatures and moderate wind speeds, exhibited lower PSI values compared to other cycles. These values ranged from 0.007 to 0.0154 for the single-transmitter setup. Conversely, cycles 6-10, measured on March 19th, a cloudy day with low wind speed, displayed significantly higher PSI values. These values, ranging from 0.0467 to 0.1, represented the maximum PSI values across all measurements. Notably, a proportional relationship between wind speed and PSI was not evident for cycles 6-10. Examining Figure 48(b), we observe that cycles 6-10, corresponding to the highest PSI values, exhibited a more pronounced agreement factor of 2 with a single transmitter. This agreement factor translates to a decrease factor of approximately 0.5 when employing the double-transmitter setup.

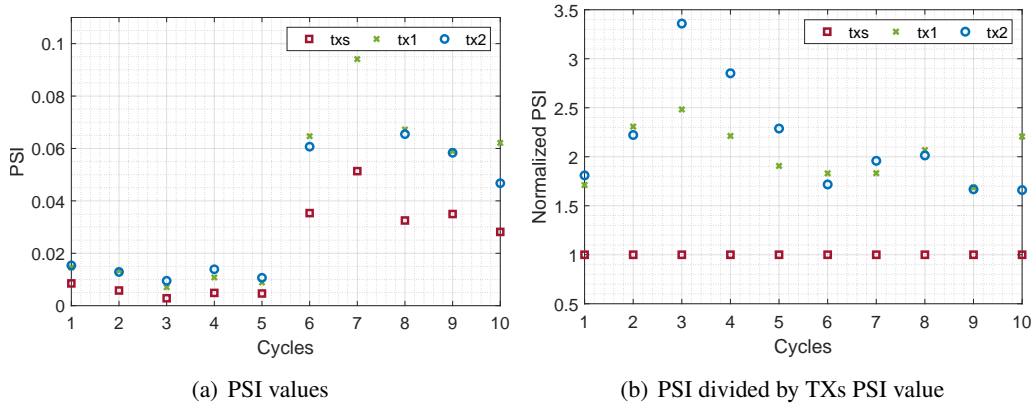


FIGURE 48: 545urad 10cycles PSI

Cycle	1	2	3	4	5	6	7	8	9	10
TX1	14.5	13.4	7	10.8	8.9	64.7	94.1	67.2	59	62.1
TX2	15.4	12.9	9.5	13.9	10.6	60.7	100.6	65.5	58.3	46.7
TXs	8.5	5.8	2.8	4.9	4.7	38.2	51.4	32.5	35.2	28.2

TABLE 22: 545u 10cycles mean PSI values ($\times 10^{-3}$)

5 ANALYSIS

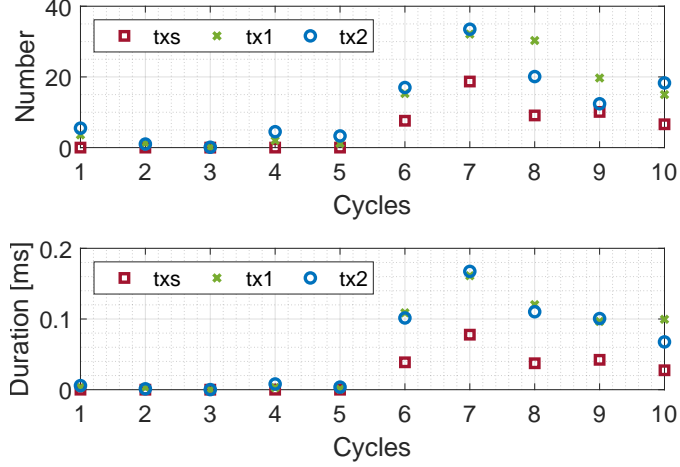


FIGURE 49: $545\mu\text{rad}$ 10cycles fades analysis

Figure 49 depicts the number of fades and their corresponding durations. Similar to the observations for the 330 microradian (μrad) measurement, the trends here closely resemble those identified in the PSI graphs. However, a key difference emerges when examining cycles 6-10, which exhibit higher PSI values. Unlike other measurements, these cycles displayed non-zero fade events even with the double-transmitter setup. Nevertheless, the overall pattern of significantly reduced fade occurrences persists when employing the double-transmitter configuration compared to the single-transmitter setup. Notably, the reduction in fades appears to be approximately halved.

Measurements were conducted for a divergence angle of 924 microradians (μrad) on two separate dates: March 27th and April 16th. As observed with other divergence angles, the received power exhibited variations dependent on the date and time of the measurement. Detailed values are presented in Table 23. The Figure 50 shows the measurement data with mean received power value marker and the Figure 51 is the corresponding weather data. The mean received power on March 27th, a sunny day with low wind speed, ranged from approximately $3.33 \mu\text{W}$ to $3.85 \mu\text{W}$. In contrast, the mean values on April 16th, a cloudy and windy day, fell within the range of $2.49 \mu\text{W}$ to $2.74 \mu\text{W}$. Notably, all measurement cycles displayed a near doubling of received power when employing a double-transmitter setup. Interestingly, no statistically significant correlation was observed between the weather data and the mean power values.

Cycle	1	2	3	4	5	6	7	8	9	10
TX1	3.85	3.76	3.80	3.52	3.33	2.49	2.51	2.58	2.40	2.74
TX2	3.99	3.84	3.83	3.51	3.45	2.60	2.47	2.49	2.48	2.90
TXs	7.78	7.59	7.64	7.12	6.87	5.38	4.92	5.02	5.06	5.54

TABLE 23: $924\mu\text{rad}$ 10cycles mean output power values in μW

5.2 10 CYCLES OVERALL ANALYSIS

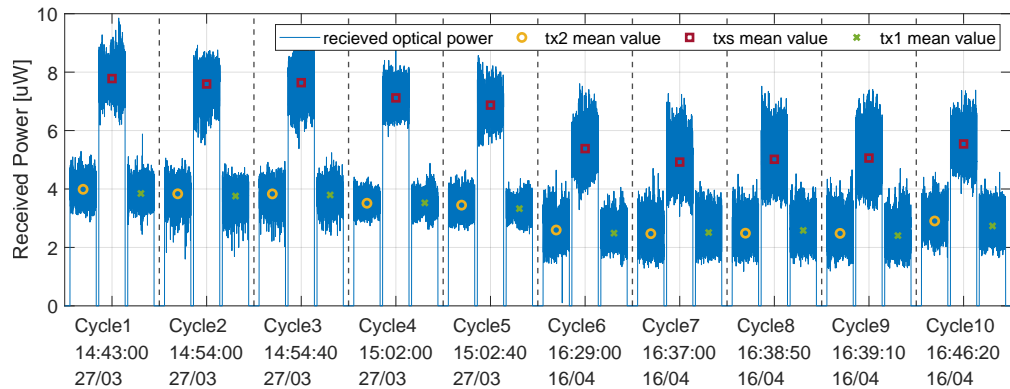


FIGURE 50: 924urad 10cycles measurement

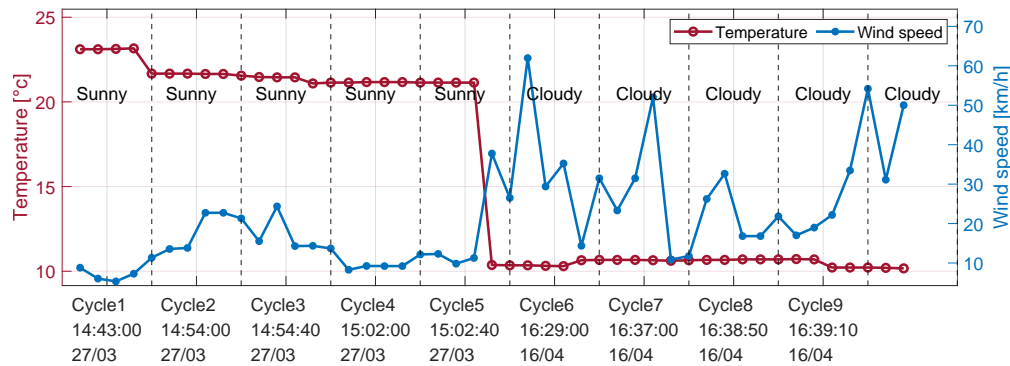


FIGURE 51: 924urad 10cycles weather

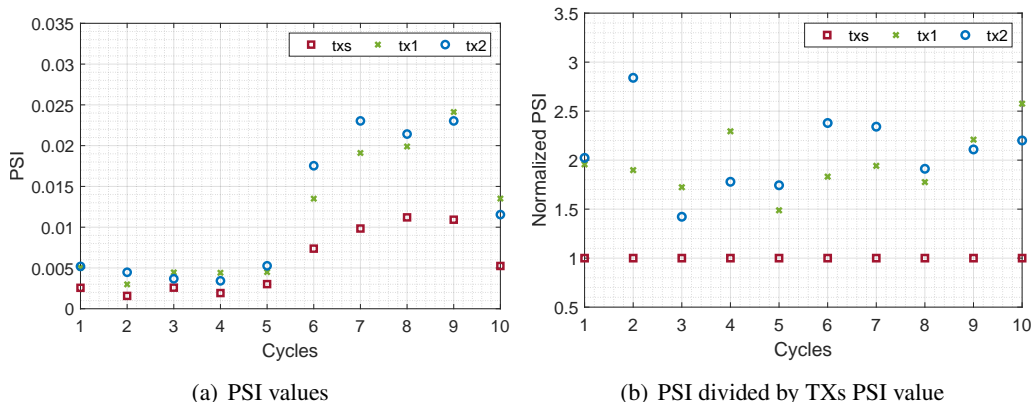


FIGURE 52: 924urad 10cycles PSI

5 ANALYSIS

Cycle	1	2	3	4	5	6	7	8	9	10
TX1	5	3	4.5	4.4	4.5	13.5	19.1	19.9	24.1	13.5
TX2	5.2	4.5	3.7	3.4	5.3	17.5	23	21.4	23	11.5
TXs	2.6	1.6	2.6	1.9	3	7.4	9.8	11.2	10.9	5.2

TABLE 24: 924u 10cycles mean PSI values $\times 10^{-3}$

A comparison between weather data and the PSI was conducted using Figures 51 and 52. Figure 52(a) depicts the original PSI values, which are also detailed in Table 24. Figure 52(b) shows the normalized PSI values relative to the transmitters' PSI value. As anticipated from prior analysis in $330\mu\text{rad}$, a positive correlation between PSI and wind speed was observed. For wind speeds ranging from 10 km/h to 63 km/h, the corresponding PSI values fell within the range of 0.135 to 0.0199. Notably, the magnitude of wind speed, rather than its variation, exhibited a strong link to PSI values. Figure 52(b) further reveals that the factor associated with the one-transmitter setup primarily ranged from 1.5 to 2.5. When the PSI values from Transmitter 1 (TX1) and Transmitter 2 (TX2) were closer, the decrease factor tended towards a value of 0.5. However, the decrease factor exhibited greater variability under conditions with significantly lower PSI values, making analysis more challenging.

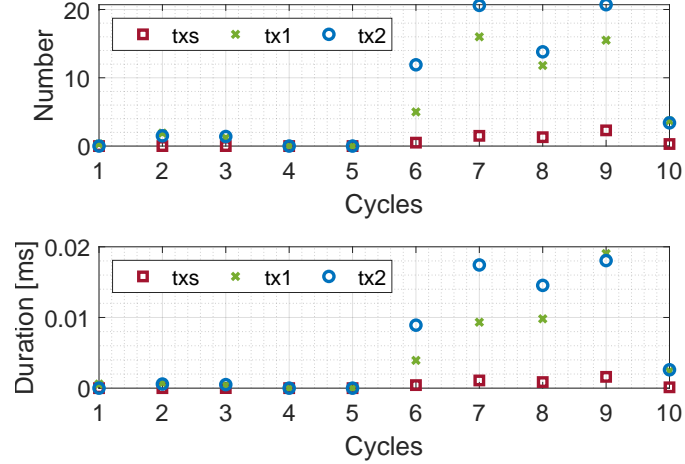


FIGURE 53: 924 μrad 10cycles fades analysis

Figure 53 presents the relationship between the number of fades and their corresponding durations. The observed trends closely resemble those identified for the PSI (Parameter for Scintillation Index). Notably, cycles 1-5, characterized by significantly lower PSI values, exhibited close to zero fades for both single and double-transmitter configurations. Conversely, cycles 6-10, with higher PSI values, displayed a small number of fades with the single-transmitter setup and near-zero fades when employing the double-transmitter configuration.

5.3 MEAN RECEIVED POWER COMPARISON

5.3 MEAN RECEIVED POWER COMPARISON

Figure 54 presents the mean received power measured for three divergence angles: $330 \mu\text{rad}$, $545 \mu\text{rad}$, and $924 \mu\text{rad}$. The data incorporates measurements from ten measurement cycles analyzed in the previous section (Section 5.2). The figure depicts the mean received power of three transmitter configurations: single transmitter (TX1), single transmitter (TX2), and double transmitter (TXs) setup. The x-axis represents the ten measurement cycles. Each data point on the graph corresponds to a specific cycle for a particular transmitter configuration. For instance, the third data point along the x-axis signifies cycle 3 of the ten cycles measurement from each divergence angle for three configurations (TX1, TX2, and TXs).

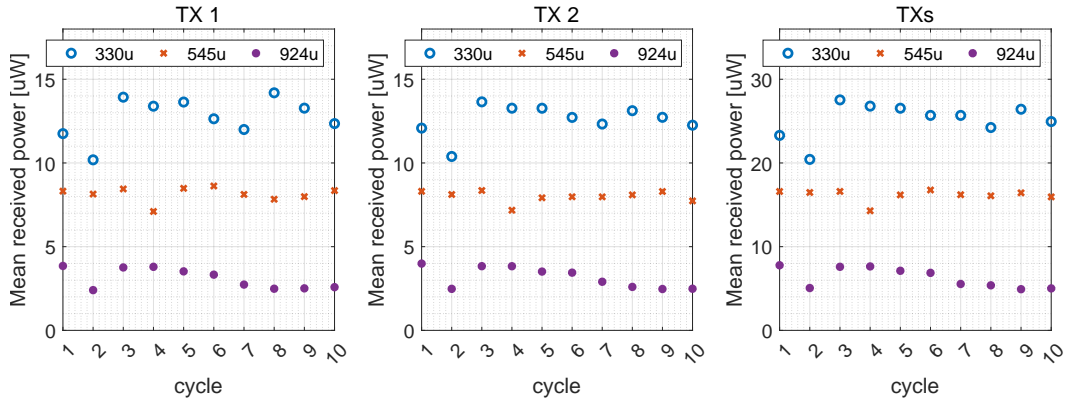


FIGURE 54: Received power 10cycles measurement from TX1, TX2 and TXs for $330\mu\text{rad}$ $545\mu\text{rad}$ and $924\mu\text{rad}$

For the single-transmitter setup, the mean received power across the cycles ranged from 10 to $15 \mu\text{W}$ for the $330 \mu\text{rad}$ divergence angle, 7 to $8 \mu\text{W}$ for the $545 \mu\text{rad}$ divergence angle, and approximately $3 \mu\text{W}$ for the $924 \mu\text{rad}$ divergence angle. Detailed values for each cycle and divergence angle can be found in the corresponding tables: Table 19 for $330 \mu\text{rad}$, Table 21 for $545 \mu\text{rad}$, and Table 23 for $924 \mu\text{rad}$ (all referenced in the previous section 5.2).

As anticipated, the data presented in Figure 54 reveals an inverse relationship between the mean received power and the divergence angle. This observation aligns with theoretical predictions, indicating that smaller divergence angles result in higher received power compared to larger angles. Notably, the measured mean received power values for the $545 \mu\text{rad}$ and $924 \mu\text{rad}$ configurations exhibited close agreement with the estimated received power values calculated in the Link Budget Estimation of the previous section (Section 2.7). These estimated values were $9.43 \mu\text{W}$ and $3.28 \mu\text{W}$, respectively. (Refer to Table 6 within Section 2.7 for the detailed expected power values for each divergence angle.) However, for the $330 \mu\text{rad}$ case, some discrepancies were observed between the measured and estimated values. The expected received power for this configuration was approximately $25.73 \mu\text{W}$, which deviates from the measurement value. However, further investigation into the potential causes of this discrepancy was limited.

Figure 55 illustrates the normalized mean received power for three divergence angles: 330

5 ANALYSIS

microradians (μrad), $330 \mu\text{rad}$, $545 \mu\text{rad}$, and $924 \mu\text{rad}$. This figure summarizes the findings from ten measurement cycles, which were the focus of the analysis detailed in Section 5.2. Each data point within the figure represents a specific measurement cycle(x-axis). To facilitate a more insightful comparison across these cycles and divergence angles, the power vector for each cycle has undergone normalization. This normalization involves dividing the power vector entries by the average value of the mean received power from both Transmitter 1 (TX1) and Transmitter 2 (TX2) for that particular cycle to concentrate solely on the relative trends in the mean received power.

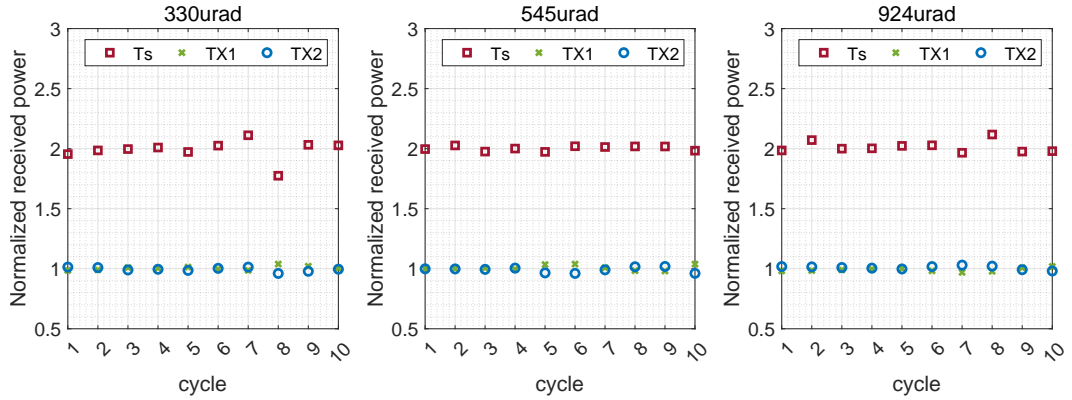


FIGURE 55: Normalized received power 10cycles measurement from $330 \mu\text{rad}$ $545 \mu\text{rad}$ and $924 \mu\text{rad}$

Established in the previous section (Section 2.10), the use of a double-transmitter configuration consistently resulted in an approximate doubling of the normalized mean received power across all ten measurement cycles from $330 \mu\text{rad}$, $545 \mu\text{rad}$, and $924 \mu\text{rad}$. This observed behavior aligns remarkably well with the predictions established by the mathematical theory detailed in Section 2.10. The theory demonstrates that employing multiple beams (denoted by N), leading to a proportional increase in power that scales with the number of beams (N). Furthermore, the results presented here are consistent with the findings from the numerical simulations presented in Section 2.10. These simulations specifically validate the case of $N = 2$, which corresponds to the double-transmitter configuration. They demonstrate an increase in power that scales with this specific value of $N = 2$, thereby corroborating the theoretical predictions.

Importantly, this observed power increase with the double-transmitter configuration holds true for all three divergence angles investigated ($330 \mu\text{rad}$, $545 \mu\text{rad}$, and $924 \mu\text{rad}$). This finding suggests that the effectiveness of the double-transmitter setup in enhancing received power is independent of the divergence angle within the range of angles considered in this study.

5.4 POWER SCINTILLATION INDEX COMPARISON

This section delves into the analysis of the Power Scintillation Index (PSI) measured during the experiment. Figure 56 presents the PSI values measured for three divergence angles: $330\mu\text{rad}$, $545\mu\text{rad}$, and $924\mu\text{rad}$ collimated gaussian beam. The data encompasses measurements from ten measurement cycles analyzed in the previous section (Section 5.2). The figure illustrates the performance of three transmitter configurations: single transmitter (TX1), double transmitter (TX2), and an unspecified TXs setup. The x-axis represents the ten measurement cycles. Each data point on the graph corresponds to a specific cycle for a particular transmitter configuration. For instance, the third data point along the x-axis signifies cycle 3 for all three configurations (TX1, TX2, and TXs).

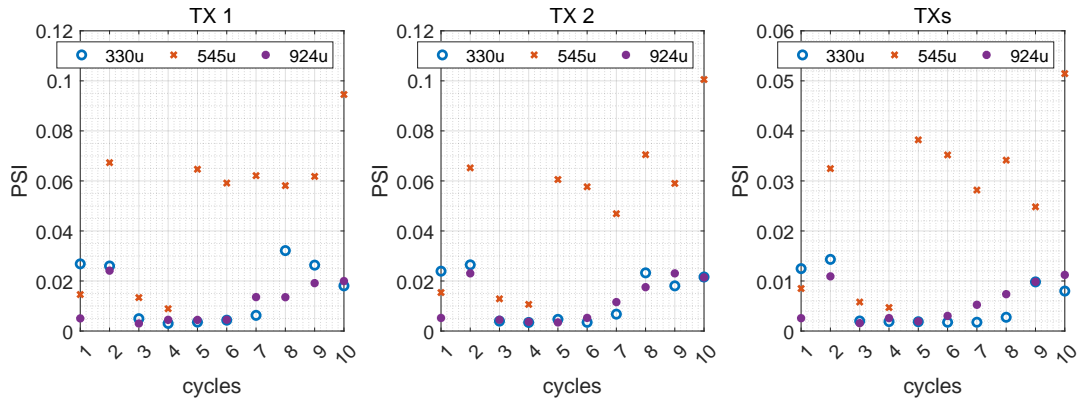


FIGURE 56: PSI values 10cycles measurement from from TX1, TX2 and TXs for $330\mu\text{rad}$ $545\mu\text{rad}$ and $924\mu\text{rad}$

The PSI values for the single-transmitter setup exhibited a range of 0.003 to 0.032 for the $330\mu\text{rad}$ divergence angle, 0.008 to 0.1 for the $545\mu\text{rad}$ divergence angle, and 0.003 to 0.02 for the $924\mu\text{rad}$ divergence angle. Detailed values for each cycle and divergence angle can be found in the corresponding tables: Table 20 for $330\mu\text{rad}$, Table 22 for $545\mu\text{rad}$, and Table 24 for $924\mu\text{rad}$ (all referenced in the previous section 5.2).

Interestingly, the $545\mu\text{rad}$ configuration displayed consistently higher PSI values across all measurements compared to the $330\mu\text{rad}$ and $924\mu\text{rad}$ configurations. Conversely, the $330\mu\text{rad}$ and $924\mu\text{rad}$ configurations yielded comparable PSI values. While scintillation effects are theoretically expected to be more pronounced for smaller divergence angles, the relatively small difference between the angles in this study ($330\mu\text{rad}$, $545\mu\text{rad}$, and $924\mu\text{rad}$) resulted in mathematically predicted and empirically observed similarity in beam scintillation values, as established in the previous section (Section 2.4). This observation aligns well with the theoretical understanding that minimal variations in divergence angles within a small range may not significantly influence PSI values. External factors such as date, time, and weather conditions are likely to have a more substantial impact on PSI. Based on these findings, the comparatively high PSI values observed in the measurements employing the $545\mu\text{rad}$ collimated beam are

5 ANALYSIS

tentatively attributed to specific weather conditions during those measurement cycles.

Figure 57 presents the normalized Power Scintillation Index (PSI) measured for three divergence angles: $330 \mu\text{rad}$, $545 \mu\text{rad}$, and $924 \mu\text{rad}$ collimated beam. This data summarizes the findings from ten measurement cycles analyzed in detail within Section 5.2. Each data point on the x-axis of the figure corresponds to a specific measurement cycle. To facilitate a more insightful comparison between the PSI values obtained under different conditions, a data normalization technique was employed. This technique involved dividing the mean PSI value for each cycle, measured with a single transmitter setup (either TX1 or TX2), by the corresponding mean PSI value measured with the double-transmitter setup (TXs) for that specific cycle. Consequently, the resulting normalized PSI values within the figure focus solely on the relative trends across the different divergence angles and measurement cycles.

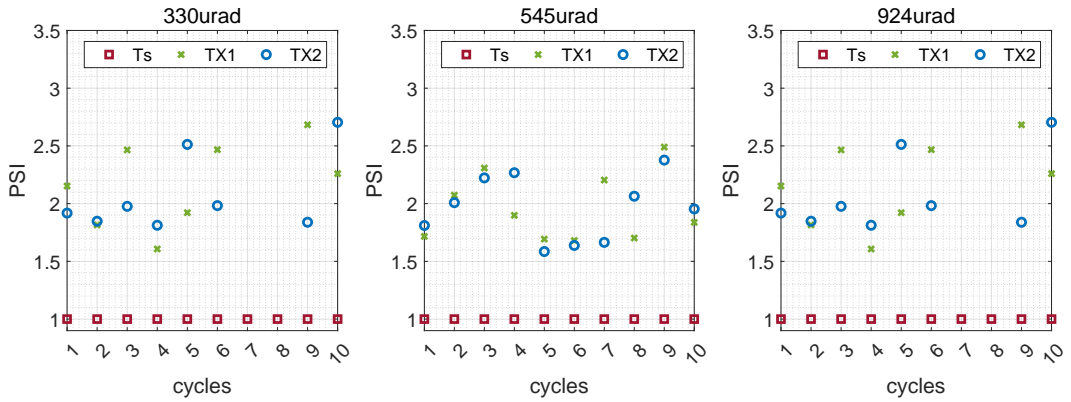


FIGURE 57: Normalized PSI values from $330\mu\text{rad}$ $545\mu\text{rad}$ and $924\mu\text{rad}$

As detailed in Section 2.10, the established mathematical theory posits that utilizing multiple beams (denoted by N) leads to a proportional decrease in the PSI value that scales with the number of beams employed. In essence, the theory suggests a constructive deduction effect, where combining multiple beams mitigates the scintillation experienced by individual beams, resulting in a lower overall PSI. Furthermore, the analysis presented in Section 2.10 anticipated that employing a double-transmitter configuration ($N = 2$) would theoretically result in an approximate halving of the PSI value compared to a single-transmitter setup. This prediction was further supported by the numerical simulations presented in Section 2.10, which were specifically designed to validate the theoretical findings for $N = 2$, demonstrating a decrease in PSI values that scales with this specific value.

However, the empirical data presented in Figure 57 deviates from the theoretical predictions and the anticipated outcome of the simulations. The figure illustrates that the PSI values measured with the single-transmitter setup (TX1 and TX2) were approximately 1.6 to 2.6 times higher than those measured with the double-transmitter setup (TXs) for all three divergence angles ($330 \mu\text{rad}$, $545 \mu\text{rad}$, and $924 \mu\text{rad}$). Additionally, within each divergence angle configuration, it was difficult to discern a clear distinction between the values obtained with TX1 and TX2. This observed

5.4 POWER SCINTILLATION INDEX COMPARISON

discrepancy between the theoretical expectation of a proportional decrease in PSI with N and the empirical data displaying a less pronounced decrease, potentially even an increase, necessitates further investigation.

While the observed data in Figure 57 deviates from the theoretical prediction of a perfect halving of the PSI value with the double-transmitter configuration ($N = 2$), it is important to acknowledge some key observations within this discrepancy.

Firstly, the data consistently demonstrates a significant level of reduction in PSI values when employing the double-transmitter setup (TXs) compared to the single-transmitter setup (TX1 and TX2) across all ten measurement cycles and for all three divergence angles ($330 \mu\text{rad}$, $545 \mu\text{rad}$, and $924 \mu\text{rad}$). This observation underscores the effectiveness of the double-transmitter configuration in mitigating scintillation effects, even if the reduction is not a precise halving as predicted by the theory.

Secondly, the data suggests a potential correlation between the similarity of PSI values from TX1 and TX2 and the observed decrease in the combined PSI (TXs). When the PSI values measured with TX1 and TX2 were relatively close within a specific measurement cycle and same divergence angle configuration, the decrease in the combined PSI (TXs) approached the anticipated halving value. This observation suggests that when both transmitters encounter independent but similar atmospheric conditions along their respective optical paths, the combined effect on scintillation is more closely aligned with the theoretical prediction based on a uniform environment.

5 ANALYSIS

5.5 FADES COMPARISON

This section delves into the analysis of fade events observed during the experiment. Fade events are characterized by temporary reductions in received signal power. In this study, a fade event was defined as a decrease in received power exceeding 1.5 dB below the mean received power level. Figure 58 presents a comprehensive overview of the fade data, encompassing both the number of fades and their respective durations.

The data originates from ten measurement cycles conducted for each of the three divergence angles employed in the previous section (Section 5.2). These divergence angles are $330 \mu\text{rad}$, $545 \mu\text{rad}$, and $924 \mu\text{rad}$. The x-axis of Figure 58 represents these ten measurement cycles for each divergence angle. This organization facilitates a clear comparison of fade events across different measurement cycles.

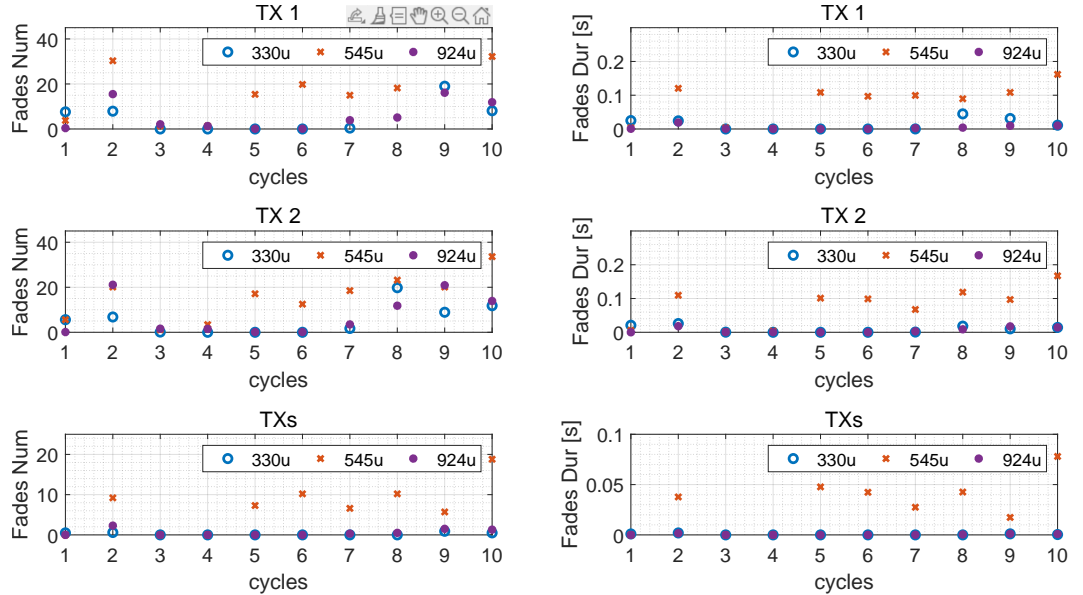


FIGURE 58: Number of fades and duration 10cycles measurement from from TX1, TX2 and TXs for $330\mu\text{rad}$ $545\mu\text{rad}$ and $924\mu\text{rad}$

The figure employs a two-column format to differentiate between the number of fades and their durations. The left column visually depicts the number of fades experienced for each configuration within a specific measurement cycle and divergence angle combination. Conversely, the right column illustrates the corresponding durations of these fades. The data is further organized by transmitter configuration across three rows. The first row showcases the number and duration of fades for each divergence angle ($330 \mu\text{rad}$, $545 \mu\text{rad}$, and $924 \mu\text{rad}$) when employing the single-transmitter configuration TX1. The second row follows the same format, presenting the number and duration of fades for each divergence angle when utilizing the single-transmitter configuration TX2. Finally, the third row depicts the number and duration of fades for each

5.5 FADES COMPARISON

divergence angle when employing the double-transmitter configuration TXs, which combines the signals from TX1 and TX2.

Similar to the PSI trends, observed in previous section 5.5 , the data on fade events, presented in Figure 58, reveals a dependence on PSI values. The data suggests that the $545 \mu\text{rad}$ divergence angle exhibits a higher number of fade events compared to both the $330 \mu\text{rad}$ and $924 \mu\text{rad}$ configurations for all transmitter setups (TX1, TX2, and TXs). This observation aligns with the trend observed for PSI values, where the $545 \mu\text{rad}$ configuration exhibited higher scintillation.

Interestingly, some measurement cycles for the $330 \mu\text{rad}$ and $924 \mu\text{rad}$ configurations experienced close to zero fade events, even with the single-transmitter setup (TX1 and TX2). This observation suggests that under specific atmospheric conditions and for these particular divergence angles, the impact of scintillation might be minimal, resulting in very few or even no fade events. Furthermore, when employing the double-transmitter configuration (TXs) for these divergence angles, the number of fade events approaches zero across all ten measurement cycles. This aligns with the expectation that combining multiple beams can significantly mitigate scintillation effects, potentially leading to near-elimination of fade events under specific conditions.

Similar to the observations with PSI values, the data indicates that TX1 and TX2 experience somewhat different fade occurrence and durations. However, the deviation in fade characteristics between the two single-transmitter setups (TX1 and TX2) appears to be more subtle compared to the observed discrepancies in PSI values. While the previous analysis (Section 5.2) struggled to definitively establish a specific "decrease factor" in fades decrease with the double-transmitter setup, the y-axis of Figure 58 suggests a trend towards an approximate halving of both the number and duration of fades when employing TXs compared to the single-transmitter configurations. This observed reduction aligns more closely with the theoretical prediction of a proportional decrease in scintillation with additional beams (N).

Despite the limited number of fade events observed for the short horizontal distance configurations, the data offers valuable insights. It demonstrates a clear trend of significantly reduced fade events with the double-transmitter setup for all three divergence angles ($330 \mu\text{rad}$, $545 \mu\text{rad}$, and $924 \mu\text{rad}$). This suggests that employing a double-transmitter configuration has the potential to achieve near-zero fade events and minimal signal variations for short-distance links. However, it is important to acknowledge that this conclusion is based on a limited dataset focused on short distances. Further research with longer link distances and more diverse atmospheric conditions is necessary to confirm the generalizability of these observations.

Following the analysis presented in Section 5.4, 5.5, and Figure 59 delves into the relationship between fade events and PSI values for the single-transmitter configuration TX1 and Figure 60 for TX2. The data originates from ten measurement cycles conducted for each of the three previously employed divergence angles: $330 \mu\text{rad}$, $545 \mu\text{rad}$, and $924 \mu\text{rad}$. The figure utilizes a two-axis presentation to facilitate a comprehensive comparison.

The x-axis of Figure 59 represents the ten measurement cycles for each divergence angle, allowing for a direct comparison of PSI values and fade event characteristics across different measurement

5 ANALYSIS

periods and atmospheric conditions. The left-hand y-axis depicts the corresponding PSI values for each data point, while the right-hand y-axis represents the number of fade events observed during each measurement cycle. This dual-axis approach enables a visual exploration of the potential relationship between signal scintillation (reflected in PSI values) and the occurrence of fade events (represented by the number of fades).

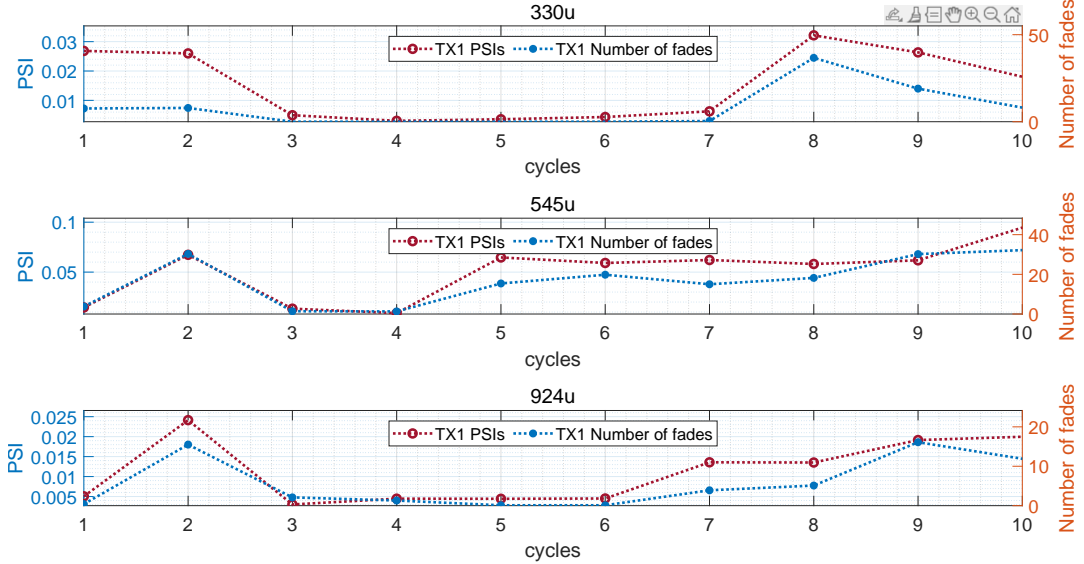


FIGURE 59: PSI values and fades from $330\mu\text{rad}$ $545\mu\text{rad}$ and $924\mu\text{rad}$

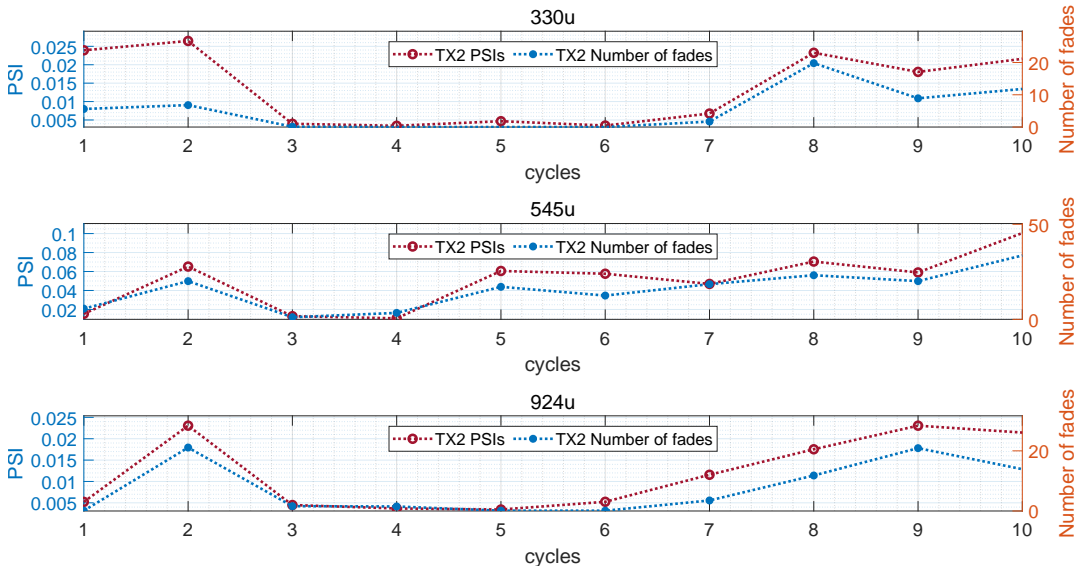


FIGURE 60: PSI values and fades from $330\mu\text{rad}$ $545\mu\text{rad}$ and $924\mu\text{rad}$

CONCLUSION

6 CONCLUSION

This study investigates the effectiveness of transmitter diversity in mitigating signal degradation caused by atmospheric turbulence in free-space optical communication systems. The analysis focuses on a horizontal link with a short distance and employs three different beam divergence angles. The benefits of transmitter diversity were established through both theoretical and numerical simulations. These theoretical predictions were then compared with experimental measurements conducted between March 15th and April 16th at various times and dates.

Due to the limitations of manual alignment between the transmitter and receiver, ten measurement cycles were selected for each divergence angle from the entire dataset. These cycles were subsequently analyzed in detail within Section 5.2. Each selected cycle comprises 10 seconds of power vector data from the single transmitter (TX1), followed by 10 seconds of data from each transmitter (TX1 and TX2) combined (TXs). Power Scintillation Index (PSI) values were calculated using the equations (39) and fades threshold was defined as -1.5dB from mean power values, referenced in section 2.5

Building upon the link budget calculations presented in Section 2.7, this section analyzes the received power measured during the experiment. As predicted, a smaller divergence angle (330 μrad) resulted in a higher mean received power compared to the wider divergence angles (545 μrad and 924 μrad). The measured power for 545 μrad and 924 μrad configurations exhibited good agreement with the expected values, with slight deviations. However, the 330 μrad configuration displayed a larger deviation. This higher sensitivity to alignment for the narrower beam profile (330 μrad) is likely due to its tighter collimation, making it more susceptible to misalignment between the transmitter and receiver. Furthermore, the analysis revealed that data collected on the same date tended to exhibit more consistent mean received power compared to data collected across different dates. This suggests that variations by date in atmospheric conditions can influence the received power. Additionally, the analysis observed a correlation between weather conditions and received power stability. Fair weather conditions led to more stable power levels within individual measurement cycles, while cloudy or windy conditions resulted in greater variations in the mean power across cycles. However, a direct relationship between specific weather parameters and the mean received power could not be established.

As established in Section 2.4, the separation distance increases, the correlation between the beams weakens. This translates to a greater improvement in the Power Scintillation Index (PSI) with wider transmitter separations. Limitations associated with the transmitter hardware assembly restricted the achievable separation distances during the measurements. For the transmitter divergence angle of 330 microrads, separations of 15 cm, 27 cm, and 51 cm were employed. While the separation distances used for the 545 microrad divergence angle (11 cm and 270 cm) differed, a significant performance difference in transmitter diversity was not observed between these specific distances. This finding provides confidence in assuming independence between the two beams for the larger separation distance of 2.7 meters employed in the main analysis.

According to the multi-beam and double-transmitter theories outlined in Section 2.10, a theoretical reduction of PSI by half ($N=2$) is expected when employing a double-transmitter configuration, but only if the separation distance exceeds the correlation length. Despite utilizing the shortest

separation distances exceeding the correlation length for each divergence angle, both configurations (330 μ rad and 545 μ rad) still demonstrated a factor-of-two improvement with transmitter diversity. This translates to a near-halving of the PSI values with the double-transmitter configuration compared to the single-transmitter setup. As confirmed by separate analysis in section 4.2, the most commonly used configuration, the separation of 2.7 meters ensured independence of the beams from each other.

As described in the theoretical Section 2.10, employing a double-transmitter configuration with separation between transmitters larger than correlation length (r_0) was predicted to yield a doubling of the mean received power compared to the single-transmitter setup. The measured mean received power with the double-transmitter configuration (TXs) closely matched the theoretical prediction across all ten measurement cycles and for all three divergence angles (330 μ rad, 545 μ rad, and 924 μ rad). This observation confirms the effectiveness of the transmitter diversity technique in enhancing the received power under various weather conditions and for different beam divergence angles. Detailed power values for each measurement cycle are presented in Section 5.2 and further analysis is provided in Section 5.3.

The measurements were conducted within a weak turbulence regime, characterized by a scintillation index σ_P^2 below 1. As established in the theoretical section (Section 2.5), Rytov approximation predicts a log-normal distribution for the power vector of each individual transmitter (TX1 and TX2) under such conditions. Furthermore, based on mathematical and numerical simulations in section 2.10, the combined power vector from the double-transmitter configuration (TXs) was also expected to exhibit a log-normal distribution. The measured probability density functions (PDFs) for the power vectors of both TX1 and TX2 confirmed the theoretical prediction, displaying a log-normal distribution. However, the measured PDF for the combined power vector from TXs exhibited a distribution that resembled, but did not perfectly match, a log-normal distribution. This deviation from the ideal log-normal behavior for the double-transmitter configuration warrants further investigation.

Building upon the theoretical foundation established in Section 2.10, the implementation of a double-transmitter configuration (TXs) demonstrably reduces the probability of fade events. This reduction is attributed to the significant decrease in the Power Scintillation Index (PSI) value observed with the double-transmitter setup. The theoretical analysis in Section 2.10 suggested the potential for near-elimination of fade events in weak turbulence regimes. The experimental results presented here support this prediction, demonstrating a near-zero occurrence of fades, particularly for the 330 μ rad and 924 μ rad divergence angle measurements. These configurations exhibited lower PSI values compared to the 545 μ rad configuration, further solidifying the dependence of fade events on power scintillation. Detailed measurement data for all configurations can be found in Section 5.2, with a comprehensive analysis provided in Section 5.1. Further investigation with a wider range of turbulence conditions is necessary to determine the generalizability of these findings across diverse atmospheric scenarios.

As anticipated in the mathematical predictions and numerical simulations presented in Section 2.10, the double-transmitter setup demonstrably reduces the PSI value. The PSI was

6 CONCLUSION

calculated for each 10-second power vector of each cycle from TX1, TX2, and TXs using the equation introduced earlier equation (39) in Section 2.5. The measurements confirmed a significant decrease in PSI values when employing the double-transmitter configuration compared to the single-transmitter setups. Furthermore, the observed decrease factor approached the predicted value of 0.5, particularly in cases where the single transmitters (TX1 and TX2) exhibited similar initial PSI values. However, significant variations in PSI were observed between individual measurement cycles and within each cycle, likely due to fluctuations in atmospheric conditions. These variations resulted in discrepancies between the PSI values of TX1 and TX2 within individual cycles. Consequently, the actual decrease factor for the double-transmitter configuration ranged from 0.4 to 0.6 across most measurements for all three divergence angles ($330 \mu\text{rad}$, $545 \mu\text{rad}$, and $924 \mu\text{rad}$). Interestingly, no significant correlation was observed between the divergence angle and the PSI value itself. This suggests that the primary factor influencing the PSI values is likely weather conditions, including specific date and time of the measurement. While a narrower beam profile (smaller divergence angle) might theoretically lead to higher scintillation, the impact of such variations appears to be overshadowed by the influence of atmospheric turbulence during the experiment.

LIST OF ACRONYMS

UAV	Unmanned Aerial Vehicles
FSOC	Free-Space Optical Communication
FSO	Free-Space Optical
ITU	International Telecommunications Unit
OGS	Optical Ground Station
RF	Radio Frequency
SNR	Signal-to-Noise Ratio
WDM	Wavelength Division Multiplexing
FWHM	Full-Width-Half-Maximum
FSPL	Free-Space Path Loss
CW	Continuous-Wave
IRT	Index of Refraction Turbulence
PSI	Power Scintillation Index
PDF	Probability Density Function
MCF	Mutual Coherence Function
rms	root-mean-square
WSF	Wave Structure Function
SIMO	Single Input Multiple Output
MISO	Multiple Input Single Output
MIMO	Multiple Input Multiple Output
BER	Bit Error Rate
PPM	Pulse-Position Modulation
OOK	On-Off Keying
IM/DD	Intensity Modulation / Direct Detection (IM/DD)

LIST OF ACRONYMS

BPF	Band-pass Filter
DAC	digital-analog converter
DC	direct current

BIBLIOGRAPHY

- [1] E. Korevaar, I. Kim, and B. McArthur, “Atmospheric propagation characteristics of highest importance to commercial free space optics,” *Proceedings of SPIE - The International Society for Optical Engineering*, Apr. 2003. doi: 10.1117/12.483804.
- [2] I. I. Kim and E. J. Korevaar, “Availability of free-space optics (FSO) and hybrid FSO/RF systems,” in *Optical Wireless Communications IV*, E. J. Korevaar, Ed., International Society for Optics and Photonics, vol. 4530, SPIE, 2001, pp. 84–95. doi: 10.1117/12.449800.
- [3] E. Shettle, “Models of aerosols, clouds, and precipitation for atmospheric propagation studies,” *AGARD Conf. Proce.*, vol. -1, 1990.
- [4] L. C. Andrews, R. L. Phillips, and P. T. Yu, “Optical scintillations and fade statistics for a satellite-communication system,” *Appl. Opt.*, vol. 34, no. 33, pp. 7742–7751, Nov. 1995. doi: 10.1364/AO.34.007742.
- [5] A. Paulraj, R. Nabar, and D. Gore, “Introduction to space-time wireless communications [m],” Jan. 2003.
- [6] D. Kedar and S. Arnon, “Urban optical wireless communication networks: The main challenges and possible solutions,” *IEEE Communications Magazine*, vol. 42, no. 5, S2–S7, 2004. doi: 10.1109/MCOM.2004.1299334.
- [7] L. Andrews and R. Phillips, “Laser beam propagation through random media,” in Jan. 2005, ISBN: 0819459488. doi: 10.1117/3.626196.
- [8] L. C. Andrews, R. L. Phillips, and C. Y. Young, “Modeling optical scintillation,” in SPIE, pp. 67–97, <https://www.spiedigitallibrary.org/ebooks/PM/Laser- Beam- Scintillation-with - Applications/2/Modeling - Optical - Scintillation/10.1117/3.412858.ch2>. doi: 10.1117/3.412858.ch2.
- [9] H. Kaushal and G. Kaddoum, “Optical communication in space: Challenges and mitigation techniques,” *IEEE Communications Surveys Tutorials*, vol. 19, no. 1, pp. 57–96, 2017. doi: 10.1109/COMST.2016.2603518.
- [10] E. Lee and V. Chan, “Part 1: Optical communication over the clear turbulent atmospheric channel using diversity,” *Selected Areas in Communications, IEEE Journal on*, vol. 22(9), pp. 1896–1906, Dec. 2004. doi: 10.1109/JSAC.2004.835751.
- [11] S. M. Navidpour, M. Uysal, and M. Kavehrad, “Ber performance of free-space optical transmission with spatial diversity,” *IEEE Transactions on Wireless Communications*, vol. 6, no. 8, pp. 2813–2819, 2007. doi: 10.1109/TWC.2007.06109.
- [12] N. H. M. Noor, A. W. Naji, and W. Al-Khateeb, “Theoretical analysis of multiple transmitters/receivers on the performance of free space optics (fso) link,” in *Proceeding of the 2011 IEEE International Conference on Space Science and Communication (IconSpace)*, 2011, pp. 291–295. doi: 10.1109/IConSpace.2011.6015903.

BIBLIOGRAPHY

- [13] H. Kaushal, V. Jain, and S. Kar, “Free-space optical channel models,” in Jan. 2017, pp. 41–89, ISBN: 978-81-322-3689-4. doi: 10.1007/978-81-322-3691-7_2.
- [14] H. Hemmati, *Near-earth laser communications*. Jan. 2009, pp. 1–403.
- [15] L. Andrews, R. Phillips, and C. Hopen, *Laser Beam Scintillation with Applications* (Online access with subscription: SPIE Digital Library). Society of Photo Optical, 2001, ISBN: 9780819441034.
- [16] I. Kim, B. Mcarthur, and E. Korevaar, “Comparison of laser beam propagation at 785 nm and 1550 nm in fog and haze for optical wireless communications,” *Proc. SPIE*, vol. 4214, Feb. 2001. doi: 10.1117/12.417512.
- [17] M. Alnaboulsi and F. Fornel, “Fog attenuation prediction for optical and infrared waves,” *Optical Engineering*, vol. 43, pp. 319–329, Feb. 2004. doi: 10.1117/1.1637611.
- [18] A. Yariv, *Lasers*. Holt, Rinehart and Winston, 1982.
- [19] A. E. Siegman, *Gaussian Beams and Their Applications*. 1973.
- [20] A. M. Carrillo Flores, D. Giggenbach, M. T. Knopp, D. Orsucci, and A. Shrestha, “Effects of pointing errors on intensity losses in the optical leo uplink,” in *2022 International Conference on Space Optics, ICSO 2022*, B. Cugny, N. Karafolas, and K. Minoglou, Eds., 2022.
- [21] E. Hecht, *Gaussian Beams and Diffractive Optics*. Oxford University Press, 2006, ch. 3.
- [22] E. Hecht, “Fundamental properties of light,” in *Optics*. Pearson, 2006, ch. 2.
- [23] D. Giggenbach, M. T. Knopp, and C. Fuchs, “Link budget calculation in optical leo satellite downlinks with on/off-keying and large signal divergence: A simplified methodology,” *International Journal of Satellite Communications and Networking*, vol. 41, no. 5, B. Evans, Ed., pp. 460–476, 2023.
- [24] D. Giggenbach and A. Shrestha, “Atmospheric absorption and scattering impact on optical satellite-ground links,” *International Journal of Satellite Communications and Networking*, vol. 40, no. 2, pp. 157–176, 2022. doi: <https://doi.org/10.1002/sat.1426>. eprint: <https://onlinelibrary.wiley.com/doi/pdf/10.1002/sat.1426>.
- [25] J. Strohbehn, “Line-of-sight wave propagation through the turbulent atmosphere,” *Proceedings of the IEEE*, vol. 56, no. 8, pp. 1301–1318, 1968. doi: 10.1109/PROC.1968.6572.
- [26] W. B. Miller, J. C. Ricklin, and L. C. Andrews, “Effects of the refractive index spectral model on the irradiance variance of a gaussian beam,” *J. Opt. Soc. Am. A*, vol. 11, no. 10, pp. 2719–2726, Oct. 1994. doi: 10.1364/JOSAA.11.002719.
- [27] L. C. Andrews, R. L. Phillips, D. Wayne, *et al.*, “Near-ground vertical profile of refractive-index fluctuations,” in *Atmospheric Propagation VI*, L. M. W. Thomas and G. C. Gilbreath, Eds., International Society for Optics and Photonics, vol. 7324, SPIE, 2009, p. 732 402. doi: 10.1117/12.820369.

BIBLIOGRAPHY

- [28] S. Doss-Hammel, E. Oh, J. Ricklin, F. Eaton, C. Gilbreath, and D. Tsintikidis, “A comparison of optical turbulence models,” *Proc SPIE*, p. 12, Oct. 2004. doi: 10.1117/12.563746.
- [29] E. Brookner, “Improved model for the structure constant variations with altitude,” *Appl. Opt.*, vol. 10, no. 8, pp. 1960–1962, Aug. 1971. doi: 10.1364/AO.10.001960.
- [30] L. A. Bol’basova and V. P. Lukin, “Laser guide stars and models of atmospheric turbulence,” in *Optics in Atmospheric Propagation and Adaptive Systems XI*, A. Kohnle, K. Stein, and J. D. Ginglewski, Eds., International Society for Optics and Photonics, vol. 7108, SPIE, 2008, 71080H. doi: 10.1117/12.800585.
- [31] L. B. Stotts and L. C. Andrews, “Improving the hufnagel-andrews-phillips refractive index structure parameter model using turbulent intensity,” *Opt. Express*, vol. 31, no. 9, pp. 14 265–14 277, Apr. 2023. doi: 10.1364/OE.488544.
- [32] D. Giggenbach, H. Henniger, and F. David, “Long-term near-ground optical scintillation measurements,” in *Proceedings of the SPIE*, Vol. 4976, LIDO-Berichtsjahr=2003, 2003.
- [33] A. Knoedler and F. Moll, “Atmospheric turbulence statistics and profile modeling. local to dlr oberpfaffenhofen,” in *COAT 2019 (Communications and Observations through Atmospheric Turbulence: characterization and mitigation)*, 2021.
- [34] S. M. Rytov, “Diffraction of light by ultrasonic waves,” *Izvestiya Akademii Nauk SSSR, Seriya Fizicheskaya (Bulletin of the Academy of Sciences of the USSR, Physical Series)*, no. 2, pp. 223–259, 1937.
- [35] R. R. Beland, “Propagation through atmospheric optical turbulence,” in SPIE, Jul. 1, 1993. doi: 10.1117/3.2543821.ch2.
- [36] R. Barrios, “Fading loss for Earth-to-space lasercom affected by scintillation and beam wander composite channel,” *Optical Engineering*, vol. 59, no. 5, p. 056 103, 2020. doi: 10.1117/1.OE.59.5.056103.
- [37] K. Kiasaleh, “On the probability density function of signal intensity in free-space optical communications systems impaired by pointing jitter and turbulence,” *Optical Engineering*, vol. 33, no. 11, pp. 3748–3757, 1994.
- [38] L. C. Andrews, W. B. Miller, and J. C. Ricklin, “Spatial coherence of a gaussian-beam wave in weak and strong optical turbulence,” *J. Opt. Soc. Am. A*, vol. 11, no. 5, pp. 1653–1660, May 1994. doi: 10.1364/JOSAA.11.001653.
- [39] D. L. Fried, “Anisoplanatism in adaptive optics,” *J. Opt. Soc. Am.*, vol. 72, no. 1, pp. 52–61, Jan. 1982. doi: 10.1364/JOSA.72.000052.
- [40] V. I. Tatarskii, “Wave propagation in turbulent medium,” *Wave Propagation in Turbulent Medium*, 1961.
- [41] V. I. Tatarskii, *The effects of the turbulent atmosphere on wave propagation*. 1971.
- [42] W. B. Miller, J. C. Ricklin, and L. C. Andrews, “Log-amplitude variance and wave structure function: A new perspective for gaussian beams,” *J. Opt. Soc. Am. A*, vol. 10, no. 4, pp. 661–672, Apr. 1993. doi: 10.1364/JOSAA.10.000661.

BIBLIOGRAPHY

- [43] L. C. Andrews and R. L. Phillips, “I–K distribution as a universal propagation model of laser beams in atmospheric turbulence,” *Journal of the Optical Society of America A*, vol. 2, no. 2, pp. 160–163, Feb. 1985. doi: 10.1364/JOSAA.2.000160.
- [44] H. G. Sandalid, “Performance analysis of a laser ground-station-to-satellite link with modulated gamma-distributed irradiance fluctuations,” *J. Opt. Commun. Netw.*, vol. 2, no. 11, pp. 938–943, Nov. 2010. doi: 10.1364/JOCN.2.000938.
- [45] J. Parikh and V. K. Jain, “Study on statistical models of atmospheric channel for fso communication link,” in *2011 Nirma University International Conference on Engineering*, 2011, pp. 1–7. doi: 10.1109/NUiConE.2011.6153263.
- [46] D. Giggenbach and F. Moll, “Scintillation loss in optical low earth orbit data downlinks with avalanche photodiode receivers,” Nov. 2017.
- [47] D. Giggenbach and H. Henniger, “Fading-loss assessment in atmospheric free-space optical communication links with on-off keying,” *Optical Engineering*, vol. 47, pp. 046 001–1, 2008. doi: 10.1117/1.2951952.
- [48] H. T. Yura and W. G. McKinley, “Optical scintillation statistics for ir ground-to-space laser communication systems,” *Appl. Opt.*, vol. 22, no. 21, pp. 3353–3358, Nov. 1983. doi: 10.1364/AO.22.003353.
- [49] P. Beckmann, “Probability in communication engineering,” 1967.
- [50] L. Andrews, *Special Functions of Mathematics for Engineers* (Online access with subscription: SPIE Digital Library). SPIE Optical Engineering Press, 1998, ISBN: 9780819426161.
- [51] D. Giggenbach, F. David, R. Landrock, *et al.*, “Measurements at a 61 km near-ground optical transmission channel,” in *Free-Space Laser Communication Technologies XIV*, G. S. Mechele, Ed., ser. Proceedings of SPIE, LIDO-Berichtsjahr=2002, vol. Vol. 4, SPIE-The International Society for Optical Engineering, 2002, pp. 162–170.
- [52] D. Giggenbach, S. Parthasarathy, A. Shrestha, F. Moll, and R. Mata Calvo, “Power vector generation tool for free-space optical links - pvgc,” in *International Conference on Space Optical Systems 2017*, IEEE Xplore, 2017.
- [53] D. Giggenbach, A. Shrestha, C. Fuchs, F. Moll, and K. Saucke, “Reference power vectors for the optical leo downlink channel,” in *2019 IEEE International Conference on Space Optical Systems and Applications, ICSOS 2019*, Oct. 2019.
- [54] A. M. Carrillo Flores, D. Giggenbach, M. T. Knopp, and A. Shrestha, “Absolute power vectors for the optical leo uplink channel,” in *Communications and Observations through Atmospheric Turbulence (COAT 2023)*, 2023.
- [55] A. Ibrahim, “Performance analysis of optical receivers with space diversity reception,” *IEE Proceedings - Communications*, vol. 143, 369–372(3), 6 Dec. 1996, ISSN: 1350-2425.
- [56] E. Shin and V. Chan, “Optical communication over the turbulent atmospheric channel using spatial diversity,” in *Global Telecommunications Conference, 2002. GLOBECOM '02. IEEE*, vol. 3, 2002, 2055–2060 vol.3. doi: 10.1109/GLOCOM.2002.1188992.

BIBLIOGRAPHY

- [57] S. Wilson, M. Brandt-Pearce, M. Baedke, and Q. Cao, “Optical mimo transmission with multipulse ppm,” Aug. 2004, p. 289. doi: 10.1109/ISIT.2004.1365327.
- [58] S. Wilson, M. Brandt-Pearce, Q. Cao, and J. Leveque, “Free-space optical mimo transmission with q-ary ppm,” *IEEE Transactions on Communications*, vol. 53, no. 8, pp. 1402–1412, 2005. doi: 10.1109/TCOMM.2005.852836.
- [59] T. A. Tsiftsis, H. G. Sandalidis, G. K. Karagiannidis, and M. Uysal, “Optical wireless links with spatial diversity over strong atmospheric turbulence channels,” *IEEE Transactions on Wireless Communications*, vol. 8, no. 2, pp. 951–957, 2009. doi: 10.1109/TWC.2009.071318.
- [60] Y. Suhov and M. Kelbert, *Probability and statistics by example: Volume I. basic probability and statistics*, English (US). United Kingdom: Cambridge University Press, Jan. 2005, vol. 1, Publisher Copyright: © Cambridge University Press 2005., ISBN: 0521847664. doi: 10.1017/CBO9780511813634.
- [61] T. A. Tsiftsis, H. G. Sandalidis, G. K. Karagiannidis, and M. Uysal, “Optical wireless links with spatial diversity over strong atmospheric turbulence channels,” *IEEE Transactions on Wireless Communications*, vol. 8, no. 2, pp. 951–957, 2009. doi: 10.1109/TWC.2009.071318.
- [62] J. A. Anguita and J. E. Cisternas, “Spatial diversity measurements in a multiple-transmitter terrestrial fso link,” *Frontiers in Optics*, 2010.
- [63] I. I. Kim, H. Hakakha, P. Adhikari, E. J. Korevaar, and A. Majumdar, “Scintillation reduction using multiple transmitters,” in *Photonics West*, 1997.